Fall 2019

Circum-Arctic Mineralogy & Pan-Arctic Chronostratigraphy of Late Pleistocene Sediments: Developing a Comprehensive Age Model for the Western Arctic Ocean Using Unique Ice-Rafted Signals

Wesley Blake Myers
Old Dominion University

Recommended Citation

Myers, Wesley B.. "Circum-Arctic Mineralogy & Pan-Arctic Chronostratigraphy of Late Pleistocene Sediments: Developing a Comprehensive Age Model for the Western Arctic Ocean Using Unique Ice-Rafted Signals" (2019). Doctor of Philosophy (PhD), Dissertation, Ocean & Earth Sciences, Old Dominion University, DOI: 10.25777/amnr-k167
https://digitalcommons.odu.edu/oeas_etds/170

CIRCUM-ARCTIC MINERALOGY & PAN-ARCTIC CHRONOSTRATIGRAPHY OF LATE PLEISTOCENE SEDIMENTS: DEVELOPING A COMPREHENSIVE AGE MODEL FOR THE WESTERN ARCTIC OCEAN USING UNIQUE ICE-RAFTED SIGNALS

by

Wesley Blake Myers
B.S. August 2008, Old Dominion University
M.S. August 2011, Old Dominion University

A Dissertation Submitted to the Faculty of
Old Dominion University in Partial Fulfillment of the
Requirements for the Degree of

DOCTOR OF PHILOSOPHY

OCEANOGRAPHY

OLD DOMINION UNIVERSITY
December 2019

Approved by:

Dennis A. Darby (Co-Director)

David J. Burdige (Co-Director)

G. Richard Whittecar (Member)

Desmond C. Cook (Member)

ABSTRACT

CIRCUM-ARCTIC MINERALOGY & PAN-ARCTIC CHRONOSTRATIGRAPHY OF LATE PLEISTOCENE SEDIMENTS: DEVELOPING A COMPREHENSIVE AGE MODEL FOR THE WESTERN ARCTIC OCEAN USING UNIQUE ICE-RAFTED SIGNALS

Wesley Blake Myers
Old Dominion University, 2019
Co-Directors: Dr. Dennis A. Darby
Dr. David J. Burdige

To improve understanding of geographic mineral distribution from the circum-Arctic Ocean, samples from the Arctic periphery were collected and analyzed for (semi-) quantitative mineral composition. Most samples were collected from the North American region of the Arctic Ocean, a region which has had limited mineral investigation. In addition, more than 1000 published clay mineral data points were gathered to provide the most comprehensive clay mineral distribution map to date. The identification of a smectite source within the Canadian Arctic may reduce the usefulness of this mineral as a unique provenance signal for the Eurasian region. Smectite speciation may be useful in maintaining the use of this mineral for provenance determinations. Pyrophyllite, tridymite, zeolite and feldspar species were identified as potentially useful mineral provenance indicators. Strongly contrasting feldspar phases between North America and Eurasia provide an empirical signal for discerning sediment inputs to the Central Arctic. Similarities between ratios of potassium feldspar to plagioclase and quartz to total feldspar indicate that basin-wide sedimentation events likely occurred in the past. These basin-wide sedimentation events, if sufficiently constrained, could be useful for correlations between the eastern and western Arctic basins.

An age model for a sub-Arctic core from Yermak Plateau (JPC22) is developed using oxygen-isotope stratigraphy. The model is based on similarities between the global oxygen-isotope model and a unique paleomagnetic signal. This model identified several periods of rapid sedimentation that, if occurred over broad spatial scales, could be used as correlative tie points for the transfer of ages to central Arctic sediment records.

Central Arctic sediments have long been poorly understood due to the lack of age control. Using the newly developed oxygen-isotope stratigraphy from JPC22 (Yermak Plateau) an age model was developed for a central Arctic core from Mendeleev Ridge (JPC9). Based on this model, sediment transport mechanisms were interpreted in the context of glacial and interglacial environmental changes. Periods of rapid sedimentation are identified in the JPC9. Identification of these rapid events is typically hindered in central Arctic sediments due to reduced overall accumulation rates and reduced resolution. The timing of these unique depositional events appears to be coincident with Greenland stadial and interstadial events, therefore their origin may be related to Dansgaard-Oeschger cycles and other similar or related phenomena.

ACKNOWLEDGMENTS

I extend my gratitude to my committee members for their patience, flexibility, and hours spent editing this manuscript. Dr. Dennis Darby, without your unwavering support and guidance I would not have completed this research and dissertation. I will always value the knowledge that you have passed on to me and confidence you had in me. Dr. David Burdige, for stepping in to co-direct my committee I will be forever grateful. Your help through this process has been invaluable. Dr. Richard Whittecar, your passion for teaching has been an inspiration to me and many others. I am thankful for your support and confidence. Dr. Desmond Cook, when I was in a pinch and requested that you join my committee, you agreed. While your time served on my committee was short, it was no less appreciated, and I will be forever thankful for your support and service.

There are many other people who have contributed to the successful completion of this dissertation. Dr. Jens Bischof, our countless conversations ranging from Arctic mineralogy to football helped my research and kept me sane. Stephen Herman, your assistance through this research was vital and your support pushed me more than you know. Shannon Cofield, we struggled together and at times vented our frustrations, but you’ve been a critical companion on this journey. A huge shout out to my fellow students: Matt Richardson, Zach Howerton, Jason Ferguson, Kerby Dobbs, Ivy Ozmon, and many more.

Finally, to my family, I owe you everything. My wife, Sarah, for your love and support, I can never repay you. I will try. My son and daughter, Ethan and Nora, I love you and completed this dissertation for you. Mom, Dad and Jason, I love you and am so thankful for you and your support.

TABLE OF CONTENTS

LIST OF TABLES

Table Page

LIST OF FIGURES

1. INTRODUCTION

1.1 The Arctic region in a global context

Despite being the smallest ocean in the world in both volume and area, the Arctic Ocean is globally important and imparts far-reaching effects on global climate (ACIA, 2004; IPCC, 2015). Perennial and seasonal sea-ice cover modulates Earth's albedo and the region has a primary control on the deep-water formation that drives thermohaline circulation (Stein et al., 2008). Major changes have been recorded for the planet and for the Arctic region. In the past two decades, both ice extent and thickness have decreased to record lows (Lindsay and Schweiger, 2015; Comiso, 2012; Stroeve et al., 2012), with the smallest September sea-ice extent recorded in 2012 (Parkinson and Comiso, 2013).

The deep-water formation that drives thermohaline circulation forms via extremely cold and saline (dense) waters that sink in the North Atlantic region. The strongest control on this process is the low temperatures, the presence of sea-ice and the process of brine rejection as this ice forms. The reduction in sea-ice extent and thickness in recent decades results in an increased freshening through sea-ice melt and freshwater input via rivers and the fresher Pacific water through the Bering Strait. This freshening results in less dense waters and therefore has a significant influence on thermohaline circulation. With the current trends, loss of sea-ice cover will continue and how this loss will impact global climate remains to be seen.

The climate of the Arctic is an amplified signal of global climate (ACIA, 2004). Therefore, it is imperative that the dynamics of change in this polar region are understood to identify if and how Arctic changes are linked to global climate changes and provide the data necessary for predictive climate models.

Central to the understanding of the Arctic Ocean's place in global climate is accurate age control for sediment records of the past. This age control is needed to identify localized and synchronous basin-wide events to better understand if and how this region impacts global climate. Modeling experiments require more accurate age dating of climatic events than is currently available. Given the Arctic's sensitivity to and amplification of climate signals, this region is an important archive of global climate data, especially the central Arctic. Thus, the accurate understanding of the timing of events in this region is crucial to the understanding of the past, and prediction of future climate variability.

1.2 Background (age dating issues)

For most of the world's oceans, chronostratigraphy is, or can be well established using several techniques such as stable isotopes, radiocarbon, biostratigraphy, paleomagnetic stratigraphy, and lithostratigraphy (Clark et al., 1980; Spielhagen et al., 2004; Knies et al., 2007; Stoner et al., 2007; Kaufmann et al., 2008; Stein et al., 2010; Cronin et al., 2013). For example, stable oxygen-isotope ($\delta^{18}O$) data from multiple cores allowed definition of Marine Isotope Stages (MIS), a high-resolution Pliocene-Pleistocene type-section with which all paleoceanographic sediment records can be compared (Lisiecki and Raymo, 2005; LR04). Unfortunately, the unique environmental conditions of the Arctic region do not allow a direct correlation of most Arctic continuous isotope stratigraphic records to the well-established LR04 benthic age model stack (Alexanderson et al., 2014). The large Arctic freshwater influence via extraordinary volumes of riverine input, glacial ice disintegration, and brine rejection from sea-ice formation often results in the overprinting of $\delta^{18}O$ isotopic signatures (Spielhagen and Erlenkeuser, 1994; Knies et al., 2007). Additionally, there is a problem with the sporadic occurrence of benthic foraminifera in Arctic sediments, due to limited biological activity, low biodiversity, and high rates of calcareous test dissolution in the deep waters of the central Arctic Ocean basin(s) (Backman et al., 2004; Alexanderson et al., 2014). The difficulty in applying traditional chronostratigraphic methods along with the need for accurate chronostratigraphy in this highly important region emphasizes the eed for alternative methods to provide age control here where traditional methods of age dating have failed. Thus, there is a strong need for alternative methods to provide age control.

Traditional dating methods used to constrain ages in sediment cores such as radiocarbon for the last 40 kyr, biostratigraphy and to an extent paleomagnetic variation are insufficient for the central Arctic

Ocean due to the perennial sea-ice cover, low productivity, large freshwater input, and unique bottom water chemistry (Alexanderson et al., 2014). Paleomagnetism is problematic in the Arctic due to difficulty in defining paleomagnetic secular variation in this region (St. Onge and Stoner, 2011). The proper identification of reversals or excursions has been an issue in past studies. For example, Clark et al. (1980) utilized a paleomagnetic reversal, identified as the Brunhes/Matuyama boundary, and lithology to produce a lithostratigraphy that could be applied over large distances. This reversal was later challenged and determined to not represent a full reversal but rather a paleomagnetic excursion identified as either the Biwa II (Jakobsson et al., 2000) or the 'Pringle Falls event' (Stein et al., 2010). This challenge altered the view of central Arctic sedimentation records from being based on mm/kyr-scale resolution to cm/kyr-scale resolution. Alternatively, the paleomagnetic variation in Arctic sediments might be related to diagenetic changes (Xuan and Channel, 2010; Xuan et al., 2012). The unique bottom water chemistry of the Arctic Ocean can diagenetically alter the fine-grained magnetic fraction of the sediment record, and thus impart changes to the paleomagnetic record. For instance, diagenetic oxidation of titanomaghemite can impose low and negative natural remanence magnetization signals (Xuan and Channell, 2010). Additionally, these authors have proposed negative inclinations in cores via partially self-reversed chemical remanent magnetization, resulting from diagenetic maghemitization of sediment grains (Xuan and Channell, 2010). These diagenetic changes are related to the oxic conditions in the Arctic Ocean sediments resulting from low marine organic matter concentrations combined with low sedimentation rates, leading to minimal burial of organic matter and a minimized reducing conditions (Xuan and Channell, 2010). Despite the paleomagnetic issue, several studies have shown that lithostratigraphy and other physical and geochemical properties can be used to correlate cores over great distances (Spielhagen et al., 2004; Alder et al., 2009; Sellén et al., 2010; Stein et al., 2010).

Chronostratigraphy is essential for all paleoceanographic studies because understanding the timing of events is a critical first step in the interpretation of the sediment record. Because of the slow and highly variable rates of deposition in the central Arctic (Jakobsson et al., 2001; Backman et al., 2004;

Polyak et al., 2004; Adler et al., 2009; Sellén et al., 2009; Not and Hillaire-Marcel, 2010; Jakobsson et al., 2013), placing Arctic sediments in a regional or global temporal context requires closely-spaced age dates that are not available in the central Arctic (Polyak et al., 2009). Development of chronostratigraphy for sediment records in the Arctic has been a persistent problem since the first Arctic cores were recovered from the early ice camps (Clark et al., 1980). This issue has been especially true for the central and western portions of the Arctic basin, where a long-standing debate persisted as to whether this region was sediment starved or not. It is now generally accepted that the central region is likely not 'sediment-starved', but chronostratigraphy for this region is still problematic and poorly constrained (Backman et al., 2004; Alexanderson et al., 2014). High-resolution records are uncommon, and high-resolution records that extend past the Last Glacial Maximum (LGM) are even more rare.

1.3 Outlines and Objectives

This dissertation is constructed in the following way: the introduction of materials and methods used throughout this research will be discussed. The mineralogical data gaps from the circum-Arctic periphery will be discussed and filled. New regions that exhibit potentially useful mineral signals for provenance will be introduced, and the usefulness of these mineral data as indicators of provenance are discussed. An age model for a Fram Strait sediment record is introduced and based on oxygen-isotope stratigraphy. Using this Fram Strait age model, a central Arctic age model is developed, refined and substantiated by mineral and provenance trends identified within the records.

2 MATERIALS AND METHODS

2.1 Materials

2.1.1 Source Samples

A total of 34 circum-Arctic samples, comprised of surface sediment samples, near shore grab samples, and core top samples were chosen for bulk mineral (clays and non-clays) analysis and are representative of a good geographical coverage and as well as prominent source areas as determined by the Fe-oxide fingerprinting technique that matches these Fe grains to circum-Arctic sources in several previous studies (Darby, 2003; 2008; Darby and Bischof, 1996; Darby and Zimmerman, 2008; Darby et al., 2002; 2006; 2011; 2012; 2015). In addition to samples from the well-established Eurasian region, the primary sampling focus was from the North American shelves and coastal regions that are underrepresented in published mineralogy data sets. These 34 samples were added to the data compilation of >1000 samples from primarily the Eurasian Arctic shelves (Nürnberg et al., 1995; Wahsner et al., 1999; Rossak et al., 2000; Kalinenko et al., 2000; Kalinenko,2001; Stein et al., 2004; Vogt & Kneis, 2009; Saukel et al., 2010) to produce mineral distribution maps.

For past studies, the predominant methodology for obtaining clay mineral abundance data was through oriented XRD mounts of the <2 μm (or <1 μm) fraction and calculating mineral abundance based on peak width and height of mineral specific d-spacings from the resulting diffractograms (Biscaye, 1965). These oriented methods are subject to errors due to the size dependent nature of clays, especially the smectite species (and subset of phases). Care must be taken to ensure samples are fully disaggregated so the finest material (smectite) does not become enhanced at the surface of XRD mounts and result in erroneous concentrations (Gibbs, 1965). Until recently, an efficient method for identifying a full spectrum of non-clay phases was unavailable.

For bulk mineral analysis, each sample was wet sieved to remove the >45 μm fraction. The <45 μm fraction was then disaggregated and 1g of sediment was separated out for XRD analysis. Finally, bulk mineralogy was quantified using RockJock®, and mineral phases were summed to produce clay and non-clay mineral percentages (Eberl, 2004). For many of the mineral species discussed, multiple phases were combined to avoid phase misclassification. It has been shown through a comparison of two mineral quantification programs that RockJock® is well suited to identify a mineral species, but the specific mineral phase identification may be erroneous (Vogt, C. pers. comm.; Bahzanova, 2012).

2.1.2 Sediment Cores

The cores examined in this study were collected during the second leg of the Healy-Oden Trans-Arctic Expedition '05 (Darby et al., 2005, 2006, 2009). Each of these cores was photographed and analyzed onboard the ship for gamma-density, p-wave velocity and magnetic susceptibility via a GeoTek Multi Sensor Core Logger. Core HLY0503-JPC22 (80° 29.386'N, 007°46.141'E; 798 m water depth; henceforth JPC22) was retrieved from the Yermak Plateau in Fram Strait (**Figure 1**). This core location is directly in the path of sea-ice exiting the Arctic Ocean, meeting warmer North Atlantic waters and melting out the sediment load (**Figure 1**). The unique location of this core, in the Fram Strait, allows for the formation of a detailed age model (as described below).

Core HLY0503-JPC9 (Mendeleev Ridge; 79°35.605'N, 172°27.663'W; 2783 m water depth; henceforth JPC9) was selected as the western Arctic core to which the age model will be correlated (**Figure 1**). This core site is uniquely situated at the confluence of the Transpolar Drift (TPD) and the Beaufort Gyre (BG). The TPD is a prominent surface current that carries primarily Eurasian sediment entrained by ice across the Arctic to Fram Strait. The BG is an anticyclonic circulation gyre that is restricted to the Canada Basin and is dominated by Amerasian sediments. Thus, JPC9 receives a high volume of material from both the Eurasian and Amerasian Arctic. JPC9 has been correlated to several very similar cores along the Alpha-Mendeleev Ridge system using lithology, geochemical signatures and physical sediment parameters such as p-wave velocity etc. (Polyak et al., 2004; Darby et al., 2006). Thus, an updated age model for JPC9 can be transferred to other central Arctic cores.

Core sampling was determined based on Gamma-Ray density logs. Sediment density is a direct reflection of the mineralogy and compaction of the sediments, thus large variations in the mean density were sampled as they might help identify distinct mineral variations. Each core was sampled at different resolution depending on the method of analysis. Average sampling resolution for JPC22 was every ~6.3 cm, with higher resolution sampling in sections with the largest density variability. Similarly, in JPC9, the sections with the largest density variation were the focus. The overall sampling resolution average for JPC9 is ~6 cm (~4.5 cm in the upper 150 cm portion of the core).

2.2 Methods

2.2.1 Quantitative Bulk Mineralogy

Bulk mineralogy of the <45 μm fraction was determined through X-Ray Diffraction (XRD) of randomly-oriented powder mounts. Using <45 μm fraction is favored as it provides information regarding the bulk mineralogy, as opposed to just the clay fraction (<2 μm). More than 90-95 % of Arctic sediments are <45 μm, by examining this fraction the overwhelming quartz signal from the coarsest material is avoided while still retaining the bulk mineralogical signal. Randomly oriented XRD mounts are preferred to oriented ones, because the latter may bias the mineralogical composition, especially the non-clay minerals (Moore and Reynolds, 1997).

The average sampling resolution of JPC22 (0-585 cm; n = 96) and JPC9 (0-275 cm; n = 55) for mineralogical analysis was 6.3 and 5.6 cm, respectively. Details of the methods and procedures used in this study can be found in Srondon et al. (2001) and Eberl (2004). A brief synthesis of these methods follows: 1 g of <45 μm sample is mixed with 0.25 g of powdered, 99.9% pure corundum which serves as an internal standard. This mixture is ground in a McCrone

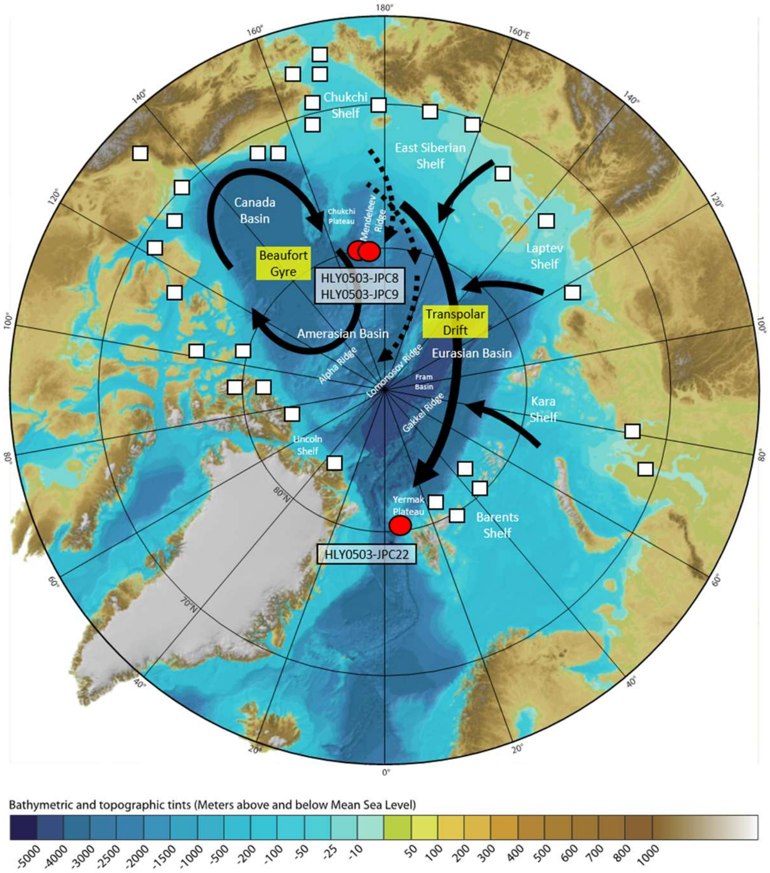

Figure 1. Study Area. Solid Black arrows indicate primary surface current features, Beaufort Gyre (BG) and Transpolar Drift (TPD). Cores JPC8, JPC9 and JPC22 are shown with red markers. Dashed arrows indicate areas of mixing. White boxes indicate the location of source area samples.

Micronizing mill for 5 minutes with 4 ml of methanol, and subsequently oven dried overnight at 80° C. The dried sample is sieved through a 400-500 μm sieve for homogenization. The sample is milled for ten minutes with three 10 mm acrylic balls in a ball mill to further enhance sample homogeneity. Next ~0.3 mL of hexane (0.5 mL per gram of pure clay) is added and the sample is mixed again for ten minutes in the ball mill, to ensure uniform sample homogenization and random dispersion of minerals. The sample is dried under a fume-hood, passed through the sieve again and side mounted in special powder mounts for XRD using frosted glass to help ensure random orientation. The samples analyzed on a Panalytical X'Pert PRO XRD with a Cu-tube from 5 to 65° 2θ with 0.2° steps at 2 seconds per step (45 mA, 40 kV). The sample pattern is transferred to the program RockJock which integrates mineral intensity factors of known standards in the program's library to calculate and match the pattern of the unknown sample, thus converting the samples mineral constituents into weight percent (Eberl, 2003). This program is shown to be accurate and precise, where values are ± 4 % of the actual values (Eberl, 2003). Independent tests of the RockJock program on random mineral mixtures all fell to ± 4 % or better of the actual values.

2.2.2 Provenance

The source samples were selected from the circum-Arctic margins, all of which have been previously analyzed for anhydrous Fe-oxide grain source determination (Darby and Bischof, 1996; Darby et al., 2015). All samples were wet sieved at 45, 63, and 250 μm. The magnetic portion of the 45-250 μm fraction was used for analysis of detrital anhydrous Fe-oxide grains as outlined in Darby et al. (2015). In short, each magnetic grain (ilmenite, magnetite, titanomagnetite, hematite, chromite, and exsolved phases of ilmenite and magnetite) is analyzed on an Electron Probe Micro Analyzer to determine the composition of 14 elements. The data for each grain were then matched to a source data set of >38,000 grains analyzed for the same elemental suite. The accuracy of this method is high with only a <2% error of mismatch. The average core sampling for JPC22 and JPC9 for Fe-grain provenance determination is 3 cm.

2.2.3 Texture

Texture was determined via a quantitative laser-based approach using a Malvern Mastersizer 2000. Based on the comparison with data from wet-sieve analysis, this method is slightly biased towards the coarser spectrum but largely the two methods are comparable. The instrument manufacturer estimates error of 5% for sediments up to 200 μm, with slightly increased error for greater size fractions (Malvern, 2015). For sediments > 200 μm, a conservative estimated error of 15% is used. The resulting data were useful in determining modes of transportation for the Arctic Region as a whole, as well as qualitatively determining varying current velocities in the case of the Fram Strait region.

Differentiating between sediment delivered via iceberg and sea-ice transport is difficult (Drewry, 1986; Polyak et al., 2010; St. John et al., 2015). For offshore sediment records collected from bathymetric highs, coarse sand-sized sediment is often interpreted as iceberg-derived rather than sea-ice derived (Polyak et al., 2010). But sea-ice can also transport coarse sand although more often it is finer-grained than iceberg IRD (Darby, 2003; Darby et al., 2011). Thus, here the use of glacial intervals and coarse sand-sized and larger IRD will be used to infer iceberg transport.

Using textural characteristics iceberg transport in core sediments is identified as coarse dominant, sea-ice transport is presumed for fine sand dominant, and intervals with roughly equal parts fine and coarse sand are considered mixed. Thus, based on IRD texture and timing (i.e. whether it occurs during a glacial or interglacial), the probable mode of transport can be determined (Pfirman et al., 1989; Nürnberg et al, 1994). When the distribution of medium-coarse sand fraction (>250 µm) exceeds the coarse silt fraction (45-63 µm) during glacial periods, the inferred transport mode is by iceberg. Conversely, during interglacial periods, most IRD signals are presumed to be sea-ice derived. The only exception is if during interglacial periods, the coarse fraction greatly exceeds the coarse silt fraction then iceberg transport can be invoked as a major contributor to IRD transport. This simplistic approach provides only an estimate of the mode of ice rafting.

3 CIRCUM-ARCTIC MINERALOGY

3.1 Introduction

The geologic terrains surrounding the Arctic Ocean impart distinct lithologic, mineralogic, and geochemical signatures in the surface sediments of the circum-Arctic Ocean (**Figure 2**) (Darby et al., 1989; Stein, 2008; Fagel et al., 2014). Therefore, spatial and temporal trends in Arctic Ocean sediments might reflect variations in source provenance (Bischof, Clark, & Vincent, 1996; Bischof & Darby, 1997; Wahsner et al., 1999; Phillips & Grantz, 2001; Knies et al., 2003; Viscosi-Shirley et al., 2003; Darby et al., 2011; Fagel et al., 2014; Darby et al., 2015), changes in transport processes and pathways (Bischof and Darby, 1997; Wahsner et al., 1999; Schoster & Stein, 1999; Schoster et al., 2000; Phillips & Grantz, 2001), and aid in constructing stratigraphic correlations and paleoenvironmental reconstructions (Clark et al., 1980; Müller & Stein, 2000; Jakobsson et al., 2001; Polyak et al., 2004). The methods for these studies vary, but variations in clay mineralogy, heavy minerals, trace elements, lithic grain counts, and isotopes are commonly used (Bischof, Clark, & Vincent, 1996; Darby & Bischof, 1996; Wahsner et al., 1999; Hemming et al., 2002; Krylov et al., 2008; Immonen et al., 2009; Fagel et al., 2014). On this basis, it is important to understand contrasting mineral variations in shelf sediments around the Arctic.

The Arctic Ocean is unique in that sedimentation is not limited to density-driven currents and riverine inputs. While these two processes are prevalent, sea-ice and glacial ice transport are also important, especially to transport sediment onto the ridges in the central Arctic. It has been shown that to best constrain provenance, information should be obtained on all sediment size fractions (Andrews & Principato, 2002). However, provenance studies generally focus on either the sand or the clay fraction, leaving the silt fraction under-studied and poorly understood. The silt fraction is arguably the most diagnostic fraction for glacial periods as it is the product of abrasion and crushing at the base of ice sheets and glaciers (Drewry, 1986; Andrews & Principato, 2002). Furthermore, significant differences between silt- and clay-sized mineralogy have been documented (Andrews et al., 1989). The transport- and climate-specific controls on sediment grain-size and transport highlights the necessity of studying a wide range of sediment size in bulk sediments.

Overall circum-Arctic data coverage for clay and non-clay mineralogy is not uniform, with the North American region underrepresented. In the Eurasian Arctic, clay minerals have been extensively studied (Nürnberg et al., 1995; Kalinenko et al., 1996; Wahsner et al., 1999; Kalinenko et al., 2001; Viscosi-Shirley et al., 2003; Stein et al., 2004; Knies and Vogt, 2009). Non-clay mineralogy is limited to point counts of the coarse fraction and generally focuses on heavy minerals, carbonates and lithics (Bischof and Darby, 1997; Behrends et al., 1999). In the North American regions both clay and non-clay mineralogy has largely been ignored, apart from portions of the Beaufort Sea shelf (Naidu & Mowatt, 1982, 1983)

The objective of this chapter is to provide a baseline of quantitative bulk-mineralogy for the circum-Arctic using randomly oriented XRD analyses and add to the overall understanding of mineral distribution around the Arctic Ocean. A brief summary of clay mineral variability and potentially valuable source-specific non-clay minerals determined from bulk sediment samples for the circum-Arctic will be provided and gaps in the geographic coverage of clay mineralogy will be filled-in.

3.2 Current Understanding and Distribution of Arctic Mineralogy

While most studies examining mineralogy of the Arctic Ocean focus on the primary clay mineral groups: smectite (*S*; including montmorillonite and *I/S* mixed layered phases), illite (*I*), chlorite (*C*), and kaolinite (*K*), this work summarizes our understanding of the full range of both clay and non-clay mineral phases. Some background information regarding the current understanding of non-clay and clay mineralogy follows.

3.2.1 Clay Minerals

Illite and chlorite are the most common clay mineral phases found throughout the Arctic, apart from the coastal regions of the Laptev and Kara Seas and certain areas around Franz Josef Land (Wahsner et al., 1999; Viscosi-Shirley et al., 2003). These clay minerals are very common in northern latitudes, due to the physical weathering of plutonic and metasedimentary rocks (Chamley, 1989). These rock types are commonly found throughout Siberia and Alaska (Viscosi-Shirley et al., 2003 and references therein).

Generally, the concentration of illite and chlorite throughout the Arctic is greater than 50% and 20% of bulk clay mineralogy, respectively (Viscosi-Shirley et al., 2003)

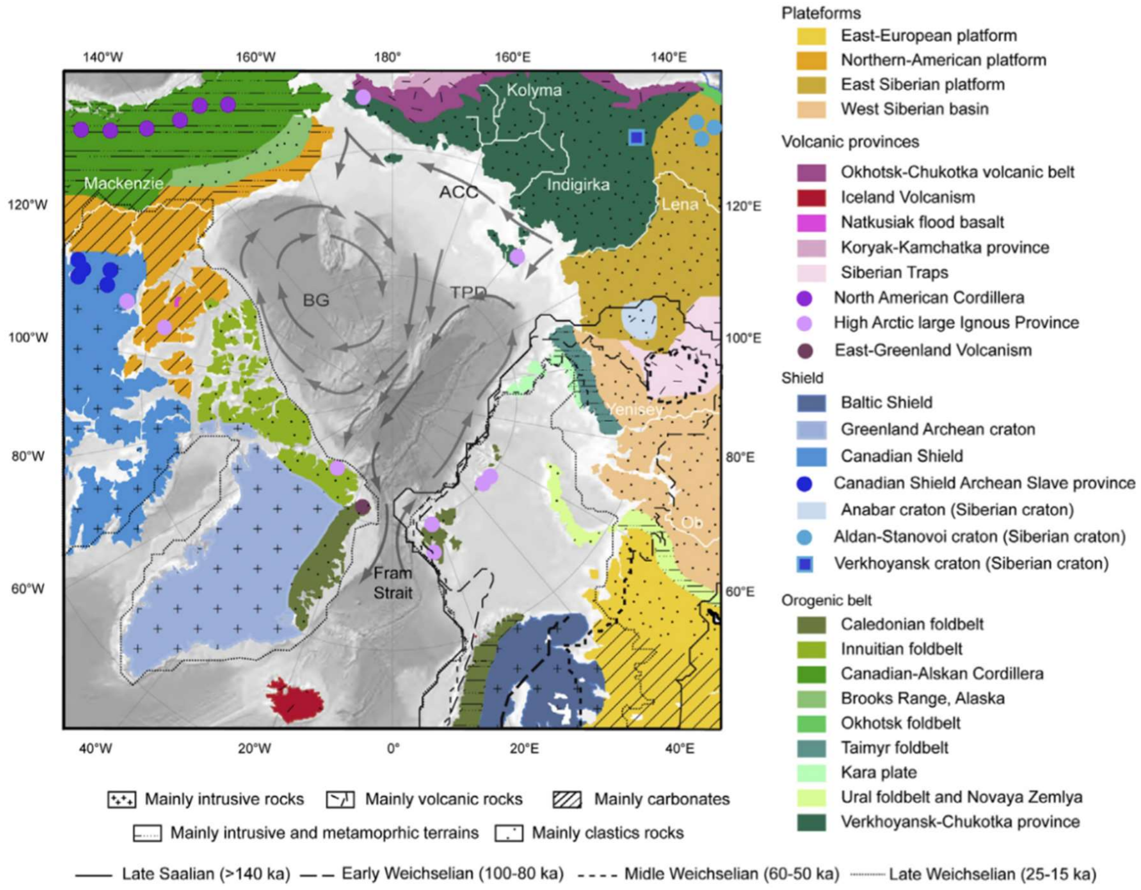

Figure 2. Map of circum-Arctic lithology, modern surface current distribution, and past maximum ice sheet limits (from Fagel et al., 2014). The Transpolar Drift (TPD) and Beaufort Gyre (BG) surface currents are highlighted with grey arrows. The lithologies of the terrains adjacent to the Arctic Ocean are highlighted (AMAP, 1998; Harrison et al., 2008). Primary structural units are identified by color: shields in blue, orogenic foldbelts in green, sedimentary platforms in yellow, and volcanic terrains in pink.

The clay minerals smectite and kaolinite exhibit the highest degree of gradation across the Arctic shelves. It should be mentioned that for qualitative clay mineral studies all expansive clays are assigned to the "smectite group"; including smectites, montmorillonites, and interstratified smectite-illite mixed layered clays (Vogt & Knies, 2009). Soil production under warm and wet weathering conditions will produce “smectite group” clays (Griffin et a., 1968; Tucker, 1988). A major source of expandable clays is the product of hydrolysis and submarine weathering and diagenetic alteration of volcanogenic material (Vogt & Knies, 2009). Basaltic rocks are the most prevalent source of these expandable clay minerals; these rock-types are commonly found along the mid-ocean ridges as well as from terrestrial sources such as the Putorana flood basalts of northern Siberia (Wahsner et al., 1999; Vogt & Knies, 2009).

3.2.1.1 Eurasian Epicontinental Seas

Eurasian shelf sediment clay mineralogy has been extensively studied (**Figure 3** and **4**; Nürnberg et al., 1995; Kalinenko et al., 1996; Wahsner et al., 1999; Kalinenko et al., 2001; Viscosi-Shirley et al., 2003; Stein et al., 2004; Knies and Vogt, 2009). The clay mineral distributions of the Chukchi Sea and portions of the Beaufort Sea shelf have also been well constrained (Naidu & Mowatt, 1983; Wahsner et al., 1999; Viscosi-Shirley et al., 2003). The general clay mineral assemblage of the Eurasian Sea shelves is illite-chlorite-kaolinite-smectite (I-C-K-S; I range: 40-70% /C ~23% /K 10-40% /S <5-20 %; from Wahsner et al., 1999). Conversely, clay mineralogy of most of the Amerasian region is largely unknown. Mineral distribution maps with a subset of these clay mineral data identifies the paucity of data for the Amerasian shelf regions (**Figures 3** and **4**). Clay mineral assemblage trends vary between the Eurasian seas, and these trends are controlled by the distinctive variation in terrestrial geology (**Figure 2**). The mineralogical trends in the Amerasian Arctic are also distinct, as has been shown with the high concentrations of carbonates originating from the Canadian Arctic Archipelago (Vogt, 1997).

3.2.1.2 Illite

The dominant clay mineral throughout the Arctic is illite, and the distribution of this mineral is uniform (**Figure 3**). In the Barents Sea concentrations of illite generally range between 50-60 %, with maximum concentrations of up to 70 % off the coast of Novaya Zemlya. Overall, illite exhibits little gradation except for the Kara and western Laptev Seas where illite is inversely related to smectite abundance. Illite concentrations in the Kara Sea ranging from 15-40 % corresponding to elevated smectite signals (Wahsner et al., 1999). In the Laptev Sea, illite ranges between 35-63 % and increases eastward

(Viscosi-Shirley et al., 2003). The East Siberian Sea boasts the highest average illite concentration (62 %) for the Eurasian Arctic and exhibits little gradation. Due to increases in chlorite and slight increases in smectite, illite concentrations decrease towards the Chukchi Sea where the average abundance is 51 % (Viscosi-Shirley et al., 2003). The range of illite abundance in the Chukchi is 38-59 % with the lowest concentrations found in the central portion of the sea and the highest abundances nearer the coasts (Naidu & Mowatt, 1983). Because of its ubiquitous occurrence, its usefulness for provenance is limited.

3.2.1.3 Chlorite

Overall, chlorite has an average concentration of 23 % in Eurasian Arctic shelf sediments with no apparent regional variations (Wahsner et al., 1999). In the Barents Sea, an average chlorite abundance of 20 % is found that decreases towards the east. The Kara Sea exhibits a range in chlorite of 10-20 % (Wahsner et al., 1999), and 14-25 % in the Laptev Sea with no trends evident (Viscosi-Shirley et al., 2003). For the East Siberian and Chukchi Seas, chlorite ranges from 16-39 % with an average of 23 % (Wahsner et al., 1999; Viscosi-Shirley et al., 2003). In general, chlorite exceeds kaolinite in the eastern East Siberian Sea and the Chukchi Sea. Kaolinite exceeds chlorite only on the Siberian coast near Wrangel Island and the North Slope of Alaska (Naidu & Mowatt, 1983). The primary source of this chlorite is the Bering Sea and due to chlorite-rich inputs from western Alaskan rivers (Naidu & Mowatt, 1983) and presumably from the Chukotka volcanic belt of eastern Siberia (Viscosi-Shirley et al., 2003). The material from the Bering Sea is carried into the Arctic via the Pacific Water inflow where it splits into three major branches (Aksenov et al., 2016). One branch flows through the Harold Trough in the central Chukchi Sea and into the Beaufort Sea. A second branch flows along the northslope of Alaska into the Canadian straits, and the final branch flows along the continental slope of the East Siberian Sea and into the Transpolar Drift (TPD).

3.2.1.4 Smectite

Smectite generally exhibits low concentrations throughout the Arctic, but also exhibits the sharpest gradients of any clay mineral (**Figure 4**). Maximum concentrations of smectite are found in and around the Ob and Yenisei River mouths with values up to 70% (Wahsner et al., 1999). Concentrations decrease radially from these river mouths, with <10% concentrations found in the southeast Barents Sea (Wahsner et al., 1999). A strip of elevated smectite concentrations continue eastward through Vilkitski Strait and into the western Laptev Sea; these elevated concentrations can also be from the Khatanga River draining into the western Laptev Sea. Concentrations throughout this region reach as high as 40% and decrease to the east where levels are generally <10 % in the East Siberian and Chukchi Seas (Naidu & Mowatt, 1983; Wahsner et al., 1999; Viscosi-Shirley et al., 2003). The limited published data available for the Beaufort Sea indicate that smectite concentrations increase to 12-19% along the North Slope of Alaska (Naidu & Mowatt, 1983). The most likely source for the increase in smectite for this region is the montmorillonite and bentonite-rich Cretaceous shales near the Colville River on the north slope of Alaska (Darby, 1975). Due to the occurrence of elevated smectite in multiple circum-Arctic regions, the usefulness of smectite as a provenance indicator is brought into question. Differences in smectite phases between the Eurasian and North American smectite sources might allow for their discrimination.

3.2.1.5 Kaolinite

Kaolinite is generally found in low concentrations; however, elevated values are noted for the Amerasian basin (Darby, 1975) and in parts of the northern Barents and Kara Seas (Wahsner et al., 1999; Vogt & Knies, 2009). This mineral is indicative of hot and humid climates, and is dominant in the tropics (Chamley, 1989). In the Arctic, kaolinite deposits are found in sedimentary deposits that were formed under warmer and wetter conditions in the past (Viscosi-Shirley et al., 2003). Kaolinite-bearing deposits of the Arctic are found throughout Alaska and Canada in relict soils and shales, such as the Mesozoic sedimentary rocks of the Alaskan North Slope and the Mackenzie River area (Darby, 1975). An additional major kaolinite source is the outcropping Triassic sandstones of Franz Josef Land that results in concentrations of up to 90% kaolinite in some Franz Josef Land soils (Wahsner et al., 1999).

Overall, kaolinite in the eastern Eurasian Arctic is relatively low (**Figure 4**). Through the northern region of the Eurasian Arctic the kaolinite concentrations are in the range of 10-20 % (Wahsner et al., 1999; Viscosi-Shirley et al., 2003) The highest concentrations of kaolinite originate from Franz Josef Land, where concentrations reach >30%. Concentrations as high as 90% have been noted for Mesozoic sedimentary rock outcrops on some Franz Josef Land islands (Wahsner et al., 1999). In general, the distribution of kaolinite is low (<10%) along the coasts of the Eurasian seas (Wahsner et al., 1999). The only exception is in the western Laptev where coastal concentrations increase to between 10-20% (Wahsner et al., 1999). The increased kaolinite in this portion of the western Laptev is likely direct input, via sea-ice or current transport from the Franz Josef Land area.

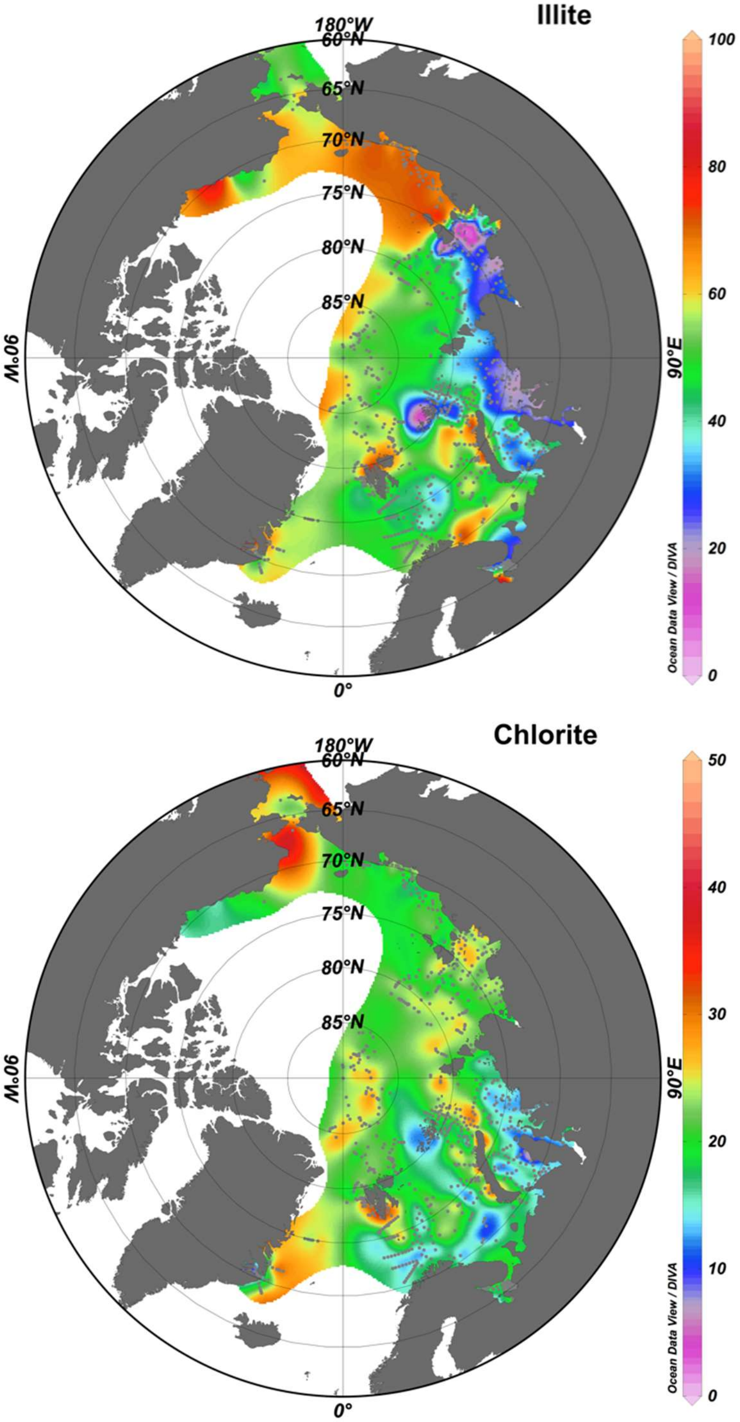

Figure 3. Previously published distribution of illite (upper) and chlorite (lower) over the Eurasian Arctic shelves. Data presented here are from various sources and taken from Pangaea.de. Maps generated using Ocean Data Viewer (Schlitzer, 2012).

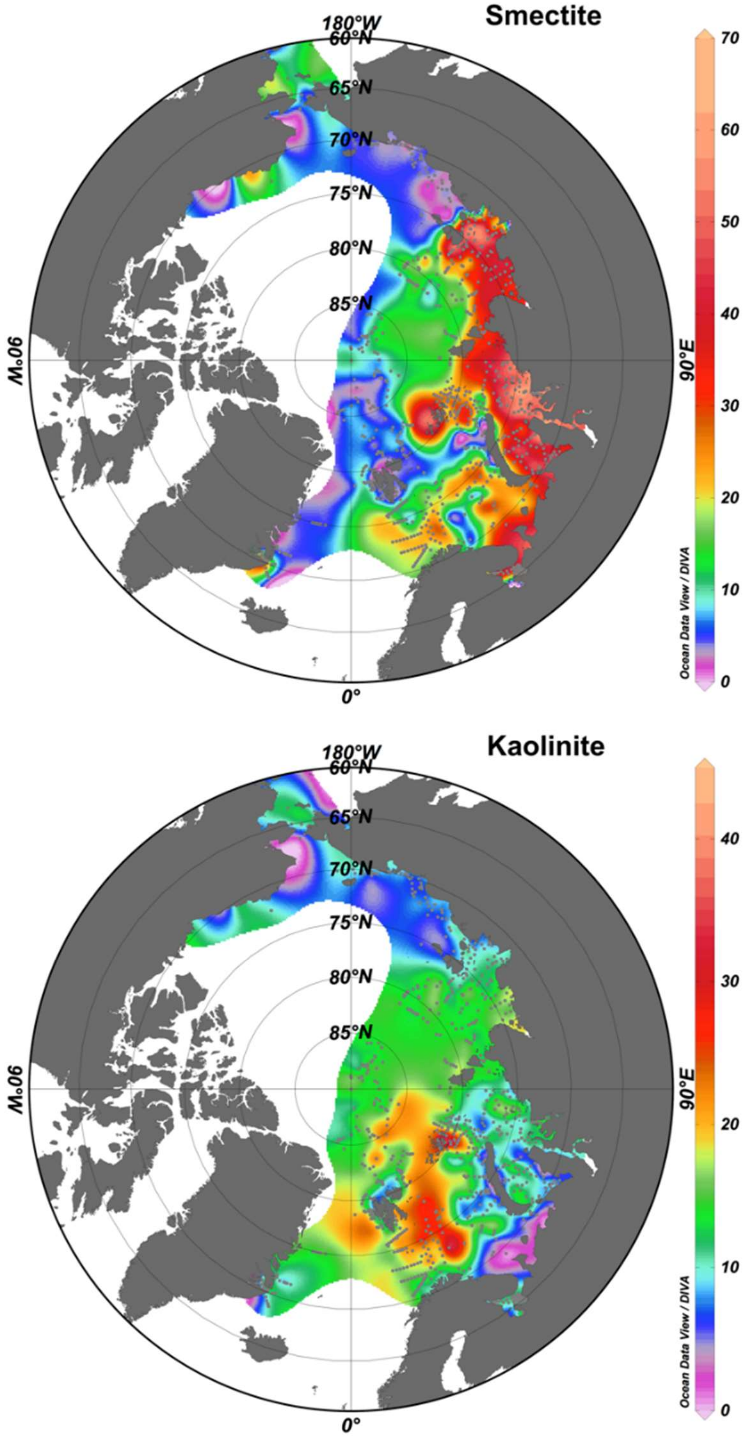

Figure 4. Published distribution of smectite (upper) and kaolinite (lower) over the Eurasian Arctic shelves. These two clay minerals exhibit the highest degree of variability across the Eurasian shelves. Maps generated using Ocean Data View (Schlitzer, 2012).

3.2.2 Non-Clay Minerals

Studies of specific non-clay mineral phases are lacking, and the geographic coverage is limited. Exploration of the bulk mineral variation throughout the circum-Arctic periphery has been limited (except for Vogt, 1997). Thus, the study of circum-Arctic non-clay mineralogy is limited and more needs to be done to quantify mineral variations. The goal is to fully recognize the potential for using mineral variation in the Arctic sediment record to decipher spatial and temporal changes in provenance and track changes in transport pathways.

Vogt (1997) analyzed material from around the Arctic and identified distinct mineral zones. The following descriptions are from Vogt (1997) and in some cases, have been further substantiated or expanded on by others. The first, and most striking difference, was the extensive carbonate rock outcrops of the Canadian Arctic Archipelago and Northern Greenland (Franklinian Reef Belt) and the primarily siliclastic sediments that dominate the Siberian Shelves. The Siberian shelf region could be further divided into two primary zones each defined by distinct mineral suites. The eastern Kara Sea and the western Laptev Sea delineates the westernmost distinct mineral zone and is defined by the mineral suite consisting of high concentrations of smectite, (clino-) pyroxene, and plagioclase. These minerals are indicative of the extensive outcrops of Putorana flood basalts that are drained by the Ob, Yenisei, and Khatanga Rivers. The second distinct mineral zone comprises the eastern portion of the Siberian shelves and includes the eastern Laptev Sea and the East Siberian Sea. This region is associated with elevated concentrations of feldspar, quartz, illite, mica and chlorite association combined with the trace minerals hornblende and epidote. This suite of minerals is indicative of the siliclastic sediments that dominate this region and the less dominant volcanic material that occurs sporadically throughout the eastern Siberian region.

In addition to the regionally distinct mineral zones, more localized zones are also recognized. The Franz Josef Land and Svalbard archipelagos also exhibit distinctive mineral suites that result from the geology of these islands and the geographic location. Franz Josef Land is associated with a mineral composition enriched in quartz and kaolinite. Svalbard has a very diverse geology, resulting in specific mineral suites of highly metamorphic crystalline rocks, dolomite-rich carbonates, and sedimentary rocks with a high diagenetic potential indicating that secondary authigenic minerals could be prevalent in this region (Vogt, 1997).

3.3 Clay Mineralogy Results and Discussion

From the >1000 data points in this study, the overall clay mineral assemblage is I>C>S>K (48>20>19>13 %; n=1040; **Tables 1** and **2**). In general, the illite and chlorite concentrations are constant while the smectite and kaolinite concentrations show the greatest variation (Wahsner et al., 1999; Stein, 2008). A total of five unique clay mineral assemblages are identified determined from the data compilation produced in this study. In general, the clay mineral assemblages for the Eurasian Arctic seas are like those identified by previous studies. There are a few exceptions that will be further explored, and potential explanations will be examined. A first-order assessment of the clay mineral variation of the North American sources will be addressed. Finally, a comparison to the central Arctic clay mineral assemblage will be made.

3.3.1 Eurasian Arctic

The clay mineral distribution for the Eurasian shelf is consistent with the findings of previous studies (Stein et al., 1994; Wahsner et al., 1999; Viscosi-Shirley et al., 2003). This study and previous studies identify an overall clay mineral assemblage for the Eurasian Arctic shelf of I>S>C>K (**Table 1**; Wahsner et al., 1999). Illite has an average concentration of 45.3 %, with a general trend of higher concentrations in the eastern portion of the Eurasian Arctic Shelf. The average chlorite concentration for the Eurasian Arctic is approximately 20 % (**Table 1**; **Figures 3** and **5**). Of the clay mineral phases, chlorite exhibits the least spatial variability across the Eurasian shelves. Kaolinite and smectite exhibit the highest degrees of gradation across the Eurasian shelves. Kaolinite has an average concentration of 13 % with Franz Josef Land and the eastern East Siberian Sea exhibiting the highest and lowest concentrations, respectively (**Table 1**; **Figures 4** and **6**). The clay mineral smectite experiences the sharpest concentration gradients in the circum-Arctic, with a range of 0 to 68 % and an average of 21.7 % (**Table 1**; **Figures 4** and **6**).

Across the Eurasian Arctic seas, the clay mineral assemblages determined from this study correspond well with those found previously for the eastern Kara, East Siberian, and Chukchi Seas. For the Barents, western Kara, and Laptev, the clay mineral assemblages determined in this study differs slightly from those previously published (**Table 1**). Each sea will be discussed, with more attention given to those seas with clay mineral assemblages that differ from those previously published.

3.3.2 Barents Sea

The Barents Sea follows a clay assemblage of I>C>S>K (48.7>19.9>16.6>14.9 %; n = 410; **Table 1**; **Figures 3** to **6**). This differs from previous studies which have found a clay mineral assemblage of illite-chlorite-kaolinite-smectite (Wahsner et al., 1999; Vogt & Knies, 2009). Possible reasons for the inversion of kaolinite and smectite in abundance could be a difference in the delineation between the Barents and Kara Seas, a difference in sample distribution, or both. Both explanations could impart a higher smectite signal into the Barents Sea assemblage by recording a stronger Kara Sea influence. The Barents Sea boasts the highest average kaolinite concentration of the Eurasian shelf seas, as well as the highest individual kaolinite concentrations of the entire Arctic. The source of this kaolinite-rich material is the outcropping Mesozoic sedimentary rocks of Franz Josef Land. The western coast of Novaya Zemlya has been identified as a potential source for the enhanced chlorite concentrations found in the Barents Sea (Nürnberg et al., 1995; Wahsner et al., 1999).

For the western Barents Sea an assemblage of I>C>K>S was found (49>21>17>13 %; n = 175; **Table 1**; **Figures 3** to **6**; Vogt & Knies, 2009). In this area a band of high concentration kaolinite occurs along 30° E. Glacial erosion has been suggested as the origin of this strip of increased kaolinite, citing the limited outcrops and submarine sources of enriched kaolinite to imply lateral transport via currents and sea-ice as the source (Vogt & Knies, 2009). However, the extensive outcrops of kaolinite-rich Mesozoic material on Franz Josef Land provides the most logical source for this band of kaolinite enriched surface sediments. Atlantic waters enter the Arctic as the Fram Strait Branch, north of Svalbard and Franz Josef Land; this current meets a zone of ice melt where this water is brought into the mixed layer via mechanical stirring and then splits. One branch continues as the Fram Strait branch, and the other flows back into the Barents Sea between Svalbard and Franz Josef Land. An additional branch flows back into the Barents around the northern portion of Franz Josef Land (Schauer et al., 2002; Rudels et al., 2015). The southern limit of this back flow is modified by the location of the polar front (Oziel et al., 2016). Comparing the Barents Sea circulation against kaolinite distribution, the most logical source of Barents Sea kaolinite is laterally transported material from Franz Josef Land carried along southerly Arctic outflow currents (**Figure 7**). Additional sampling would be necessary to confirm that this band is an extension from Franz Josef Land as the mineralogy of the intermediate area is not fully constrained.

The Greenland Sea region exhibits a similar assemblage to the proximal Barents Sea, following the I>C>S>K trend. This region includes coastal Greenland and a large portion of the Fram Strait constituting the Greenland Sea. The Greenland Sea and coastal sediments have slightly higher recorded illite concentration and lower values of smectite and kaolinite (I>C>S>K; 59.2>19.3>11.0>10.5 %; n = 56; **Table 1**; **Figures 5** and **6**). The elevated illite in this region might be sourced to northern Greenland where high illite concentrations have been recorded (**Figure 4**). The reduction in smectite concentration is likely a result of distance from the primary source and/or dilution from larger inputs of other clays from the nearby landmasses of Svalbard, Greenland, and the eastern Canadian Arctic.

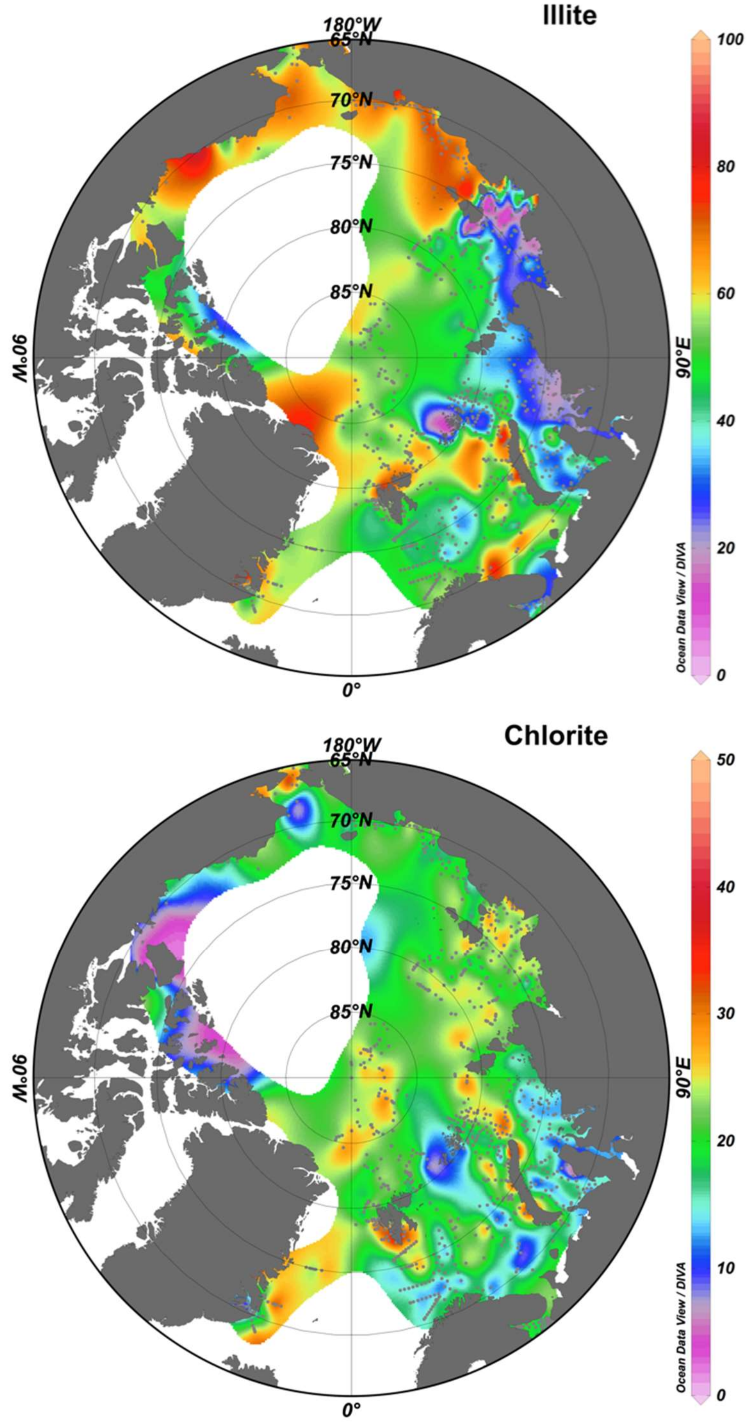

Figure 5. Distribution map of illite and chlorite, including the 34 source samples from this dissertation. North American sources show that illite concentrations are elevated and chlorite is nearly absent in the North American region. Sampling distribution is too low in this region to determine if these trends are local or constrain the entire region. Map generated using Ocean Data Viewer (Schlitzer, 2012).

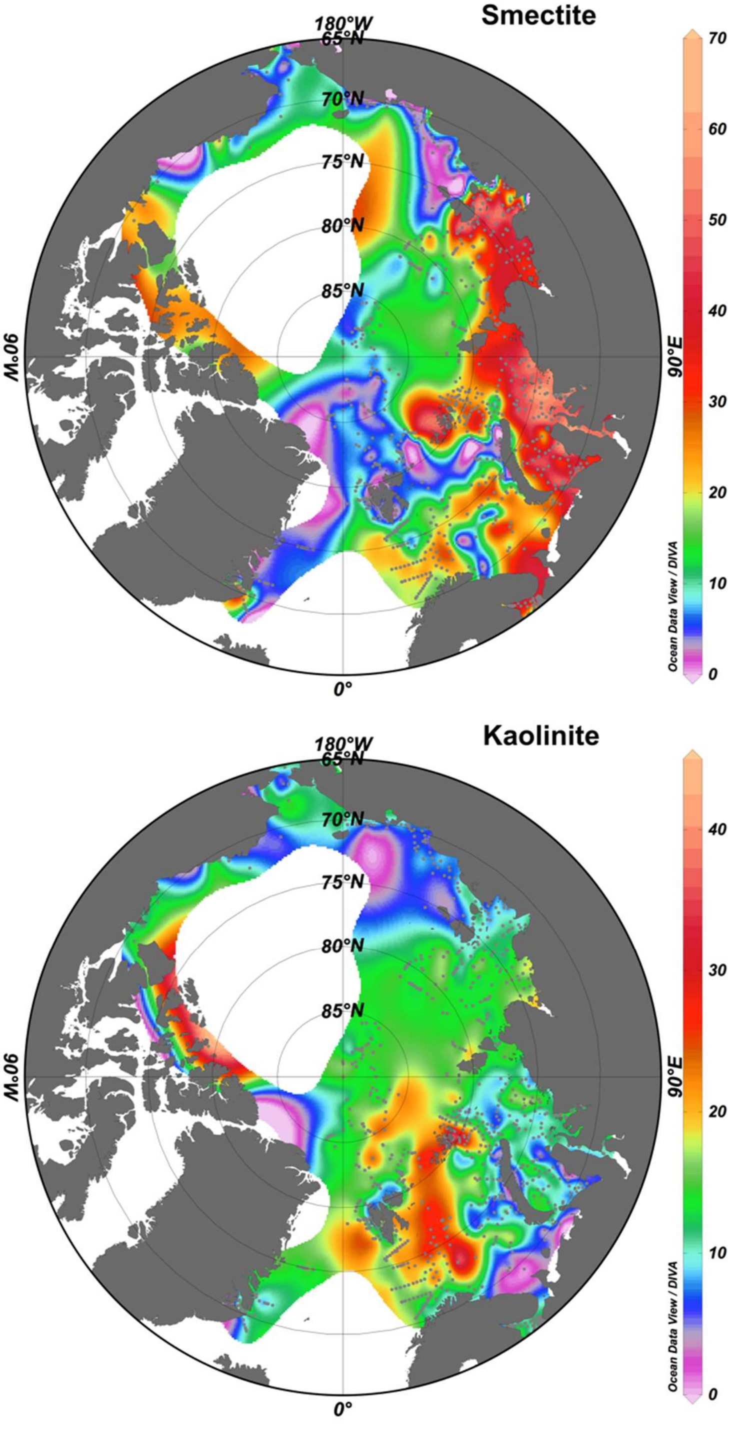

Figure 6. Distribution map of smectite and kaolinite, including the 34 samples from this dissertation. The distribution of smectite and kaolinite throughout the North American region appears to be elevated and significant. Sampling distribution is too low in this region to determine if these trends are local or constrain the entire region. Map generated using Ocean Data Viewer (Schlitzer, 2012).

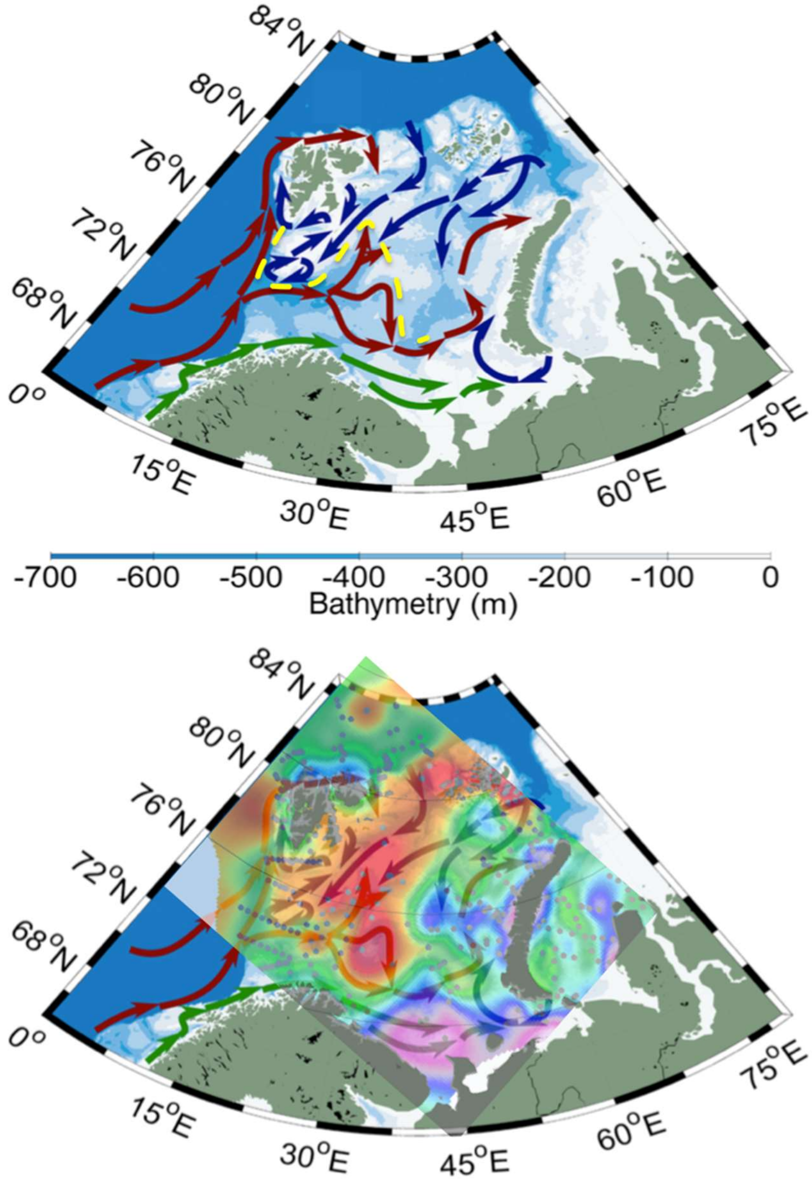

Figure 7. (Upper) Schematic showing the Barents Sea circulation (base map from Oziel et al., 2016). The red arrows indicate the Fram Strait Branch and the Barents Strait Branch of the Atlantic water inflow. Blue arrows indicate the Arctic water outflow. The yellow dashed line shows the estimated location of the modern-day polar front of sea-ice (Lind & Ingvaldsen, 2012; Oziel et al., 2016). (Lower) Same map with Barents Sea kaolinite distribution overlain, showing the probable source of the kaolinite in this sea as from Franz Josef Land transported on the Arctic water outflow and the distribution modified by a shifting polar front. Warmer colors indicate higher Kaolinite concentrations.

3.3.3 Kara Sea

To the east of the Barents Sea, the Kara Sea is characterized by the highest concentrations of smectite found in the Arctic Ocean (S>I>C>K; 38.6>32.8>17.2>11.4 %; n = 160; **Table 1**; **Figures 5** and **6**). The high expandable clay content is attributed to the riverine input of the Ob and Yenisei Rivers that drain the massive Putorana Flood Basalt terrain of the western Siberian Hinterland (Wahsner et al., 1999; Schoster et al., 2000; Vogt & Knies, 2009). Excluding the samples from the north central Kara Sea (St. Anna Trough), no distinct change in clay mineral assemblage is identified. From the west to east, there is a small decrease in smectite and increase in illite concentrations, probably due to mixing and dilution of the smectite by illite.

Previous studies have identified regional differences in the clay mineral assemblage of the eastern and western Kara (Wahsner et al., 1999). In this study, the Kara Sea is represented by an assemblage of S>I>C>K in the east and I>S>C>K in the west. Only the far west portion of the Kara Sea, west of the Ob River Gulf and south of Novaya Zemlya is the I>S>C>K assemblage evident. However, this region is small and likely contributes little to the sediments exiting the Kara Sea, so this distinction is not considered relevant. This earlier study included a high sampling density from the St. Anna Trough and the Kara Sea region around Novaya Zemlya which might have resulted in the mineral assemblage shift (Wahsner et al., 1999). The current study includes a higher sampling density across the entire Kara Sea and does not recognize a prominent east-west division, finding a S>I>C>K assemblage across the vast majority of the Kara Sea (Table 1).

3.3.4 Laptev Sea

Much like the Kara Sea to its west, the Laptev Sea is associated with very high concentrations of expansive clay minerals. The primary source for the smectite in the Laptev is from input from the Kara Sea though Vilkitski Strait and the Khatanga River which also drains the Putorana flood basalts of the Siberian Hinterland (Wahsner et al., 1999; Schoster et al., 2000; Viscosi-Shirley et al., 2003; Vogt & Knies, 2009). The clay mineral assemblage in the Laptev Sea is I>S>C>K (38.6>25.9>22.7>12.8 %; n =

160; **Table 1**; **Figures 5** and **6**). This assemblage is different than those found in previous studies where distinct eastern and western regions were recognized and defined by unique clay mineral assemblages (Table 1; Wahsner et al., 1999; Viscosi-Shirley et al., 2003).

In each of these studies, chlorite concentrations are greater in the eastern Laptev Sea. The source of this chlorite was determined to be input from the Lena and Yana Rivers (Wahsner et al., 1999; Rossak et al., 1999). In the current study, no appreciable increase in illite or chlorite is recognized for the eastern Laptev Sea. While these earlier studies identified unique eastern and western clay mineral assemblages for the Laptev Sea, they also lacked the sample distribution used in this data compilation (Wahsner et al. 1999; Viscosi-Shirley et al., 2003). Overall, the results of the current study are like those presented by Wahsner et al. (1999), who identified a similar assemblage in the western Laptev Sea.

3.3.5 East Siberian Sea

The East Siberian Sea shelf sediments have a clay mineral distribution of I>C>K>S (65.6>19.9>8.4>6.3 %; n = 84; **Table 1**; **Figures 5** and **6**), consistent with the results of previous studies (Kalinenko et al., 1996; Vogt, 1997; Wahsner et al., 1999; Kalinenko et al., 2001; Viscosi-Shirley, 2003). This region contains the highest average illite concentration in the Arctic (> 60 %) with a slight increase in the western East Siberian Sea. Chlorite concentrations average 20 % and show no distinct gradations. Kaolinite and smectite are both of minimal importance in this region with averages less than 10 %. Both Kaolinite and Smectite show a slight gradational increase to the far east that continues into the Chukchi Sea. The increase in kaolinite is likely sourced to the clastic sedimentary rocks of Wrangel Island. The elevated smectite concentrations are probably sourced to the volcanic belt of the Chukotka Peninsula material carried to the region through Bering Strait via Pacific Water inflow (Viscosi-Shirley et al., 2003). The Chukotka region is also enriched in chlorite, but an increase of this mineral is not noted in the eastern East Siberian Sea. The notable increase in smectite and not chlorite within the East Siberian Sea might be due to differential sorting, or preferential accumulation along the transport path (Chamley, 1989). The finer grained smectite can be transported in suspension by weak currents farther distances than the typically larger chlorite. Grain size data from the East Siberian Sea indicates that the fine fraction increases offshore, implicating differential sorting as a control on smectite distribution (Mammone, 1998; Viscosi-Shirley et al., 2003).

To the east of Wrangel Island there appears to be a broad smectite-enriched zone extending into the central Arctic (Mendeleev Ridge), however the sampling density in this region is insufficient to confirm this enrichment (**Figures 5** and **6**). This feature is possibly an artifact of the interpolating algorithm used to produce the distribution map. The elevated smectite found in the JPC9 core top is important to note as it far exceeds the average smectite concentration typical of central Arctic sediments (**Table 1**).

3.3.6 Chukchi Sea

The Chukchi Sea sediments express a clay mineral assemblage of I>C>K>S (60.5>21>10.4>8.2 %; n = 8; **Figures 5** and **6**). This assemblage is like those produced previously (Naidu & Mowatt, 1983; Wahsner et al., 1999; Schoster et al., 2000). The highest chlorite concentrations are found near the Bering Strait (up to 39 %), and these are likely delivered via the Pacific Water inflow from chlorite rich regions in the Bering Sea. The probable source of this enriched chlorite is the chlorite-rich Alaskan rivers (Naidu & Mowatt, 1983), and/or the volcanic belt of the Chukotka Peninsula (Viscosi-Shirley et al., 2003).

3.3.7 Beaufort Sea

The shelf region of the Beaufort Sea is shallow (<30 m depth) and extends along the North Slope of Alaska and Canada (width of 50-100 km). Additional islands and channels throughout the Canadian Arctic Archipelago (CAA) provide extensive coastline for erosion and subsequent transport via sea-ice to the central Arctic. While the areal extent of the shelf in this region is much less than those of the Eurasian Arctic, this region is an important source of sediment for the western central Arctic (Canada Basin), and the Beaufort Gyre (Reimnitz et al., 1998). The clay mineral concentrations of sediments entrained in western Arctic sea-ice are like the assemblage of the Beaufort Sea shelf (Reimnitz et al., 1998). For this study, low sampling distribution limits the potential for understanding mineral gradations through this region. It does, however, provide at least a baseline to begin the understanding of mineral distributions.

The Beaufort Sea shelf consists of the northern Alaskan region and the western CAA. The general clay mineral assemblage for the Beaufort Sea shelf is I>S>C>K (60.6>14.3>13.3>11.7 %; n=19; **Table 2**; **Figures 5** and **6**). The highest concentration of illite (82%) on the Beaufort shelf is found at the mouth of the Canning River which delivers sediments from the northeastern Brooks Range. Smectite concentrations are highest in the western CAA and in the mouth of the Colville River, North Slope, Alaska. Naidu & Mowatt (1983) identified this isolated sediment, rich in expandable clays as relict. Chlorite distribution is consistent and low, with elevated concentrations in the western region of the Beaufort shelf. This chlorite is enhanced by western Alaskan river inputs into the Bering Sea that enter the Arctic on the Pacific Water inflow and carried along the Arctic boundary current to the Beaufort Sea (Naidu & Mowatt, 1983). Kaolinite is low throughout the Beaufort Sea shelf, except for a small portion of northeastern Banks Island and in some northeastern Alaskan rivers (30 and ~10-15 %, respectively).

The largest input of sediment to the Beaufort Sea shelf is the Mackenzie River. This river has a discharge of 330 km^3 y^{-1} and delivers an estimated sediment load of 124×10^6 t y^{-1} (Gordeev, 2006). This total suspended matter (TSM) content is more than half of the annual input for the entire Arctic which totals 237×10^6 t y^{-1} (Stein, 2008). Given the large TSM flux to the Beaufort Sea, intuitively the shelf minerals should closely mirror the mineralogy of the river. The Mackenzie has a clay mineral assemblage of ICKS which is quite different from that of the shelf. There are several reasons for the disconnect between the mineralogy of the Mackenzie River and the Beaufort Sea shelf. First, most of the Mackenzie River sediment is moved to the east on the shelf and then into the Canada Basin via turbidity flows. Second, the northernmost gauging stations used to calculate the TSM are not at the mouth of the river, and it is estimated that only about half of the TSM load reaches the Arctic Ocean (Macdonald et al., 2004). Additionally, the influence of numerous small rivers draining into the Beaufort Sea is quite substantial, further diluting the local shelf clay mineral assemblage. Furthermore, it is shown that prevailing coastal currents control the clay mineral assemblage and dispersal along the North Alaska coastal region. Further north, on the outer continental shelf recognizable dispersal patterns are absent (Naidu & Mowatt, 1983). This lack of recognizable dispersal patterns indicates that the direct influence of riverine inputs into the Beaufort Sea are negligible, and away from the coast dispersal is much more complex than is currently understood. Possible reasons for this breakdown in dispersal patterns are seasonal effects on the sedimentary regime, random transport of clays by ice rafting, and/or erratic reworking and redistribution of sediments from occasional ice gouging (Naidu & Mowatt, 1983). With the breakdown of dispersal patterns so close to the shore, the ability to use these mineral provinces to track transport is limited.

A recent study sought to explore the mineral composition and distribution through the Amundsen Gulf and the associated Canadian Beaufort Shelf (Gamboa et al., 2017). These authors findings are important as they identify variations in mineralogy that can be applied to very specific source regions, however, their research is focused on a very small region in the western portion of the Canadian Arctic and still ignores large data gaps from the Canadian Arctic Archipelago.

3.3.8 Canadian Arctic Archipelago

The western Canadian Arctic is a prominent source region for sediment-laden ice in the western Arctic Ocean (Beaufort Sea and Canada Basin) (Clark et al., 1980; Naidu & Mowatt, 1983; Reimnitz et al. 1998). Sediment-laden ice transported in the Beaufort Gyre is intermittently incorporated into the Transpolar Drift where these two currents converge. Thus, sediments from North America can be transported and deposited into the eastern Central Arctic. In addition, sediments can flow directly into the eastern central Arctic and Fram Strait. The overall clay mineral assemblage for the Canadian Arctic Archipelago (CAA) is I>S>K>C (54.8>20.7>15.1>9.4 %; **Table 2**; **Figures 5** and **6**), and for northern Alaska I>S>C>K (59>12.5>12.5>9.8 %; **Table 2**; **Figure 6**).

The CAA can be divided into an eastern portion representing the Innuition ice sheet and a western portion representing the Laurentide ice sheet during glacial periods. While the clay mineral assemblages for the eastern and western regions are the same, there are small but notable differences. Relative to the western CAA, the eastern CAA exhibits lower illite, higher smectite, and slightly higher kaolinite concentrations (**Table 2**). Major ice streams originate in the CAA presumably imparting a mineralogical signature in the western Arctic Basin sediments.

3.3.9 Central Arctic

For this data compilation, the central Arctic sediments are samples taken from north of 83° N. Nearly all the samples in this study constrain only the eastern Arctic, or the Fram Basin and Nansen Basin east of Lomonosov Ridge. Based on 116 samples, the clay mineral assemblage is I>C>K>S (55>23.5>14.7>7 %; **Table 1**; **Figures 3** to **6**). The primary source of the illite in this region is from northern Greenland and Svalbard (Stein et al., 1994). Chlorite in the central eastern Arctic basin exhibits constant concentrations and is likely sourced to northern Greenland and the Laptev Sea. Kaolinite in this region is sourced to Franz Josef Land and the Barents Sea. Smectite appears to be of minor importance in this region of the Arctic but is sourced to the Laptev Sea. The low smectite concentration in this region is peculiar considering the eastern Arctic Basin lies directly in the path of the TPD which transports sediment laden ice from the smectite-enriched regions of the Kara and Laptev Seas to the Fram Strait.

Table 1. Clay mineral assemblages for the Eurasian Arctic. Data from three studies are listed (Wahsner et al., 1999; Schoster et al., 2000; Viscosi-Shirley et al., 2003). Primary differences: the Barents Sea clay mineral assemblage differs from that published by Vogt & Knies (2009) (data not shown), in the Kara Sea a eastern and western distinction is not recognized, and the eastern and western Laptev Sea distinction is not identified in the current study. The probable reasons for these differences are both the number of samples used to produce the distributions and potential bias introduced by sample clusters. For instance, focused sampling of the Franz Josef Land and St. Anna Trough region in the Barents Sea can bias the assemblage to overestimate the kaolinite concentration.

EURASIAN ARCTIC OCEAN SHELVES

		Eurasian Arctic Shelves	Barents Sea	Kara Sea		Laptev Sea		East Siberian Sea	Chukchi Sea	Central Arctic	All Samples
				West	East	West	East				
Wahsner et al. (1999)	**Illite**	48.6	55.5	38	19	40	49	69	57	53.8	-
	Chlorite	19.5	19.9	15	12	22	21	20	25	23	-
	Smectite	20.8	11.9	38	60	26	19	4	9	9	-
	Kaolinite	11.6	12.7	10	9	14	11	8	9	14.8	-
	Assemblage	**ISCK**	**ICKS**	**ISCK**	**SICK**	**ISCK**	**ICSK**	**ICKS**	**ICKS**	**ICKS**	-
	n	382	127	41	20	48	35	20	17	91	-
Schoster et al. (2000)	**Illite**	-	-	33		40	48	69	57	56	-
	Chlorite	-	-	19		22	22	19	25	22	-
	Smectite	-	-	33		23	18	4	9	7	-
	Kaolinite	-	-	15		15	13	8	9	16	-
	Assemblage	-	-	**SICK**		**ISCK**	**ICSK**	**ICKS**	**ICKS**	**ICKS**	-
	n	-	-	-	-	-	-	-	-	-	-
Viscosi-Shirley et al. (2003)	**Illite**	-	-	-	-	~ 35	~ 63	~ 62	~ 51	-	-
	Chlorite	-	-	-	-	~ 14	~25	~ 23	~ 23	-	-
	Smectite	-	-	-	-	~ 39	~ 7	~ 9	~ 20	-	-
	Kaolinite	-		-	-	~ 7	~ 7	~ 7	~ 7	-	-
	Assemblage	-	-	-	-	**SICK**	**ICSK**	**ICSK**	**ICSK**	-	-
	n	-	-	-	-	12	18	20	15	-	-
Current Study	**Illite**	45.3	48.7	26.9	32.5	37.6	39.3	65.6	60.5	55	48
	Chlorite	19.9	19.8	15.7	16.4	22.8	22.6	19.9	21	23.5	20
	Smectite	21.7	16.6	44.7	40.7	25.5	26.2	6.3	8.2	7	19
	Kaolinite	13.1	14.9	12.7	10.5	14.2	11.9	8.4	10.4	14.7	13
	Assemblage	**ISCK**	**ICSK**	**SICK**	**SICK**	**ISCK**	**ISCK**	**ICKS**	**ICKS**	**ICKS**	**ICKS**
	n	818	410	109	26	64	96	84	8	116	1040

Table 2. Clay mineral assemblages for major Amerasian sources and regions. Sample distributions for these regions are limited, thus these assemblages are only first-order assessments. Note: the highest illite concentrations are found in the Beaufort Sea and western Canadian Arctic Archipelago, the highest chlorite is found in the Greenland Sea and sourced to metamorphic terrain of northern Greenland, the highest smectite values are found in the eastern Canadian Arctic Archipelago from basaltic outcroppings on Ellesmere Island, and the highest kaolinite concentrations are found in the eastern Canadian Arctic Archipelago. If these clay mineral concentrations are pervasive in these regions it is yet to be fully documented.

AMERASIAN ARCTIC OCEAN SHELVES & ISLAND CHANNELS

	Amerasian Arctic	**Greenland Sea**	**Canadian Arctic Archipelago**			**Northern Alaska**	**Alaskan Rivers**	**Beaufort Sea**
			undivided	**West**	**East**			
Illite	59.3	59.2	54.8	60.3	50.4	59	59.6	60.6
Chlorite	14.2	19.3	9.4	10.7	11.1	12.5	23.2	13.3
Smectite	14.4	11	20.7	15.7	21.8	12.5	8.8	14.3
Kaolinite	12	10.5	15.1	13.3	16.6	9.8	8.4	11.7
Assemblage	**ISCK**	**ICSK**	**ISKC**	**ISKC**	**ISKC**	**ISCK**	**ICSK**	**ISCK**
n	28	56	13	11	5	9	10	19

Sea-ice production and transport to the central Arctic is strongest along the Eurasian Arctic shelf. The Laptev Sea accounts for more sea-ice production and output than all other Eurasian seas combined (Alexandrov et al., 2000). From the Laptev Sea shelf, ice enters the Transpolar Drift and is transported towards Fram Strait. Based on this production, output and transport it would be expected that the Laptev Sea mineral assemblage of I>S>C>K would be found in the eastern central Arctic. Instead the general assemblage of the central eastern Arctic is I>C>K>S, suggesting the importance of ice rafting to the overall modern central eastern Arctic sediment budget is low (Stein et al., 1994; Wahsner et al., 1999; Viscosi-Shirley et al., 2003). In the past ice rafting was much more important to the central Arctic sediment budget, especially during cooler periods. Alternatively, this disconnect between the mineralogy of the proximal Eurasian shelf and that eastern Arctic Ocean basin could be due to an underestimation of North American IRD contribution. Dirty ice flows carrying high volumes of sediments sourced to North American regions have been identified in the central Arctic, indicating that these regions could be much more important to the central Arctic sediment budget than previously thought (Darby et al., 2011). Selective entrainment in sea-ice of coarse material or early melt-out of fine material could also be invoked to explain the discrepancy between clay minerals of the shelf and eastern Arctic basin. The most logical explanation for this change in clay mineral assemblage for the eastern central Arctic is perhaps a stronger input from North American and Greenland sources and/or a reduced influence of sea-ice transport during interglacials or both.

There is limited data available for the western Arctic, but for at least one sample from the Mendeleev Ridge, the mineral assemblage is I>S>C>K (49.5>28.5>12.5>9.5 %; **Figures 5** and **6**). The assemblage from the Mendeleev Ridge matches the clay mineral assemblage of the Laptev Sea. This smectite concentration is four times the average of the eastern Arctic, showing the influence of source proximity. While most likely from a Laptev Sea source, a substantial portion of this increased smectite in the western central Arctic could also be from North American sources as this sample lies in the convergence zone of the Beaufort Gyre and the Transpolar Drift. An increased sampling distribution would be necessary for this to be confirmed.

3.3.10 Pyrophyllite

Pyrophyllite clay is identified throughout the Beaufort Sea, CAA, Svalbard, and Franz Josef Land source regions in variable concentrations (**Figure 8**). The presence of pyrophyllite in the western central Arctic is a firm indication of North American sources. In the eastern central Arctic, the presence of pyrophyllite could be confusing as high concentrations were identified in the Svalbard and Franz Josef Land regions. North American pyrophyllite is identified in sources from Eastern Chukchi Sea and northern Alaska, and primarily the Mackenzie River delta. The highest pyrophyllite concentration is identified in the deltaic sediments of the Mackenzie River, reaching ~17 % of the clay mineral fraction. To the east, elevated pyrophyllite concentrations have been identified in the Western Ellesmere, Axel Heiberg, and Ellef Ringnes Islands.

In this study, pyrophyllite might be misidentified talc, either from physical modification through sample processing due to identification inefficiencies in the mineral quantification software and the structural similarity of these two 2:1 sheet silicate monoclinic clays. Sources for pyrophyllite have been previously identified in Devonian or Mississippian conglomerates from the Brooks Range of Northeast Alaska where samples contain up to 30 % (by weight) pyrophyllite (Reed & Hemley, 1966). The material from this region is drained into the Beaufort Sea via the Kekiktuk River, Colville River, and other minor rivers draining the Brooks Range. Tosca et al. (2011) speculated that the elevated pyrophyllite found in the Mackenzie River sediments came from outcrops of Neoproterozoic strata of the Ogilvie and Mackenzie Mountains of the Yukon Territory (Tosca et al., 2011).

The only Eurasian region recognized in this study as bearing pyrophyllite is the in samples bounding the Franz-Victoria Trough, between Svalbard and Franz Josef Land. In this region pyrophyllite concentrations are more than 10% of the clay fraction. The most likely source is the eastern portion of the

Svalbard Archipelago. Talc bearing nodules have been identified in marine carbonates in the Hunnberg, Grusdievbreen, and Svanbergfjellet formations of Svalbard (Knoll & Swett, 1990; Tosca et al., 2011).

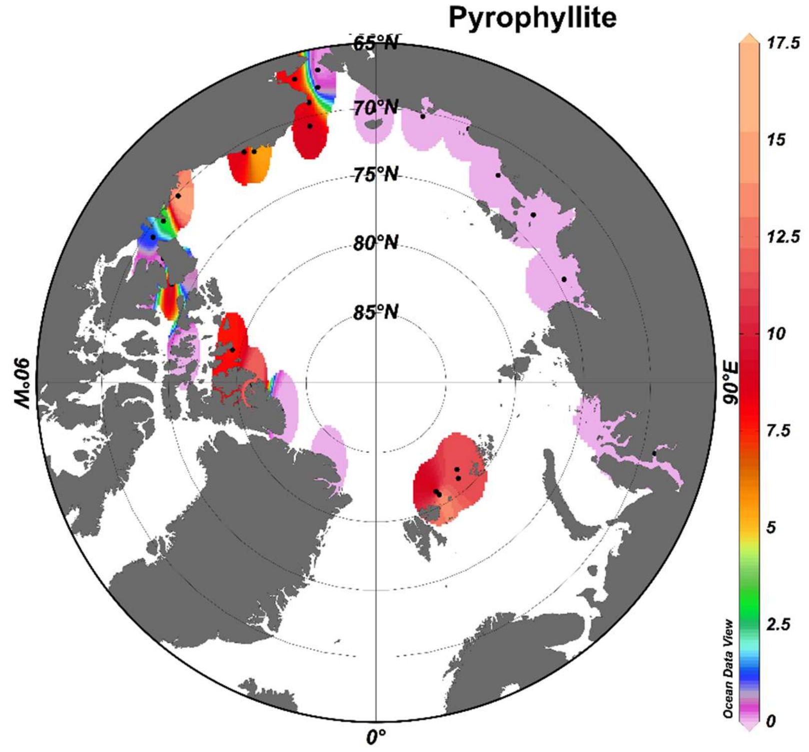

Figure 8. Distribution of pyrophyllite. Largely confined to the Amerasian Arctic with (in decreasing order) the Mackenzie River, Svalbard (Franz-Victoria Trough), eastern CAA, eastern Chukchi, and eastern Banks Island the most prominent sources. There is the possibility that talc was modified during sample processing and misidentified as pyrophyllite.

3.4 Non-Clay Mineralogy Results and Discussion

Information about the circum-Arctic distribution of non-clay mineral phases has been limited due to the lack of an efficient method for analyzing bulk mineralogy. Knowledge of non-clay mineralogy had been limited to heavy mineral and lithologic compositions attained through point counts of coarse material (Bischof et al., 1996; Bischof and Darby, 1997; Krylov et al., 2007). The geographic sampling distribution in this study limits the inferences that can be made about the mineral distribution but nevertheless provides insights into prominent mineral phases for select regions, specifically the underrepresented regions of North America.

For the non-clay minerals, significant minerals are addressed regarding their circum-Arctic distribution. Significant minerals are those with high overall concentrations and/or those exhibiting considerable spatial gradation. Minerals meeting these criteria could potentially be used as provenance indicators or for identifying changes in sediment transport pathways. For each mineral, only a brief discussion is provided, as a comprehensive discussion is beyond the scope of this dissertation. All concentrations mentioned are based on non-clay percentages rescaled to 100 %, to remove the clay mineral percentages.

3.4.1 Carbonates

Carbonates, especially dolomite, have long been recognized in central Arctic sediment records, as has the potential use in provenance determination. Major carbonate signals in central Arctic sediments are manifested as pink-white layers that are evidence for large-scale ice-rafting events or glacial lake outbursts of the Laurentide Ice Sheet (Clark et al., 1980; Polyak et al., 2004; Adler et al., 2009; Rasmussen & Thompsen, 2013; Bazhenova et al., submitted). This study further confirms this finding by identifying very high concentrations of dolomite in the western Canadian Arctic Archipelago (**Figure 9**). Additionally, major carbonates are identified in the eastern CAA, Ellesmere Island (Figure 8).

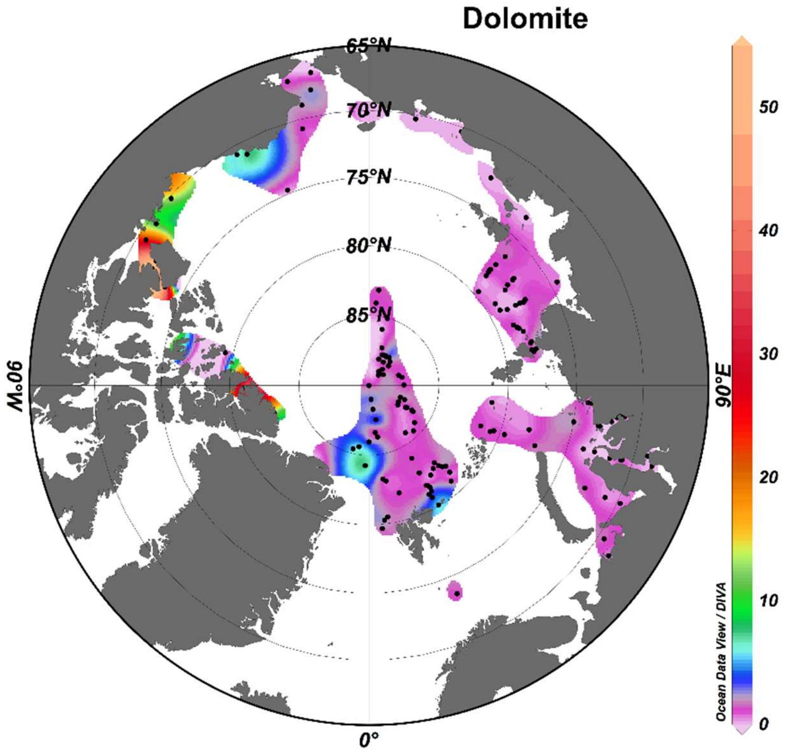

Figure 9. Distribution of dolomite for 34 circum-Arctic source samples (this study) and supplemented with data from Vogt (1997). Highest concentrations are found in the western and eastern Canadian Arctic Archipelago (most notably Victoria Island). Aside from local outcrops of Svalbard, dolomite is devoid in the Arctic outside of the Canadian Arctic Archipelago. Map generated with Ocean Data Viewer (Schlitzer, 2012).

Dolomite concentrations of > 40 %, and as high as 51%, are found in sediments originating from Victoria Island. Additionally, in the Amundsen Gulf, west of Victoria Island, dolomite concentrations are as high as 24 %. Appreciable levels of dolomite are found in only a few other circum-Arctic regions. The Mackenzie River delta is characterized by dolomite concentrations of nearly 20 % that decreases offshore to 13 %. The source of this Mackenzie River dolomite is an extension of the same Paleozoic carbonate platform that characterizes much of the western Canadian Arctic Archipelago. In Nansen Sound, the channel separating Ellesmere and Axel Heiberg Islands, a dolomite concentration of 35.6% is found. The source of this dolomite/carbonate is extensive outcrops of Paleozoic carbonates (Christie, 1964). Of these main dolomite sources, the Victoria Island source likely dominates the carbonates found in central Arctic sediments due to the higher volume of ice flow from this region relative to the Nansen Sound and Peary Channel (Stokes et al., 2005; Margold et al., 2015). Numerous studies utilizing the Fe-oxide fingerprinting technique show a strong Banks and Victoria Island signal in dirty sea-ice, marginal sediments and central Arctic sediment records (Darby & Bischof, 1997; Darby, 2003; Darby & Zimmerman, 2008; Darby et al., 2011; Darby et al., 2015). Dolomite is also found in Paleozoic rocks along the northern Svalbard archipelago, and Neoproterozoic marine carbonates are found throughout portions of Svalbard (Knoll & Swett, 1989; Vogt, 1997; Vogt et al., 2001). In terms of the central Arctic sediment budget, inputs from the Svalbard region are probably negligible but could provide a substantial input to Fram Strait sediments.

3.4.2 Tridymite

Tridymite is a high temperature polymorph of silica that is typically associated with felsic or siliceous volcanic deposits. The mineral tridymite is enriched in the surface sediments of the East Siberian and Laptev Seas and in parts of the Beaufort Sea, while being devoid in most other Arctic regions (**Figure 10**). While the data is limited, the distribution of tridymite implies that this mineral has potential to serve as a provenance indicator. The primary sources for tridymite in the western Arctic are the Devonian volcanics in the Brooks Range, Alaska and subsequent delivery by the major rivers of this region (Colville River in particular). In the Eurasian shelves, tridymite is likely sourced primarily to the Siberian Trap Basalts. Tridymite, although typical of felsic volcanics, has been identified in the trap basalts of Siberia (Lightfoot & Hawkesworth, 1997).

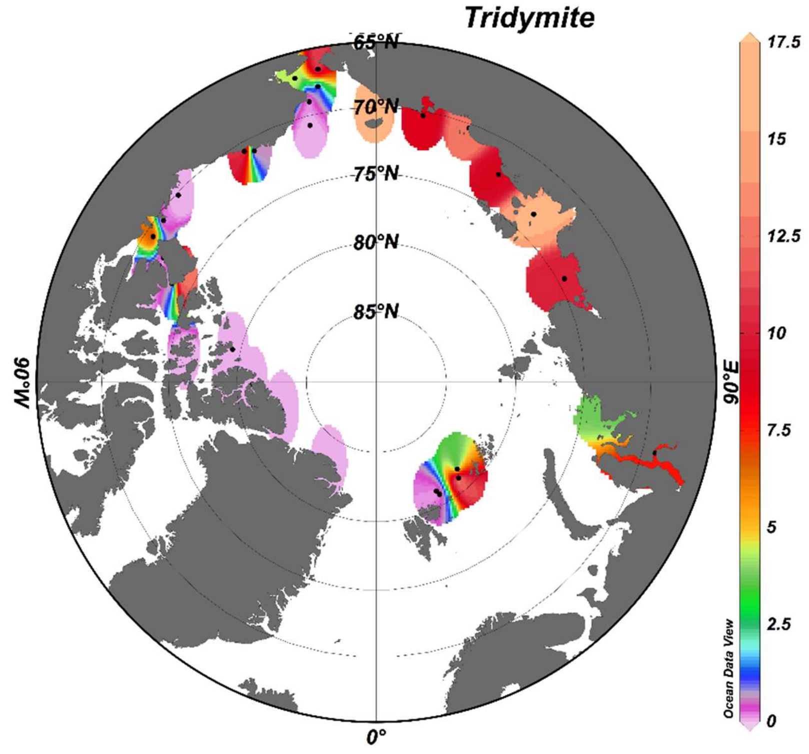

Figure 10. Distribution of the mineral Tridymite for the circum-Arctic region. Tridymite follows similar trend of plagioclase feldspar and is potentially useful as a provenance indicator. High concentrations are found in the Laptev and East Siberian Seas and are sourced to the major clastic terrains of the Siberian Hinterland. Map generated using Ocean Data Viewer (Schlitzer, 2012).

3.4.3 Opal

For the circum-Arctic, opal concentrations are very low (**Figure 11**). This limited distribution is expected due to the ice-limited growth of silica bearing organisms. From the regions sampled, only three exhibit appreciable amounts of opal mineraloids. The highest concentrations are found in the western Arctic region in the Canadian Arctic Archipelago (**Figure 11**). Namely, Ellesmere, Axel Heiberg, and Bathurst Islands have opal concentrations of up to 16.8 %. Additional regions of elevated opal are the Chukchi-northern Alaska area and the Franz-Victoria Trough, with the opal production in these areas probably a result of silica carapaces of organisms carried on the inflowing Pacific and Atlantic Waters, respectively.

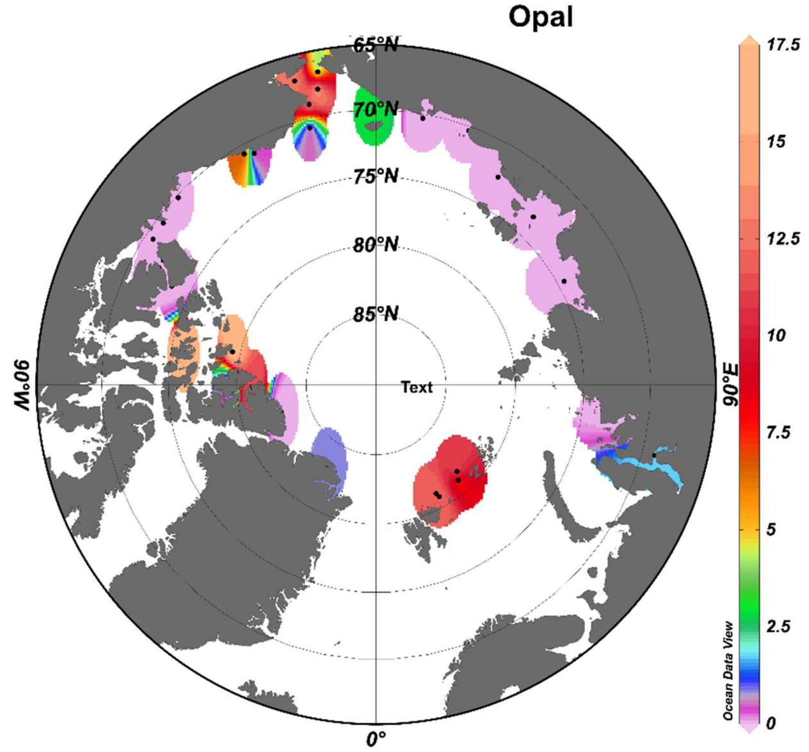

Figure 11. Distribution of opal minerals for 34 circum-Arctic source samples. Highest concentrations are found in the eastern Canadian Arctic Archipelago (Ellesmere, Ellef Ringnes, and Bathurst Islands), Franz-Victoria Trough (separating Svalbard and Franz Josef Land), and Chukchi-northern Alaska regions. Elsewhere, concentrations are low or absent. Map generated with Ocean Data Viewer (Schlitzer, 2012).

3.4.4 Zeolites

The abundance of zeolite is taken as the summation of the following phases: clinoptilolite, analcime, mordinite, natrolite, and chabazite. Zeolites are indicative of basaltic terrains and/or authigenic production volcanogenic material such as ash and tuff (Velde, 1985). Concentration of zeolite are low in the circum-Arctic, averaging just 3.9% (**Figure 12**). The few exceptions where zeolite concentrations are elevated are from a few samples around Alaska, in the eastern Canadian Archipelago, and the region between Svalbard and Franz Josef Land (Franz-Victoria Trough) (**Figure 12**). Due to the restricted sampling density a full distribution cannot be constrained, but sources of this material can be suggested.

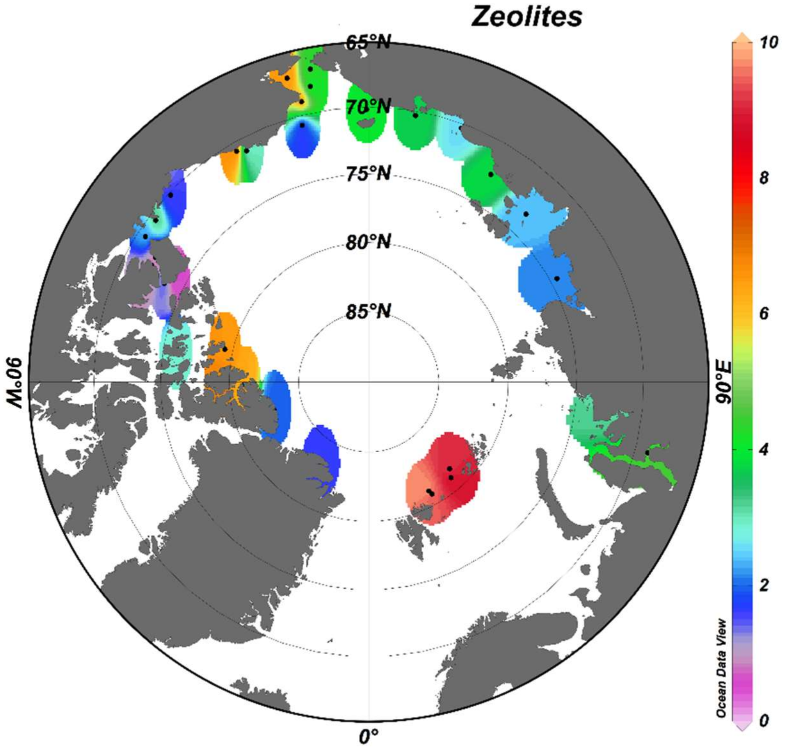

Figure 12. Distribution of zeolites for 34 circum-Arctic source samples. Highest concentrations are found in the eastern Canadian Arctic Archipelago (Ellesmere, Ellef Ringnes, and Bathurst Islands), Franz-Victoria Trough (separating Svalbard and Franz Josef Land), and Chukchi-northern Alaska regions. Elsewhere, concentrations are low. Map generated with Ocean Data Viewer (Schlitzer, 2012).

The highest concentrations of zeolite found within the samples from this study were in the Franz-Victoria Trough region of the northern Barents Sea. Here concentrations range from 8.6-10 % of the non-clay fraction (**Figure 12**; n=4). In marine environments, zeolites are commonly found where wind-blown volcanic ash predominates over river-borne detrital clays (Velde, 1985). Authigenic zeolite formation from basalt-derived sediments from the adjacent landmass is a possibility, such as the Cretaceous basalts of north and eastern Svalbard (Maher, 2001). Explosive volcanic activity of the Gakkel Ridge could serve as an additional source of zeolite at least to the eastern central Arctic (Sohn et al., 2008). Determining the actual source would require more extensive and increased sampling resolution of surface sediments in this region. A widespread occurrence would likely indicate an Icelandic source while a more localized distribution would be indicative of weathering of Cretaceous basalt outcrops on northeastern Svalbard.

Other regions of elevated zeolite are found along the Alaskan coast as well as in the eastern Canadian Archipelago (**Figure 12**). Along the northern coast of Alaska, elevated zeolite of 6.8 % is found east of the Colville River mouth. In northwestern Alaska zeolites are present, with concentration around 6.5 %. In the eastern Canadian Archipelago, zeolite concentrations range from 6.3 to 6.8 % on western Ellesmere, Axel Heiberg, and Ellef Ringnes Island. This region corresponds to Cretaceous-age flood basalts, sills and dikes that might serve as the primary source of zeolites in this western Canadian region (Maher, 2001). It has been observed that the zeolite clinoptilolite regularly occurs in palygorskite-rich (chain-clay) sediments (Couture, 1977; Nathan & Flexer, 1977; Velde, 1985). For each of the above-mentioned zeolite-enriched zones, at least one sample is associated with a palygorskite enrichment as well as the presence of clinoptilolite.

Due to the unique and limited distribution of zeolite in circum-Arctic sediments, this mineral has potential as a provenance indicator. However, the main drawback of the zeolite mineral species is its authigenic occurrence which could confound any provenance determined by its presence. More information regarding the speciation of zeolite in these unique regions and the recognition of weakly authigenic phases would be needed to use this mineral to accurately determine provenance. Furthermore, the speciation of zeolites may be indicative of sediment diagenesis, but further investigation is required. Whether or not the occurrence of zeolite minerals can be accurately identified to the level needed to constrain provenance, will need further research.

3.4.5 Amphibole and Pyroxene

Amphibole and pyroxene are minerals primarily associated with mafic rocks but also many felsic rocks, typical of igneous and some metamorphic terrains. Previously, enhanced concentrations of these two minerals have been identified across the Eurasian shelf, especially in the East Siberian, Laptev, and Kara Seas (Darby et al., 1989; Behrends et al., 1996; Behrends et al., 1999; Schoster et al., 2000). The distribution of amphibole and pyroxene is localized, indicating potential for use as a provenance indicator. Low overall concentrations preclude these minerals as strong candidates for provenance, due to dilution away from sources. In some cases, during major IRD events for instance, these minerals can be used to indicate source. For instance, a suite of heavy mineral data from the CAA has been used to identify major ice rafting events from sediment records in the Canada Basin (Zauderer, 1982). In this study, an outdated age model implied that the primary source for major IRD events in the Canada Basin was the CAA and northern Greenland throughout the last 3 million years. Using more updated sedimentation rate estimates for the Canada Basin would place these IRD events in the last 200 kyr (Backman et al., 2004).

These minerals, and others, have been used to identify the initiation of perennial sea-ice in the Arctic Ocean by recognizing a change from pyroxene to amphibole on the Lomonosov Ridge drill site (Arctic Coring Expedition or ACEX). This change indicated a shift from western Laptev Sea sources to eastern Laptev Sea source that would require sea-ice to travel for more than a year to reach the ACEX site and therefore survive summer melting, implying the initiation of perennial sea-ice (Krylov et al., 2008).

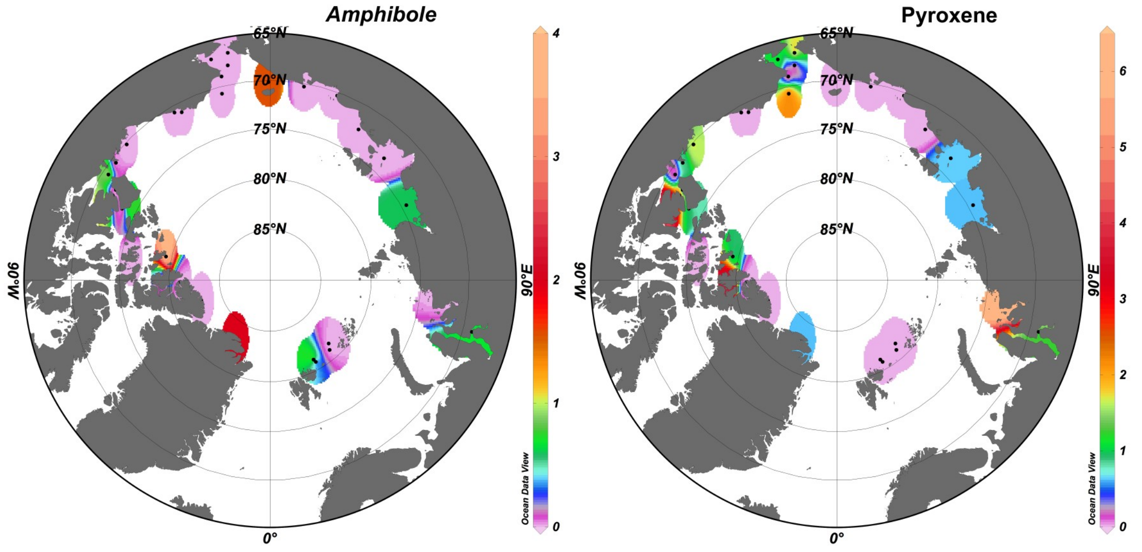

Figure 13. Distribution of amphibole (left) and pyroxene (right). Indicative of mafic terrains, the only regions of appreciable content are found in the Kara Sea (amphibole and pyroxene), Laptev Sea (amphibole only), eastern East Siberian Sea (amphibole only), northern Greenland (amphibole only), the eastern Canadian islands and the western Canadian islands (pyroxene only). Maps generated using Ocean Data Viewer (Schlitzer, 2012).

In the current study, high concentrations are not identified in locations that have been previously shown to have coarse-grain abundances in excess of 30 %, such as the western East Siberian Sea and eastern Laptev Sea (**Figure 13**; Behrends et al., 1999). The elevated amphibole concentrations centered at the confluence of the Laptev and East Siberian Seas are not recognized in the samples of the current study. Amphibole shows a concentration range of 0-4% with the highest concentration found on Ellef Ringnes Island and Wrangel Island (**Figure 13**). Elevated concentrations are noted in the eastern CAA, but knowledge of distribution is weak due to limited sampling distribution and the concentration of the coarse fraction is unknown. The difference in this study and previous studies might imply the abundance of amphibole is grain size dependent, with larger concentrations found in the coarser fraction. Alternatively, this could be the result of insufficient sampling.

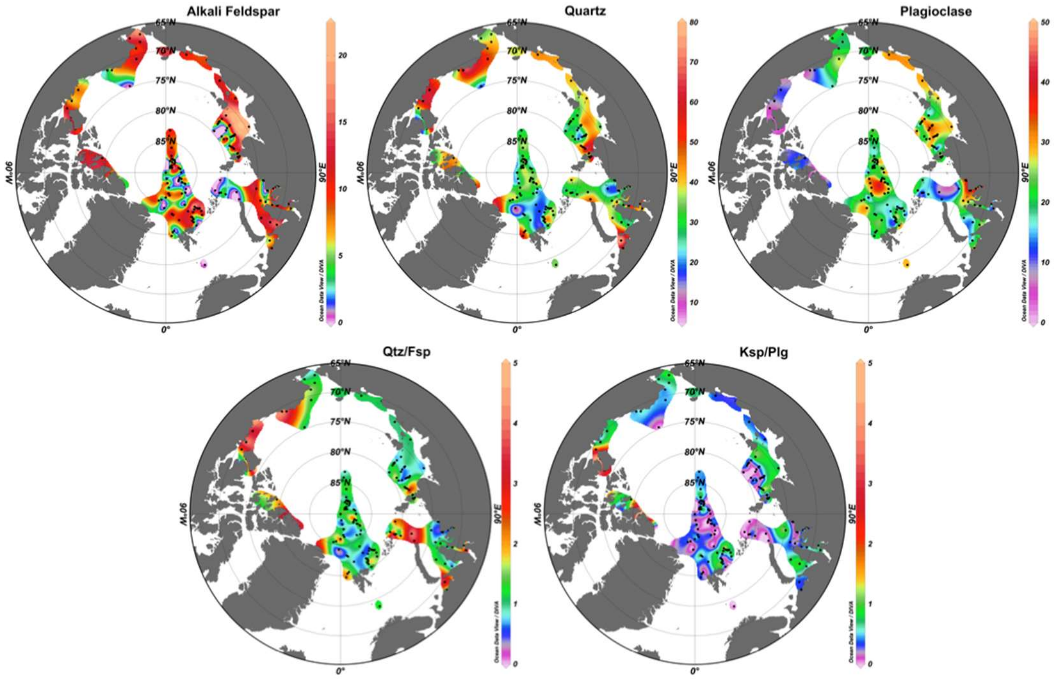

Figure 14. Distribution of quartz, alkali feldspar, and plagioclase feldspar content of the < 45 μm fraction (upper row). Distribution maps of the Qtz/Fsp and Ksp/Plg ratios (lower row). Most of the samples in the eastern central Arctic, along 0° longitude and from the northern Laptev Sea are from Vogt (1996) and are of the bulk fraction.

3.4.6 Quartz

Quartz is ubiquitous in Arctic Ocean sediments, consistently comprising most of the non-clay fraction. The only exception to this is several pink-white layers in which carbonates dominate. There are few distinguishing features of quartz that can be used to indicate provenance. There are some instances in the sediment record where quartz content reaches percentages that exceed 90 %. In these cases, there are only a few locations that can produce quartz in such high volumes. The high quartz-bearing regions are restricted to the Mesozoic clastics and Cenozoic quartz sands on the west central Canadian Arctic Archipelago and the sedimentary and volcanic formations draining into the Laptev and Kara Seas (Bischof, 2000). In some cases, features of the quartz grains can yield additional information regarding provenance. For instance, Kara Sea quartz grains from the Ob and Yenisei Rivers are typically coated by iron-oxide/hydroxide that impart reddish stain (Bischof, 2000). The presence of microfeatures, or striations, on the surface of the quartz grains can indicate a glacial origin (St. John, 2008; St. John et al., 2015).

Additional quartz sources are identified near the Mackenzie River, the eastern CAA, and northern Greenland (**Figure 14**). Elevated quartz in these regions is generally consistent with the geology of these terrains. The eastern Canadian Arctic (especially Ellef Ringes Island) and northern Greenland are comprised of largely clastic terrains which are defined by elevated quartz contents (**Figure 2**; Bischof & Darby, 1997). The elevated quartz of northern Alaska is anomalous, as the Mackenzie River primarily drains a carbonate platform and not necessarily associated with a quartz-rich terrain (**Figure 2**; Reeder et al., 1972). The elevated quartz in this northern Alaska region could be from the nearby Canadian Arctic Archipelago, from an unknown source within the Mackenzie River drainage basin, or a current transported signal from a northwestern Alaskan river/source (possibly the Colville and nearby rivers). It has been suggested that material exiting from the Mackenzie River and the eastern CAA moves eastward, possibly parallel and close to the North American Arctic continental margin, towards the Fram Strait (Bishof & Darby, 1997).

3.4.7 Alkali and Plagioclase Feldspar

The concentration of total feldspar in this study ranges from 8 – 49.7 % of the non-clay fraction. The highest concentrations are found in the Eurasian Arctic and typically exceed 30 %, with values in the Kara and Laptev Seas >40 % (**Figure 14**). Given the strongly igneous terrain drained by the Ob, Yenisei, and Khatanga Rivers it is unsurprising that high concentrations of both K-feldspar and plagioclase feldspar are found in these seas (Levitan et al., 1996).

The average alkali feldspar (K-feldspar) concentration based on the samples in this study was 11 % (range: 2.8-21.9 %). Surprisingly, the highest recorded K-feldspar concentration was identified in a sample from Victoria Island in the western Canadian Arctic, an island noted for its extremely high levels of carbonate. The source of this western Canadian K-feldspar is possibly authigenic formation from interactions of alkali-rich saline waters with the dolomitic terrain (Deer et al., 2001), and the abundant late Proterozoic Franklin Large Igneous Province of basalt and dolerite dike swarms of Victoria and Banks Island (Palmer et al., 1983; Ernst et al., 2016). In the eastern Canadian region K-feldspar concentrations are typically around the average of 11 %, these are sourced to the clastics of Axel Heiberg, Melville, and Ellef Ringnes Islands. A possible source for this K-feldspar is material from the Mackenzie Large Igneous Province held in Laurentide Ice Sheet tills. Eurasian shelf concentrations of K-feldspar are only above average in the Kara and Laptev Seas. The East Siberian Sea is associated with average levels of K-feldspar and sourced to the clastic platforms of that region. A sample from Wrangel Island, in the East Siberian Sea, indicates above average K-feldspar. The Chukchi Sea is associated with northward decreasing concentrations of K-feldspar, with local maximums appearing to be near the Bering Strait. The source for this signal is likely the volcanic material from the volcanic belt of the Chukotka Peninsula carried north and into the Arctic along the Pacific Water inflow. Aside from the above average concentrations in the western Canadian islands, the Beaufort Sea and northern Alaska have low concentrations of K-feldspar.

Plagioclase is strongly indicative of Eurasian sources (**Figure 14**; Herman, 1974). The source of this material is the Putorana Flood basalts of western Siberia, and the sporadic volcanic of northern Siberia and the volcanic belt of eastern Siberia. The highest plagioclase concentrations are found in the eastern Kara Sea and the eastern East Siberian Sea. In addition to the high concentrations of the Eurasian Arctic, above average plagioclase is also found in the Chukchi Sea and in northern Greenland where, for the latter intrusive igneous rocks are prevalent. The widespread occurrence of the plagioclase in the Eurasian Arctic, and the average to low concentrations elsewhere make this mineral ideally suited for distinguishing sediment provenance. However, using plagioclase alone to isolate a specific source is not possible due to its prevalence across the Eurasian Arctic shelf. Thus, the addition of other variables is necessary to pinpoint specific sources.

3.4.8 Ksp/Plg and Qtz/Fsp

Plotting the ratio of potassium feldspars and plagioclase feldspars (Ksp/Plg) against the ratio of quartz and total feldspar (Qtz/Fsp) provides some indication of provenance (**Figure 15**; Vogt, 1997). Qtz/Fsp is more qualitative than the quartz signal alone, because the latter is so ubiquitous within Arctic sediments. Also, the concentration of quartz relative to feldspar is somewhat higher in the North American region. Still the spread of the Qtz/Fsp does not show much regarding regional distinctions, only the Beaufort Sea sediments appear to be consistently quartz-enriched. Groupings might be identifiable; however, the sampling distribution in this study is not enough to determine these groupings with statistical significance. The higher North American Qtz/Fsp ratio appears to be boosted by values found in the Beaufort Sea tied to the high quartz content of Mesozoic and Cenozoic clastics of the northern Canadian Arctic (Bischof, 2000). Only a few samples in the Eurasian shelves exhibit higher than average Qtz/Fsp, and these appear to be localized in the Kara Sea, Svalbard, and Franz Josef Land.

Ksp/Plg is more illuminating than Qtz/Fsp in terms of determining source provenance. Two distinct end-member provinces are identified based on the Ksp/Plg. The first distinction is North American sources associated with a high Ksp/Plg ratio (mean = 1.8; **Table 3**), indicating a preponderance of Ksp relative to Plg. In general, sediments of the Eurasian Arctic Shelf exhibit low Ksp/Plg (mean = 0.4; **Table 3**) due to the prominence of plagioclase feldspars in the volcanic-rich terrain of northern Siberia. The Qtz/Fsp ratio is variable around the Arctic but averages 1.3 and 2.7 for the Eurasian and North American sources, respectively (**Figure 14** and **15**; **Table 3**).

Previously, Qtz/Fsp and Ksp/Plg data were used to show that the groupings of central Arctic sediments were very similar to the Eurasian shelf sediments (the Laptev Sea) (**Figure 15a** and **b**; Vogt, 1997; Stein, 2008). The similarity of Qtz/Fsp and Ksp/Plg signals between the central Arctic sediments and Eurasian shelf sediments indicates potential provenance. The current study proposes Eastern Canadian sources as a potential source of these central Arctic mineral signals (**Figure 15c**). Given the low smectite concentration in the central Arctic sediments, it is possible that these sediments can be traced back to the Eastern CAA where, relative to the Kara and Laptev Seas, smectite is somewhat less abundant.

The Qtz/Fsp and Ksp/Plg signals were investigated for cores JPC22 and JPC9 from the eastern and western Arctic basins, respectively. The ratios within these cores are like those identified for the Eurasian shelves (**Table 3**). This similarity supports the idea that the Eurasian shelves are the dominant source for central Arctic sediments through sea-ice and current transport (Pfirman et al., 2004). It should be noted that most of the central Arctic samples lie in the pathway of the TPD that carries ice rafted sediments from the Eurasian Arctic shelves towards Fram Strait.

Table 3. Average Quartz/Feldspar (Qtz/Fsp) and Alkali Feldspar/Plagioclase Feldspar (Ksp/Plg) ratios for surface sediments of the Eurasian, North American, and Central Arctic regions. Data from Vogt (1997) and supplemented by this study.

	Qtz/Fsp	Ksp/Plg
Eurasian	1.3	0.4
N. American	2.7	1.8
East Central Arctic	1.1	0.4

While the Eurasian source signature dominates modern surface sediments, it is probable that the North American influence on central Arctic sediments has varied in the past. Major climatic shifts such as ice sheet disintegration, glacial lake outbursts, and possibly large-scale ice rafting events imparted a Canadian signature in the central Arctic sediments. This Canadian influence has been well documented; specifically, Pink-White carbonate-rich layers from western Canada have been identified throughout central Arctic sediment records (Clark et al., 1980; Darby et al., 1989; Stein et al., 2004; Polyak et al., 2004).

Using the presence of calcic smectite in a core from the Yermak Plateau, Fram Strait, an increased influence of material sourced to the CAA can be established. Intervals of elevated calcic smectite are identified at 41.4, 64.7, 81.3, 86.7, and 138 ka correspond to Stages 3, 4, 5a, 5b and 6, respectively. Of these dates, Stages 4, 5b, and 6 correspond to periods that are associated with increased glacial ice inputs.

There are outliers that are not grouped with a strongly Eurasian source (stars in **Figure 15b**). Of these sample sites, three are located proximal to the Kara Sea and Franz Josef Land. It is likely that these sites received sediment inputs from Eurasian sources, most probably from localized outcroppings with enhanced concentrations of Ksp. One sample, however, was far removed from the proximity of the Eurasian shelves and in the direct pathway of the TPD (PS2196-3; 85.9618 N, 0.165 E; Ksp/Plg = 2.43, Qtz/Fsp = 0.49). Mixing of two or more sources can be invoked to explain these ratios, perhaps from the Kara/Laptev Seas with the Beaufort/Chukchi Seas, consistent with the mixing of the BG and the TPD.

The distinction in the Eurasian and North American Ksp/Plg ratios implies that this might serve as an indicator for source. Using alternative methods in concert with the Ksp/Plg ratio, such as other mineral phases, clay minerals, or geochemistry might be useful in further refining the source provenance. In the following section, a basic paleoreconstruction of two cores using the Ksp/Plg ratio is explored.

3.5 Implications on previous uses of mineralogy for provenance

3.5.1 Smectite as an indicator of provenance

The clay mineral smectite has been utilized as an indicator of inputs from Eurasian sources, namely the Kara and Laptev Seas (Vogt and Knies, 2009). The identification of abundant smectite in the circum-Arctic has been highlighted and brings into question the validity of using smectite to determine provenance. The speciation of smectite phases, however, might be suitable for use in provenance studies. As described in this study, the smectite group consists of sodic, calcic, and Fe-rich smectites, saponite, hectorite, and various illite-smectite mixed-layered clays (Eberl, 2004). By examining the distribution of these phases, regions may be characterized by subgroups of these smectite phases. There is evidence to suggest that RockJock program used to quantify these minerals is suitable for group identification but is limited in its ability to accurately identify individual phases or species of a mineral group (Bahzenova, 2012). Regardless, the data produced for the current study identifies source-specific smectite phase assemblages that could potentially be used for regional characterizations and provenance.

In general, the presence of calcic smectite can be used to differentiate between Eurasian and North American smectite sources. The Eurasian region sources largely contain saponite, hectorite, Fe-rich smectite and mixed-layered clays; no calcic smectite was identified in any of the Eurasian sources analyzed. The North American region smectite consists of calcic smectite plus similar phases found in the Eurasian region. In general, the amount of saponite and hectorite in the North American region is less than what is found in Eurasia. Mixed-layered clays in North American source samples are prevalent, as is Fe-rich smectite. Appreciable concentrations of calcic smectite are only identified in North American sources (**Table 4**).

Table 4. Smectite phase contribution to the primary smectite sources determined in this study. Only samples with > 8 % smectite of the total bulk sediment were selected. The clearest distinction is the presence of Calcic Smectite in the North American region and its absence in the Eurasian region.

Smectite Phase Distribution

Region	*Sub-Region*	*Sample ID*	*Smectite % of Bulk Sediment*	*Sodic Smectite*	*Calcic Smectite*	*Fe-Rich Smectite*	*Hectorite*	*Saponite*	*Mixed-Layered Clays*
Eurasian	**Kara Sea**-Ob River	OB67	16.3	-	-	38.4	10.1	15.7	35.8
	Kara Sea-Yenisei River	YR93	14.5	-	-	41.8	18.4	14.2	25.5
	Laptev Sea-West	NW063-173	8.9	-	-	69.7	9	21.3	-
	East Siberian Sea	NW063-64	10.4	-	-	-	31.1	23.3	45.6
	East Siberian Sea	NW063-90	12.3	-	-	35	6.5	27.6	30.9
North American	**E.CAA**-Ellesmere Island	EL7	8.5	-	-	17.6	-	-	82.4
	E.CAA-Bathurst Island	95BJB0003	9.1	-	44	-	12	-	44
	E.CAA-Ellef Ringnes Island	89200	11.1	-	-	50	-	-	50
	W.CAA- Amundsen Gulf	0303-CA06	15.3	-	29.3	15.6	12.9	10.2	32
	W.CAA- Amundsen Gulf	0303-CA18	9.1	-	31.4	11.6	31.4	25.6	-
	W.CAA- Beaufort Sea/Colville River	72-AJT-30/41	8.1	-	35.8	64.2	-	-	-

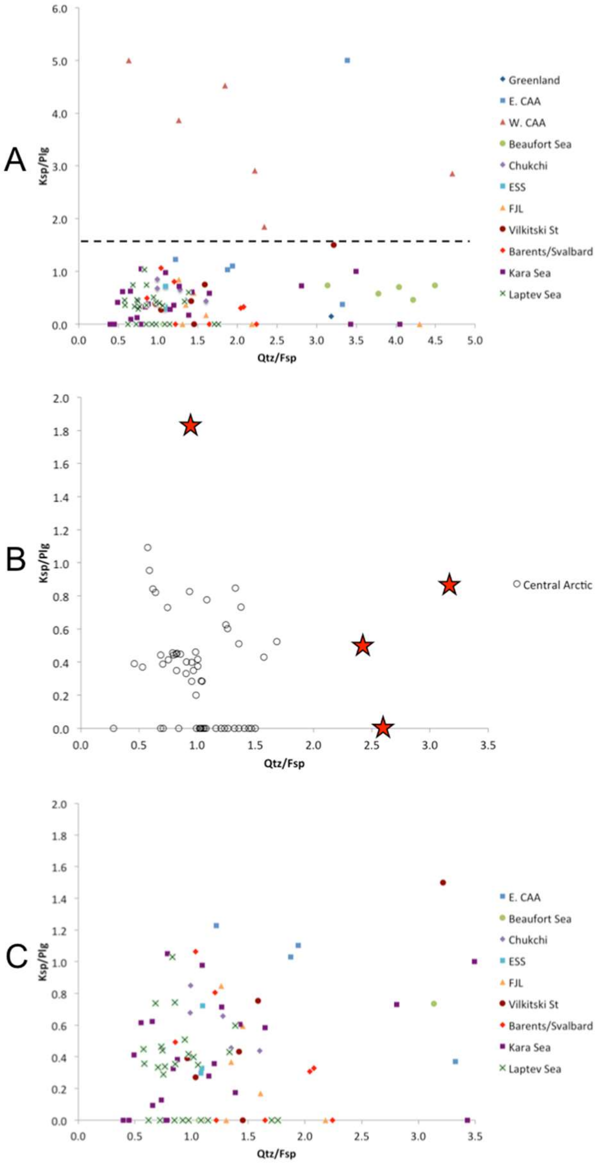

Figure 15. Plot of the ratios K-feldspar/Plagioclase feldspar and Quartz/total feldspar for the (A) entire circum-Arctic, (B) the central Arctic, and (C) sources with ratios like the central Arctic. The dashed line in plot A indicates the separation of western CAA sources from most of the remaining Arctic. Geographic groupings are probable, but more data are necessary for confirmation. Feldspars dominate Eurasian Arctic shelf sediments, with the plagioclase phase indicative of the mafic terrain in that region. Northern Alaska is associated with higher quartz relative to feldspar, with a predominance of plagioclase over potassium feldspar. Plots B and C are expansions of plot A, and do not have the same scales In plot B, the stars indicate central Arctic samples that fall outside the general ranges for Qtz/Fsp and Ksp/Plg ratios for the Eurasian Arctic. While these signatures could originate from localized sources in the Kara Sea region, they could also be sourced to CAA sources. The apparent groupings in plot B do not show any grouped provenance signatures.

3.5.2 Application of Ksp/Plg to sediment Records

The difference between the Ksp/Plg ratio between the Eurasian and North American regions implies that this ratio might be a suitable indicator of general source (**Figure 16**; **Table 3**). This ratio could be particularly important for identifying major glacial events or estimating the influence of Eurasian and North American sources in central Arctic sediment records. Here, two records are examined based on the Ksp/Plg ratio and compared with the provenance determined from Fe-grain fingerprinting (Darby et al., 2015).

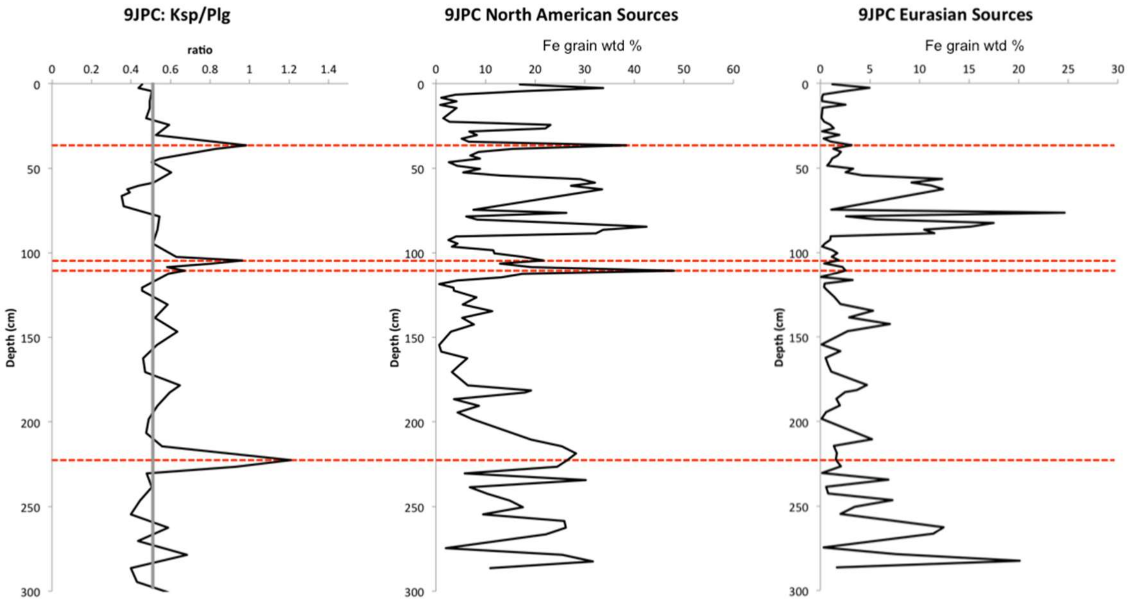

Figure 16. Ksp/Plg plots for core JPC9 compared with the North American and Eurasian source signals as determine though Fe-grain fingerprinting (Darby et al., 2015). The vertical grey line indicates a conservative estimate of Ksp/Plg separating the pure Eurasian signal (< 0.5) and that with a potential North American influence. North American and Eurasian source provenance plots are based on the weighted percent of Fe-grain matches to these regions. The red dashed lines high-light peaks in Ksp/Plg that correspond to North American source specific events, with minimal Eurasian influence.

In the western central Arctic, HLY0503-JPC9 was taken from the Mendeleev Ridge. This core is ideally situated near the confluence of the TPD and BG, where these two currents will intermittently mix

(Reimnitz et al., 1998; Rigor et al. 2002; Darby, 2003). Because of this location, material originating from both Eurasian and North American sources will be prominent. North American sources should be particularly prevalent during past cool intervals when large armadas of sediment-laden icebergs were being released from the Innuition and Laurentide ice sheets. The North American provenance is particularly evident for several intervals in JPC9 where Ksp/Plg exhibits sharp increases. For instance, intervals at ~36, ~105, and ~224 cm, likely represent large deglacial events tentatively assigned to MIS 2 to 1, MIS 4 to 3, and MIS 5b to 5a, respectively.

A core from the western central Arctic (HLY0503-JPC22; Yermak Plateau, Fram Strait) was examined for Ksp/Plg variations. Due to the core location in the TPD path that primarily consists of Eurasian source material, it was expected that the Ksp/Plg would be low and thus strongly Eurasian-dominated. For the most part, the Ksp/Plg ratio is low throughout the core except for ~100-150 cm depth where there is a jump in Ksp/Plg ratio (**Figure 17**). This Ksp/Plg increase corresponds with peaks in North American sources and troughs in Eurasian sources based on Fe-grain provenance (**Figure 17** and **18**; Darby et al., 2015). Therefore, even small increases in Ksp are magnified by a reduced input of Eurasian Plagioclase. This increase in Ksp could be indicative of increased material exiting the CAA, perhaps during glacial periods.

Plotting the Ksp/Plg against age (age acquisition discussed later in this dissertation) shows that the large sudden increase in Ksp/Plg corresponds to MIS 2 (e.g. the last glacial period). In addition, there are at least 2-3 additional peaks in the Ksp/Plg ratio corresponding to 9.6, 33.4, and 100.4 kyr (**Figure 18**). These three events might indicate short-term ice-sheet disintegration/deglaciation, like Heinrich events. These dates do not correspond with any documented Heinrich event. Within error limits of the JPC22 age model, the 33.4 ka event is close to the timing of Heinrich event 3 (~31 kya; Hemming, 2004) or the Heinrich event 4 (38 and 37 kyr; Hemming, 2004 and Bond & Lotti, 1995, respectively). Alternatively, this ~33 ka event could indicate pulses of ice associated with the initial ice sheet growth on North America. The 9.6 ka event might correspond to the Younger Dryas or the 8.2-kyr cooling events

(Bond et al., 1997; Alley et al., 1997). Regardless of the timing, the source is well constrained to be from the North American region.

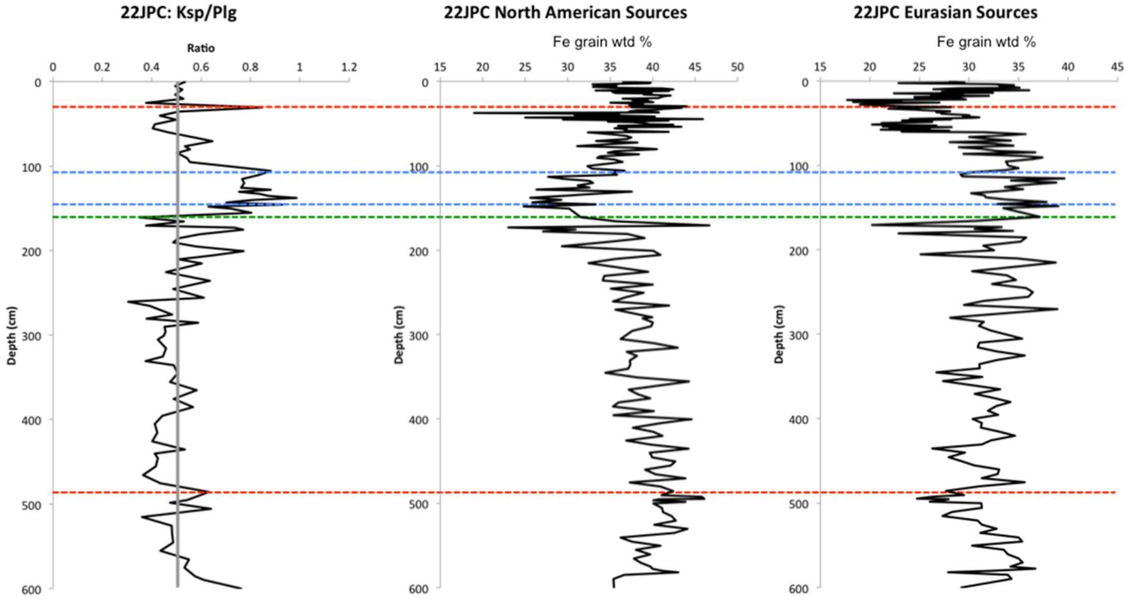

Figure 17. Plot of Ksp/Plg vs depth compared with the weighted percent of North American and Eurasian Fe-grain provenance (Darby et al., 2015). A strong increase in North American source and concurrent decrease in Eurasian source implies a strong North American event, perhaps ice sheet disintegration, melt water event, surge of glacial ice, or ice sheet resurgence. A low Ksp/Plg ratio indicates increased input form Eurasian sources, this corresponds to low North American sources and high Eurasian sources is indicative of increased input. Red dashed lines indicate probable North American events, with the MIS 2 (Last Glacial Maximum) events highlighted with the blue dashed lines. The single green dashed line is indicative of a major Eurasian event, possibly a major ice rafting event or the initiation of the Eurasian ice sheet (which might imply that during Stage 2, the Eurasian Ice Sheet growth precedes its North American counterpart).

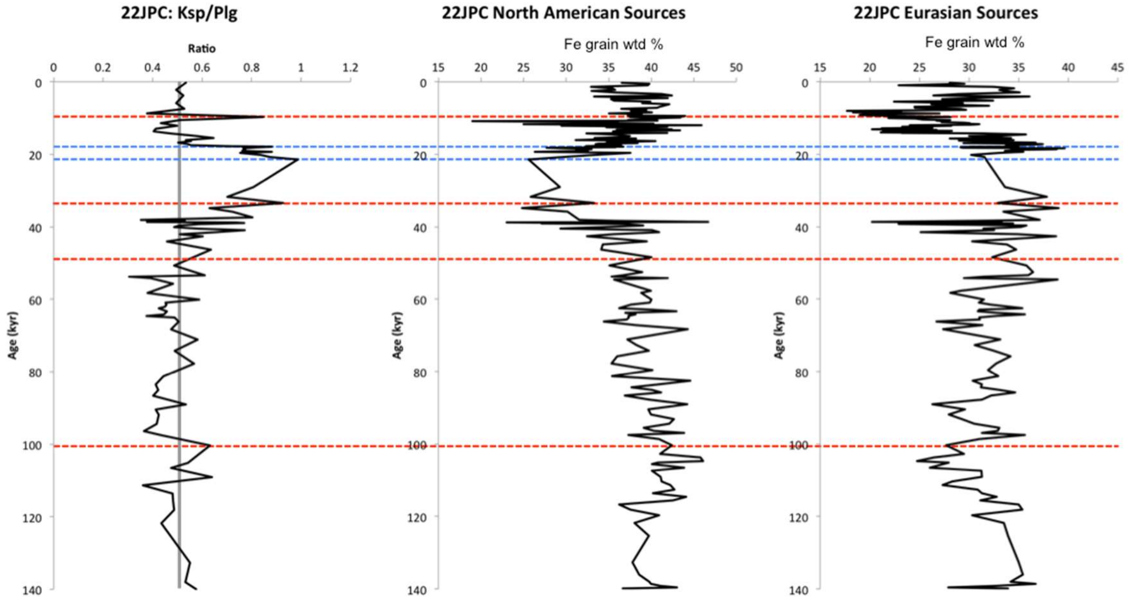

Figure 18. Plot of Ksp/Plg vs Age compared with the weighted percent of North American and Eurasian Fe-grain provenance (Darby et al., 2015). A strong increase in North American source and concurrent decrease in Eurasian source implies a strong North American event, perhaps ice sheet disintegration, melt water event, surge of glacial ice, or ice sheet resurgence. Events with only speculative causes are highlighted with red dashed lines. Blue dashed lines indicate ice sheet activity during MIS 2 or the MIS 2/1 transition.

Down core variations in Ksp/Plg and Qtz/Fsp show promise at identifying basin wide events that can be used to correlate cores from the eastern and western Arctic Basins (**Figure 19**). For a North American source signature to reach both the Mendeleev Ridge and the Yermak Plateau in Fram Strait, it would have to be a large-scale event; such as glacial disintegration, surges, melt water pulse, or isolated but major ice stream flows. For the latter, additional minerals or Fe-grain provenance may give some indication of a more precise source that can potentially elucidate the timing of ice sheet dynamics.

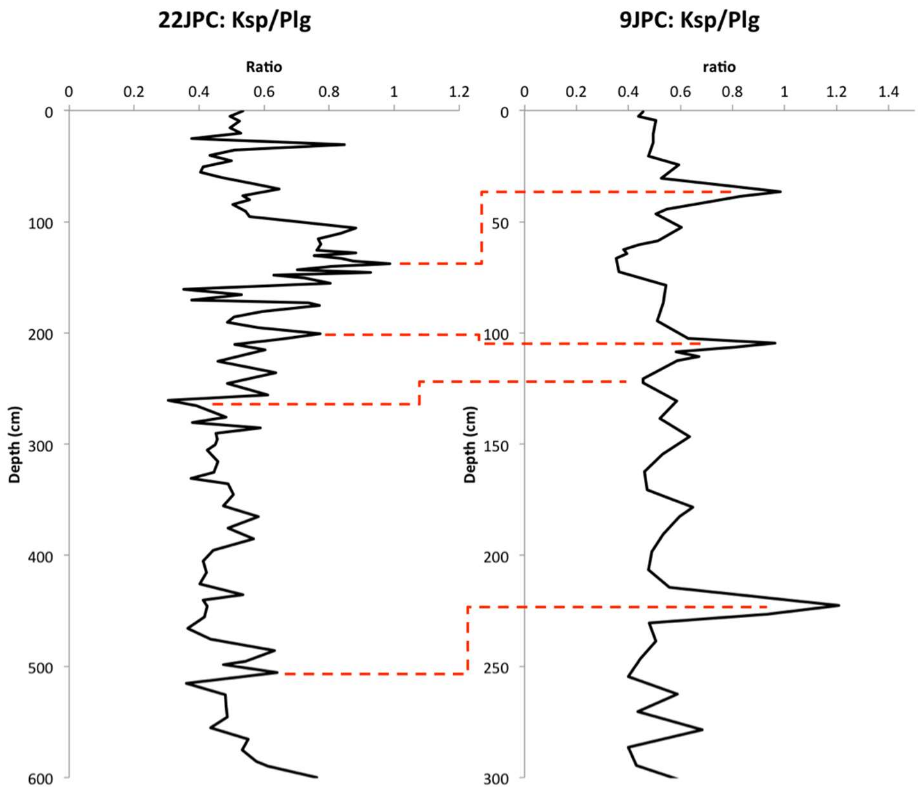

Figure 19. Ksp/Plg ratio for HLY0503-JPC22 (Fram Strait) and HLY0503-JPC9 (Mendeleev Ridge). Red-dashed lines show possible correlations indicating the potential for basin-wide correlations. These are not confirmed and are only shown to highlight the potential. Additional variables are needed in order to confirm correlations.

3.6 Conclusions

- The North American gap in circum-Arctic clay mineral distribution data is addressed.
    - Significant concentrations of illite are identified near the mouth of the Colville River and in northern Greenland. For these regions, illite is a potentially useful mineral for provenance determination. Illite speciation may be a useful proxy for unmixing source contributions in the northern Alaska and Greenland regions.
    - Appreciable levels of smectite are identified in the CAA, specifically Ellesmere and western Victoria Islands. Kaolinite-enriched sediments are also identified in the CAA, especially portions of Axel Heiberg, Ellef Ringnes, and northern Banks Island. Therefore,

at least for the western Arctic Ocean, the occurrence of smectite is not necessarily an indicator of Eurasian Arctic inputs. There appears to be a distinction between Eurasian and Amerasian smectite phases, with calcic smectite only identified in North American sources. Further determination of smectite speciation may be used to determine provenance. Likewise, the identification of kaolinite can no longer be assumed to come from Franz Josef Land.

- This work provides a foundation, or baseline, of source bulk mineralogy with which a further understanding of changing source provenance and transport pathways might be developed. The results presented here strongly support the Fe-oxide fingerprinting method of Darby et al. (2015), providing additional evidence for the efficacy of both approaches to provenance determination.
- Several minerals have been introduced as potentially useful for identifying source provenance, like the distribution of carbonate/dolomite. Pyrophyllite, tridymite, amorphous minerals, zeolites, and feldspars all show unique circum-Arctic distributions. Whether or not the distributions of these minerals across the Arctic are extensive enough that they prove to be useful, remains unknown. Amorphous minerals and zeolites, however, are subject to diagenesis and therefore may not prove useful.
- The identification of strongly contrasting feldspar phases between the North American and Eurasian regions allow for their use in discerning major inputs from these regions. Overall, correlating sediment records from the western Arctic to records of the eastern Arctic is very difficult due to the differing sedimentation rates in these basins. The Ksp/Plg and Qtz/Fsp ratios indicate that there might have been basin wide events that can potentially be used to correlate between the eastern and western basins.
- While the addition of North American source material adds to the overall understanding of circum-Arctic mineral distribution, drawbacks are still evident due to low sampling density. For instance, if a major source of a mineral were missed then the mineral distribution through this region would be

underrepresented. Also, due to the sediment size restrictions in this study, comparisons with other non-clay studies of Arctic mineralogy are limited (as was the case for the amphiboles and pyroxenes).

4 JPC22, FRAM STRAIT: AGE MODEL, MINERAL VARIATION, IMPLICATIONS FOR ICE SHEET TIMING AND ORIGIN OF HEINRICH EVENTS.

4.1 Introduction

The Fram Strait is the only deep-water connection to the Arctic Ocean, and the only constant opening to the world ocean. During peak glacial periods, when sea level drops more than 60 m, the Pacific Ocean connection is closed, and massive ice sheets block Atlantic-Arctic water exchange through the channels of the Canadian Arctic Archipelago (CAA). As the only persistent region where warm southern waters meet the cool waters of the Arctic and melt-out ice-rafted detritus (IRD), the Fram Strait likely represents one of the only regions with continuous, and high-resolution records of Arctic Ocean history. The sedimentation history is tied closely to the extent and duration of the polar ice front in this region, as ice rafting is the dominant process of sediment delivery. This characteristic highlights the importance of the Fram Strait region in respect to the paleoceanographic understanding of the Arctic Ocean region.

Near JPC22, before, during and after the LGM, ice-free conditions have been noted for the eastern Fram Strait region (Kneis and Stein, 1998; Müller et al., 2009; Jakobsson et al., 2014; Colleoni et al., 2016; Stein et al., 2017; Knies et al., 2018). Polynya-type conditions are understood to have occurred off the margins along the northern Barents-Kara Ice sheet in the eastern region of Fram Strait (location of JPC22; **Figure 20**) as well as the East Siberian continental margin (Knies and Stein, 1998; Knies et al., 2000; Svendsen et al., 2004; Niessen et al., 2013; Colleoni et al., 2016; Stein et al., 2017; Knies et al., 2018). These ice-free conditions were likely variable and were probably the result of strong katabatic winds from the Barents-Kara Ice Sheet and East Siberian continental margin that pushed sea-ice away at the leading edge of the ice sheet (Niessen et al., 2003; Stein et al., 2017; Knies et al., 2018). A record of the extent of sea-ice in the Fram Strait has been examined using the IP_{25} and brassicasterol biomarkers produced by sea-ice-associated diatoms (Müller et al., 2009; Knies et al., 2018). During the past 30 kyr (including the LGM), a sea-ice front was present near Fram Strait, specifically around the Yermak

Plateau. Ice-free conditions were identified during the early warming at 14 ka, but seasonal ice has been persistent throughout Marine Isotope Stage 1 (0-14 ka) (Müller et al., 2009; Knies et al., 2018). More recently, and utilizing similar methods, Stein et al. (2017) have identified periods of ice-free conditions in along the northern boundary of the Barents and East Siberian Seas during the penultimate glacial and last interglacial. Thus, it is reasonable to presume that there has been constant sea-ice- and iceberg-derived sedimentation during both glacial and interglacial periods on the Yermak Plateau, although perhaps less during warm phases. Reduced ice conditions during interglacial periods are consistent with studies of sedimentation rates. The sediment accumulation rates in Fram Strait during glacial periods are more than twice those identified during interglacial periods (Hebbeln & Wefer, 1997).

The Yermak Plateau, located in Fram Strait, is a flat relatively shallow (~800 mwd) plateau surrounded by deep (>2000 mwd) basins. Such plateaus preclude the delivery of sand and gravel from landmasses directly by current transport, and therefore coarse sediment is primarily due to ice transport (Hevrøy et al., 1996; Levitan et al. 2002a). However, bottom currents can result in the redeposition of sediments on the Yermak Plateau specifically of the fine fraction, so care must be made to avoid confusion between redeposition and actual IRD signals. Sedimentation on the Yermak Plateau has continued unabated for the past 660 kyr (Flower, 1997). Therefore, the continuous IRD sedimentation of the Yermak Plateau implies this region provides an excellent record of glacial/interglacial variability.

Previous attempts at applying oxygen-isotope stratigraphy to sediment records from the Yermak Plateau have been difficult due to poor resolution and age anchors based on poorly understood paleomagnetic variations (Flower, 1996; 1997). This work expands on the findings of Xuan et al. (2012), who found that a magnetic-sourced grain size proxy closely mimics the global benthic δ^{18}O curve (**Figures 21** and **22**). These data are used to produce an age model for a Yermak Plateau sediment core. Sediment texture, provenance and mineralogy data are then examined in order to provide evidence to corroborate and/or refine the age model. The overarching goal is to provide a high-resolution record directly tied to the global oxygen-isotope record and well-established ages based on these isotopes in order to serve as a reference for other Arctic records. A secondary objective is to identify unique signals that, if accurately dated, can possibly be traced across the Arctic Ocean. These signals can then be used to apply this Fram Strait age model to central Arctic Ocean sediment records, a region in need of age control especially extending beyond the effective datable range of AMS-^{14}C. Furthermore, relative to one another, identified unique events can be used to differentiate between the dynamics and timing of Barents-Kara, Innuitian, and Laurentide Ice Sheets based on the timing of their IRD contribution to the sediment record.

4.2 JPC22 Age Model

The core HLY0503-JPC22 (hereafter JPC22) was taken from the western edge of the Yermak Plateau (80˚ 29.386' N, 7˚ 46.141' E) in 798 m water depth (**Figure 20**). The age model developed for JPC22 is based on the changes in the grain size of magnetite that mimics the global oxygen-isotope curve (Xuan et al., 2012) and is further expanded on in this paper. These authors identified a grain-size proxy for magnetite in the form of anhysteretic remanence susceptibility over total magnetic susceptibility (κ_{ARM}/κ). The κ_{ARM}/κ ratio closely resembles the stacked global benthic δ^{18}O record (**Figure 21**; Lisiecki & Raymo, 2005; LR04).

The similarity between these two curves is presumed to be due to sea level fluctuations during glacial periods where eustatic sea levels drop which in turn reduces the size and volume of the Arctic Ocean basin, constricts the current flow across the Yermak Plateau and increases the current velocity through funneling (Xuan et al., 2012). Thus, during a glacial interval there will be coarser magnetite, higher κ and lower κ_{ARM}/κ ratio in Fram Strait sediments as increased

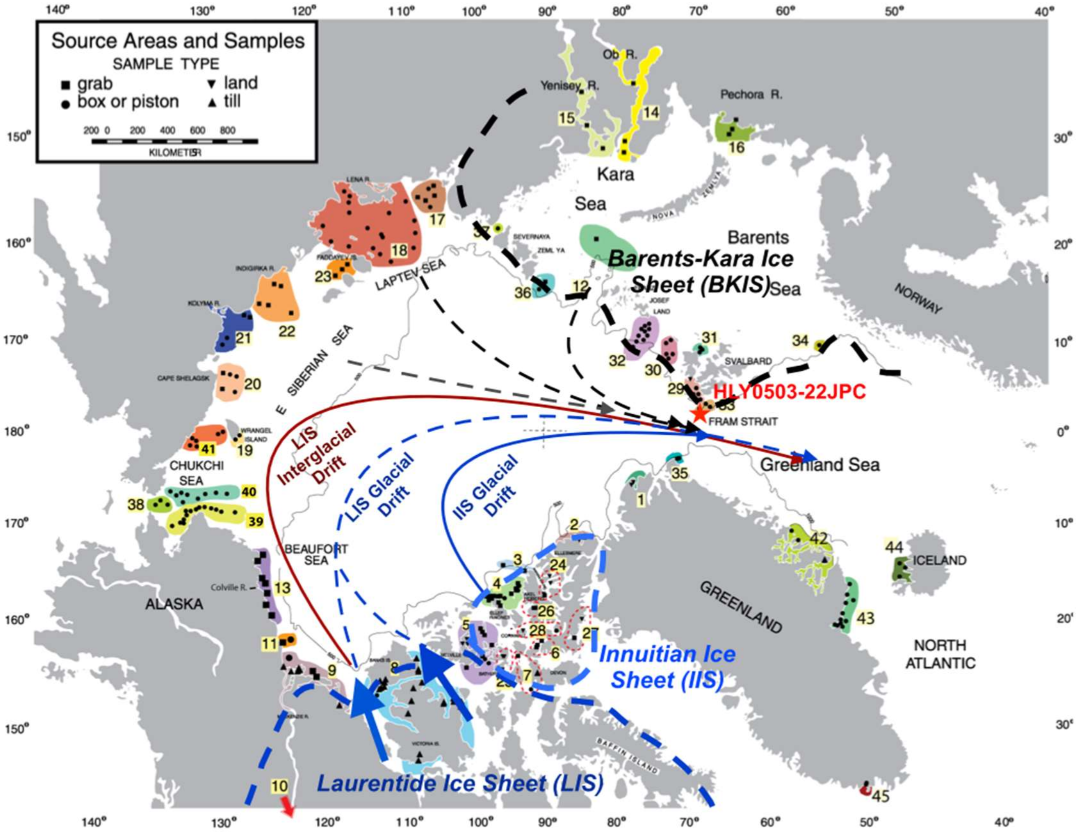

Figure 20. Map of Arctic Ocean, with the studied core HLY0503-JPC22 highlighted (red star). The broad dashed lines (blue, light blue, and black) estimate the boundaries of the major ice sheets that deliver sediment to the JPC22 core site (LIS, IIS, BKIS, respectively) (boundaries loosely based on those provided by Jakobsson et al., 2014). Major ice streams of the LIS are identified with large blue arrows (Stokes et al., 2005). The primary North American glacial/interglacial drift patterns are also labeled. The black and grey dashed line indicate the major currents that transport both materials originating from BKIS as well as the primary interglacial period sea-ice production zones of the Laptev and East Siberian Seas. JPC22 is situated in a region that will receive input from all major ice sheet zones. The Greenland Ice Sheet is not labeled. Assessment of Fe-oxides implies that Greenland is not a major source of material for core JPC22. Figure modified from Darby et al., (2002).

current velocities winnow the finer-grained materials from which most of the magnetic intensity is sourced. During an interglacial with higher sea levels, however, the Fram Strait current velocities decrease allowing for fine-grained material to accumulate, thus changing the magnetic susceptibility (Xuan et al., 2012).

The magnetic grain-size proxy record allows for the direct correlation of LR04 age model stack to JPC22, and thus the application of Marine Isotope Stages (**Figure 21**; Xuan et al., 2012). Where fauna was available for δ^{18}O analysis, the results confirmed the paleomagnetic proxy (Xuan et al., 2012). In addition, two MIS 1 samples at 100.5 and 138 cm were AMS-^{14}C dated to 15.34 and 18.50 ka, respectively. Using a reservoir correction of 440 years and the calibration of Nowaczyk et al. (2003), these ages are 17.71 and 21.35 ka, respectively (**Figure 21**, **Table 5**; Xuan et al., 2012). These dates also fit well with the paleomagnetic age model.

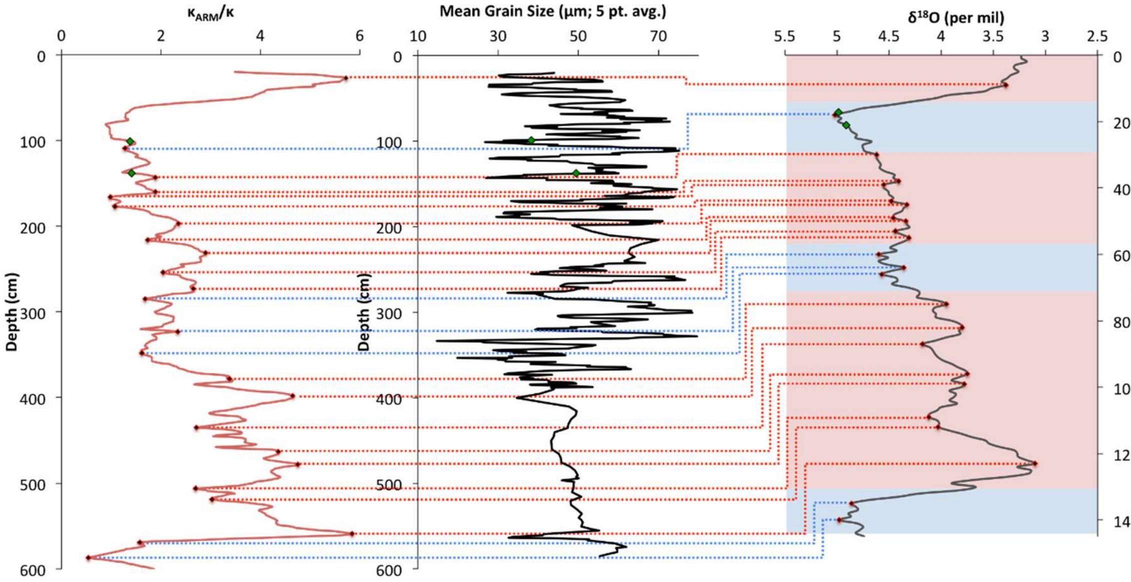

Figure 21. HLY0503-JPC22 plots of the magnetic grain size proxy κ_{ARM}/κ, a 5-point moving average of the mean grain size of bulk sediments, and the Lisiecki & Raymo (2005) benthic δ^{18}O curve. A total of 24 correlation tie points are identified (red/black diamonds), along with two AMS-14C dates (green/black diamonds; from Xuan et al., 2010). These correlation tie points are further denoted by color to represent warm and cold intervals (red and blue, respectively) based on the δ^{18}O ages. Warm (pink) and Cold (blue) intervals are identified in the δ^{18}O plot. In general, low κ_{ARM}/κ ratios correspond with increased grain size.

Each major peak in κ_{ARM}/κ, indicative of a finer grain size, correlates to troughs in δ^{18}O (peaks in Figure 4-2 due to reversed x-axis), each indicating a cold climate. In all, 24 correlation tie-points were identified, along with the two ^{14}C dates (**Figure 21**, **Table 5**). These correlation tie-points were then fit to the JPC22 record via a piecewise cubic hermite interpolating polynomial fit (PCHIP) to produce the age model shown in **Figure 22**. This interpolation method makes no assumptions about data outside the bounds of what is known. The κ_{ARM}/κ record was plotted with the JPC22 age model and yielded improved correspondence to the LR04 δ^{18}O record (**Figure 23**). The overall potential error for the JPC22 age model is tied to the instrument error for oxygen-isotope analyses in LR04 benthic stack; this error is estimated to be no more than 4 kyr (non-accumulating) for the last 1 Ma (Lisiecki & Raymo, 2005) Generally, the margin of error decreases for younger sediments. The interpolating process does not consider any of the processes that produce the data used, therefore there is not measure of uncertainty within the model. Standard error of the model must be assumed from the data used in the interpolation.

Table 5. Table of correlation points based on the similarities between the κ_{ARM}/κ magnetic grain size proxy of Xuan et al., (2012) and the benthic oxygen-isotope stack of Lisiecki & Raymo (2005). These correlation tie points are shown in figure X. Stars (*) denote AMS-^{14}C dated material (Xuan et al. 2012).

Table of Correlated Points

22JPC Depth (cm)	LR04 Age (kyr)	22JPC Depth (cm)	LR04 Age (kyr)
27	9	285	60
100.5	17.71*	323	64
109	18	348	66
138	21.35*	378	75
143	30	399	82
160	38	435	87
166	39	464	96
177	44	478	99
197	45	506	109
216	49	519	112
231	50	559	123
254	53	570	135
273	55	587	140

*Indicates radiocarbon date

4.2.1 Grain Size Variation in JPC22

Differentiating between sediment delivered via iceberg and sea-ice transport is difficult (Drewry, 1986; Polyak et al., 2010; St. John et al., 2015). For offshore sediment records collected from bathymetric highs, coarse sand-sized sediment is often interpreted as iceberg-derived rather than sea-ice derived (Polyak et al., 2010). But sea-ice can also transport coarse sand; although more often it is finer-grained than iceberg IRD (Darby, 2003; Darby et al., 2011). Thus, here the use of glacial intervals and coarse sand-sized IRD will be used to infer iceberg transport.

Using textural characteristics iceberg transport is identified as coarse dominant, sea-ice transport is presumed for fine sand dominant, and intervals with roughly equal parts fine and coarse sand are considered mixed. Thus, based on IRD texture and timing (i.e. whether it occurs during a glacial or interglacial), the probable mode of transport can be determined (Pfirman et al., 1989; Nürnberg et al, 1994). When the distribution of medium-coarse sand fraction (>250 µm) exceeds the coarse silt fraction (45-63 µm) during glacial periods, the inferred transport mode is by iceberg. Conversely, during interglacial periods, most IRD signals are presumed to be sea-ice derived. The only exception is if during interglacial periods, the coarse fraction greatly exceeds the coarse silt fraction then iceberg transport can be invoked as a major contributor to IRD transport. This simplistic approach provides only an estimate of the mode of ice rafting.

4.2.2 Fe Oxide Provenance and Mineralogic Variation

Given the lithological uniqueness of certain regions of the circum-Arctic, certain minerals can be utilized to determine the source of sediments in the Arctic sediment record. The most precise mineral-based method for elucidating sediment provenance is through Fe-oxide fingerprinting (Darby et al., 2015). This method compares and matches elemental chemistry of individual Fe-oxide (45-250 µm; ilmenite, magnetite, titanomagnetite, hematite, chromite, and exsolved phases of ilmenite and magnetite) determined via electron microprobe of Fe-oxides from the sediment record to a source database of more than 38,000 individual Fe-oxides to determine provenance. Possible diagenetic impact to the Fe-oxide minerals is avoided by analyzing only the unaltered portions of these grains, therefore assuring that the original source composition is identified.

Geographic coverage of Fe-oxide provenance has been consolidated through combining regional source areas into three primary ice sheet sources and two major sea-ice production zones: (1) Laurentide Ice Sheet (LIS), (2) Innuitian Ice Sheet (IIS), (3) Barents-Kara Ice Sheet (BKIS), (4) Laptev Sea (LS), and (5) East Siberian Sea (ESS) (**Figure 20**). The LIS group consists of source areas (SA) 8, 9, and 10, covering Banks and Victoria Islands and the Mackenzie River region (**Figure 20**). This region includes M'Clure and Amundsen ice streams which were highly active during previous glacial periods (Stokes et al., 2005; Stokes et al., 2009). The IIS group consists of SA 3, 4, 5, 6, 7, 24, 25, 26, 27, and 28 covering the regions of Ellesmere, Axel Heiberg and Ellef Ringnes Islands (**Figure 20**). This eastern CAA region is an important region for Fram Strait sediment during both glacial and interglacial periods (Darby et al., 2002; England et al., 2009). The BKIS group consists of SA 14, 15, 17, 18, 29, 30, 31, 32, 33, 36, and 37 covering the western Laptev, Kara, and Barents Seas (**Figure 20**). The contribution of IRD from these ice sheet regions is analyzed in JPC22 to interpret dynamics of ice sheet growth and retreat through glacial and interglacial periods. The latter, LS and ESS represent the zones of major sea-ice production and used to identify the source for major sea-ice events. The sources around Svalbard are also specifically examined to identify localized inputs to the JPC22 core site.

In addition, it has been shown that various circum-Arctic regions exhibit unique mineral signatures that can also be used to trace provenance (Vogt, 1997; Wahsner et al., 1999; Viscosi-Shirley et al., 2003; Section 2). Of note are the expandable clays and plagioclase feldspar indicative of the Eurasian region and the dolomite signal that correspond the Canadian Arctic. Other mineral signatures are of use, especially the ratios of potassium feldspar and plagioclase feldspar (Ksp/Plg) and quartz and feldspar (Qtz/Fsp) which show promise in differentiation between Eurasian and North American sources (Vogt, 1997; Section 2). Additional mineral ratios may serve as climatic indicators. Low ratios of kaolinite and chlorite (Kaol/Chl), smectite and kaolinite (Smec/Kaol), and smectite and illite + chlorite (Smec/Ill+Chl) have been applied as indicators of warm periods, and elevated ratios of Kaol/Chl as indicators of cool periods (Vogt, 1997; Levitan et al., 2002).

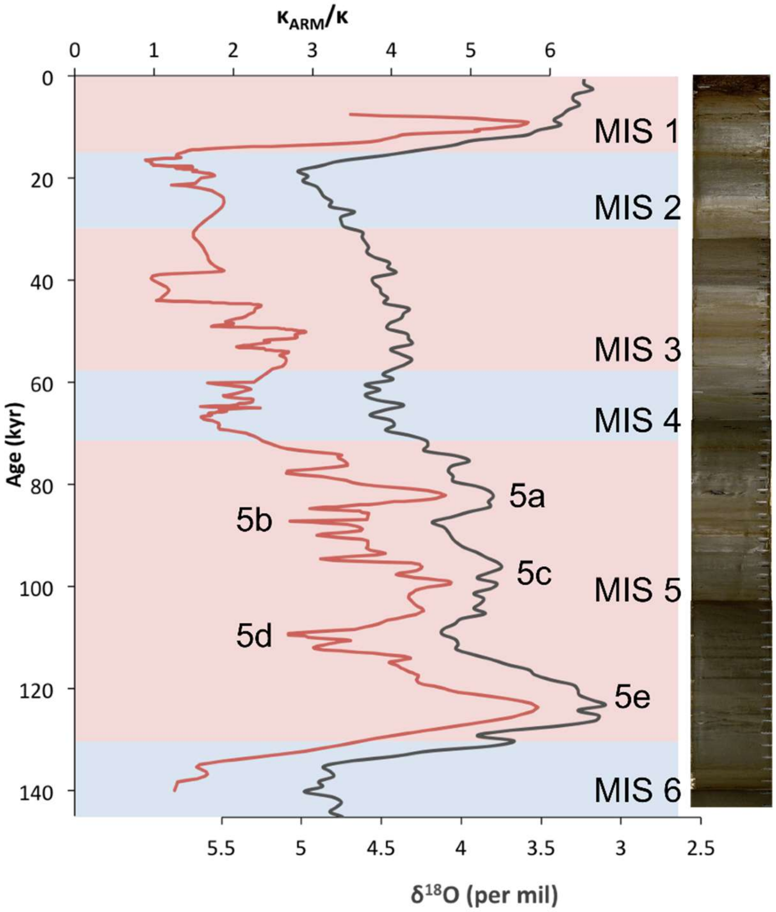

Figure 22. Realignment of the κ_{ARM}/κ magnetic grain size proxy of JPC22 (red curve; Xuan et al., 2012) and LR04 $\delta^{18}O$ benthic stack (black curve; Lisiecki & Raymo, 2005). MIS labeled and glacial (blue) and interglacial (red) conditions indicated. Peaks in κ_{ARM}/κ (warm periods) correspond to troughs in oxygen-isotopes (warm periods; peaks in above plot, note reversed x-axis).

4.3 Stratigraphy of JPC22 (Fram Strait)

The resulting age model and the calculated overall MIS sedimentation rates are higher for cool periods (Stages 2 and 4) and lower for preceding and subsequent warm periods (Stages 1, 3, and 5) (**Figure 22**; **Table 6**). Within each stage, there is variability in sediment accumulation rates. Both short-term pulses of rapid sedimentation and periods of highly reduced sedimentation are identified.

This JPC22 age model yields an overall average sedimentation rate of 4.5 cm/kyr for the past 140 kyr (**Figure 23**; **Table 6**). Because previous work has revealed intervals of rapid ice sheet calving in the Arctic (Darby et al., 2002, 2006; Darby and Zimmerman, 2008), the sedimentation rate variation throughout JPC22 suggests that this age model is largely consistent with this history of rapid sedimentation events for the Arctic region (**Figure 23**; **Table 6**). The Weichselian Glacial periods experienced increased sedimentation relative to their interglacial counterparts (Eemian) (4.8 cm/kyr vs. 2.1 cm/kyr; **Table 6**), and cold MIS Stages are associated with increased sedimentation rates relative to warm Stages. The timings of major ice calving events, such as Termination 1 in late Stage 2, are associated with increased sediment accumulation rates in JPC22 (12.8 cm/kyr).

Table 6. Linear sedimentation rates for JPC22 Marine Isotope Stages, r^2 in parentheses. Rates for the Wisconsin/Sangamonian Stages and Weichselian/Eemian Periods are also calculated. The rates for MIS 5 substages are based on peak-to-peak measurements (e.g. 5e maximum (123 ka) to 5d minimum (109 ka)), the resulting rates are likely inflated or deflated but do show the inter-Stage variability during MIS 5.

Stage Designation	Range (age)	Sedimentation Rate (cm/kyr)
Full Record	overall (0 - 140 ka)	4.5 (0.98)
MIS 1	overall (0 - 14 ka)	4.1 (0.96)
MIS 2	overall (14 - 29 ka)	7.5 (0.78)
	late (14 - 21 ka)	12.9 (0.98)
	early (21 - 29 ka)	1.5 (0.97)
MIS 3	overall (29 - 57 ka)	5.9 (0.92)
	late (29 - 44 ka)	2.1 (0.94)
	late middle (44 - 45 ka)	21.8 (0.98)
	early middle (45 - 48 ka)	4.1 (0.99)
	early (48 - 57 ka)	8.8 (0.98)
MIS 4	overall (57 - 71 ka)	8.6 (0.95)
	late (57 - 62 ka)	3.5 (0.88)
	middle (62 - 67 ka)	12.0 (0.99)
	early (67 - 71 ka)	3.2 (0.99)
MIS 5	overall (71 - 130 ka)	3.7 (0.99)
	5a (peak: 82 ka; 80 - 84 ka)	5.2 (0.97)
	5b (peak: 82; 84 - 90 ka)	5.7 (0.96)
	5c (peak: 87ka; 90 - 102 ka)	3.6 (0.99)
	5d (peak: 109 ka; 102 - 116 ka)	3.6 (0.98)
	5e (peak: 123 ka; 116 - 130 ka)	1.9 (0.93)
Other Stages & Periods	Wisconsin Stage (11 - 85 ka)	4.9 (0.97)
	Sangamonian Stage (75 - 125 ka)	3.8 (0.99)
	Weichselian Perid (11.7 - 115 ka)	4.8 (0.98)
	Eemian Period (115 - 130 ka)	2.1 (0.93)

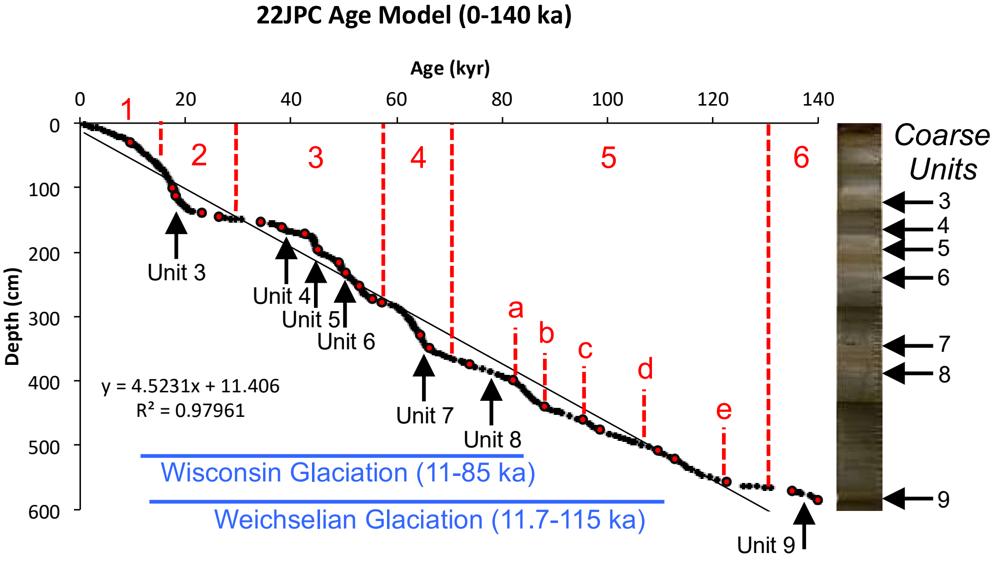

Figure 23. JPC22 age model. Age-depth tie-points are denoted by the red dots. Note that the sedimentation rates vary in accordance with what is expected for the climatic stage and is highly variable during the Wisconsin/Weichselian Glacial phase. Marine Isotope Stages are labeled in red. The JPC22 core photo is aligned with the age model to exhibit color variation associated with climatic changes, darker units correspond with cooler temperatures and lighter colors correspond to warmer periods. The coarse sand units identified in this study are labeled and noted with black arrows.

4.4 Results

4.4.1 Unique Textural, Provenance, and Mineralogy Trends

The textural data from the Fram Strait core JPC22 shows general trends expected for the age model developed on the κ_{ARM}/κ grain size proxy. Using the MIS designations defined by the JPC22 age model, glacial, interglacial, and transitional variations in 45-63 µm, 63-250 µm, and >250 µm contributions are evident. Both the glacial and interglacial periods are texturally similar and exhibit the highest mean contribution from > 250 µm (4.6 % and 4.1 %, respectively), followed by 63-250 µm (3.7 % and 3.0 %), and 45-63 µm (2.0 % and 2.2 %). The periods centered on the MIS transitions exhibit higher average concentrations of 63-250 µm (5.3 %) followed by >250 µm (4.3 %) and then 45-63 µm (2.7 %). There is significant overlap in texture between periods of glaciation and transitions, thus texture is not always useful in interpretations of periods. However, substantial excursions in texture can be used to identify important events that can help constrain the sedimentary history of the Arctic Ocean.

Two distinct coarse-grained unit-types are recognized in JPC22. These two unit-types consist of fine-sand (FS) and coarse-sand (CS) units, and generally correspond to periods of rapid sedimentation. Figure 23 shows the JPC22 age model labeled with identified coarse and fine sand intervals. The occurrences of these units are, in most cases related to glacial activity and the MIS transitions. Fe-oxide provenance for these FS and CS units provides some insight into the glacial dynamics and changes occurring in the Arctic during these times. Additionally, these coarse events have the greatest potential for being used to correlate the JPC22 age model to central Arctic Ocean sediment records.

Throughout the studied section of JPC22, the range of Fe-oxide grains per sample that matched to unique sources from the circum-Arctic ranged from 15 to 158, while the number of analyzed grains per sample ranged from 21 to 194. The average percentage of Fe-oxides grains matched to a specific source is 80.9 %, with a range of 55.9-96.0 %. Of these matched grains, 73.4 % on average (ranging from 58.7-84.4 %) match to regions once covered by major ice sheets.

In general, the local Svalbard contribution to JPC22 is low considering the proximity to JPC22, averaging 9.1 % of all matched grains (σ = 3.0 %; range – 4.8-19.8 %). Periods of exceptional Svalbard input occur at 13.9, 11.7, and 10.9 ka, at which time grains matching to Svalbard account for 19.8, 19.3 and 19.0 % of all matched grains. Like the timings of these increased Svalbard inputs, it was previously found that the BKIS deglaciation occurred as a two-step process dated to 10.5 and ~12.7 ka (Polyak et al 1995). These dates roughly coincident with the Younger Dryas Cooling Event (11.7-12.9 kyr) and the timings of two Svalbard pulses found in JPC22 (**Figures 24** and **25**). No other periods experience higher concentrations of Fe-oxides from Svalbard in the last 140 ka.

Sampling from Greenland Ice Sheet sources are limited to the northern Greenland region in this study. Fe-oxides from this region have a low occurrence in JPC22, with an average contribution of only 3.1 % grain matches (σ = 4.9 %; range – 1.1-15.0 %). Due to the prominent southerly current in the western Fram Strait, Greenland sediments are likely restricted locally in the western Fram Strait.

Overall the BKIS and IIS contribute more sediment to the Fram Strait than the LIS sources, averaging 36.2, 24.3, and 13.0 % (σ: 3.8, 4.1, and 3.8 %,) of all matched grains, respectively. This trend is expected, due to the proximity and direct input from the BKIS and IIS to the Yermak Plateau (**Figure 20**). The LIS contribution is lower due to the longer transport distances; material must first pass through the BG, become incorporated into the TPD, and then transported to the Fram Strait. During most coarse events, the contribution from the BKIS and IIS is high which would in turn result in lower LIS contributions through dilution. Therefore, instances where the LIS input to JPC22 exceeds 16.8 % (one standard deviation above the mean LIS grain match percent) are considered a major input.

Throughout the identified coarse and fine sand units, variations in the primary source provenance are evident. The primary sources for the CS and FS textural units identified in this study are found in Table 4-3. The 9 CS and FS units identified loosely fit into four categories, (1) strongly related to IIS dynamics, (2) strongly related to BKIS dynamics, (3) related to roughly equal contributions from all major ice sheet source regions, or (4) restricted to major sea-ice production zones. In addition to these primary sources, a significant input from other various sources that precede and or follow certain units are shown to have impacts on the mineral variations through these units and provide some indication of the timing of events in the context of Arctic glacial history.

4.4.2 Fine Sand (FS) and Coarse Sand (CS) Units

A total of nine coarse and or fine sand (CS and FS) units are identified in JPC22 in the past 140 ka. Of the identified CS and FS units, all but two are associated with elevated sediment accumulation rates. Three of the nine CS and FS units are comprised of multiple fine and coarse sand intervals. Many of these units are closely related to Greenland Stadials and/or Interstadials (GS/GI) identified in Greenland ice core records, the latter being analogous to Dansgaard-Oscheger (DO) events.

Nine FS intervals identified constitute all or in part of five of these units and are bound with and interrupted by pulses of fine sand that exceed two standard deviations above the mean 63-250 µm fractions. These FS units are typically associated with strong increases in the coarse silt fraction (45-63 µm) as well (**Table 7**). Based on the textural distribution of these FS units, it is inferred that they are of a mixed-type transport with both large-scale iceberg transport and significant sea-ice contributions. However, icebergs can transport fine sands and muds, so a sea-ice contribution is not necessarily guaranteed by the presence of fine sand.

A total of seven CS intervals are identified in JPC22 which comprise four individual CS units and another three units associated with varied textures. Three of the CS intervals are identified with compositions exceeding two standard deviations above the mean >250 µm fraction. An additional four CS units are selected that exceed one standard deviation above the mean >250 µm fraction and have timings coincident with well-documented events. Like the identification of the FS units, the CS units are generally bound by and injected with pulses of extremely coarse-grained sediment. Based on the strongly coarse (>250 µm) signals of these CS units, it is inferred that iceberg transport processes dominate during these periods.

Figure 4.5 compares these CS and FS units to the NGRIP oxygen-isotope curve (Lisiecki and Raymo, 2005). The first two units are identified as single CS peaks. For the period of 11.0-12.8 ka, a sediment accumulation rate of 6.7 cm/kyr is calculated. During the CS 1 (11 ka) unit, LIS are slightly elevated, but not significantly, and a substantial flux of BKIS material is recorded at 10.9 ka. The primary source areas are 9, 33, and 34 (Mackenzie River, Svalbard, and southwestern Barents Sea). The latter likely indicates a northward transport of material from the Norwegian Sea. Bulk mineralogy shows increasing expansive clays and elevated Smec/Kaol ratio and slightly reduced plagioclase and tridymite, all of which implies the increasing importance of BKIS sources (less importance of Laptev and East Siberian Seas) over the North American sources. This 11-ka unit of fine sand is probably related to the 11.4 ka oxygen-isotope excursion identified in Greenland ice records (**Figure 24**; Rasmussen et al., 2014).

Coarse sand unit 2 (12.5 ka) exhibits significant BKIS contributions and is coincident with the Younger Dryas event (**Figure 24**; GS-1 at 12.9 ka; Rasmussen et al., 2006; Steffensen et al., 2008). This BKIS contribution mainly consists of source area 30 (Franz-Victoria Trough). In addition, there is an enhanced source area 9 signal during this time (Mackenzie River/LIS). Appreciable ice sheet fluxes are registered for the period just following this coarse event. Following the 12.5 coarse event, BKIS (12.3 ka), IIS (12.2 ka), and LIS (12.0 ka) sediments enter the Fram Strait (**Figure 25**). Overall, the mineralogy shows decreasing plagioclase for the period centered on 12.5 ka (12.9-12.2 ka). This trend is indicative of a reduction of Eurasian sources during this period. The following period, 12.2-11.4 ka exhibits increases in plagioclase and tridymite consistent with the increasing BKIS and Laptev and East Siberian Sea sources over this period.

The first grouped event encompasses the period between 19.3-14.3 ka and consists of five FS units (3a & 3c-f) and one CS unit (3b) (**Table 7**). A calculated linear sedimentation rate of 12.8 cm/kyr is associated with this unit. Based on the timing and the high sediment accumulation rate, this unit corresponds to MIS 2/1 and thus represents Termination I. The individual CS event at 17.4 ka corresponds to GS-2.1a (**Figure 24**; Rasmussen et al., 2014). This time interval is coincident with the sharp rise in global atmospheric CO2 (Monnin et al., 2001; Pendleton et al., 2015), and corresponds with the early portion of Termination I. Fe-oxide provenance indicates increased contributions from the major sea-ice production regions of the East Siberian and Laptev Seas which conforms to the dominant fine sand texture of this unit. In general, the LIS contribution is low throughout, only insignificantly peaking at 15.6 ka (> 13 %). This increase in LIS at 15.6 ka is contemporaneous with an increase in BKIS sediment flux. Prior to the 15.6 ka portion at 16.9 and 16.4 ka, there is an increase in IIS sourced material. The unit is capped by increased Laptev Sea sediment sources. Beyond this unit 3, LIS contributions steadily increase until significant concentrations are registered at 12 ka (CS 2?). Bulk mineralogy of CS 3 is consistent with the identified source provenance changes, with high feldspar concentration in the later portion as well as steadily increasing dolomite concentrations.

Unit 4 occurs between 38-39 ka, coincident with GS-9 (39.9 ka) and GI-8c (38.2 ka) found in Greenland oxygen-isotope records (**Figure 24**; Andersen et al., 2006; Blockley et al., 2012). This interval is associated with a sediment accumulation rate of 6 cm/kyr and is represented by excursions of >250 µm material (4b; 38.9 ka) followed by a sharp increase in the 63-250 µm fraction (4a; 38.1 ka). This unit transitions from an extremely coarse (38.9 ka) to a fine sand (38.1 ka) texture, and provenance is restricted to materials sourced to the East Siberian Sea. At 38.9 ka, no combined ice sheet source appears to be contributing significantly to JPC22, but source areas 5 and 7 are significantly elevated. These sources are located on Bathurst Island which is near the boundary of the LIS and IIS, thus a contribution from this region might be responsible for the extremely coarse portion of unit 4. During the latter portion of unit 4 (38.1 ka), the ESS is the primary source which combined with the finer sediment texture implies a sea-ice origin. Nothing in the bulk mineral data implies a particularly strong North American source for this unit. The expansive clays, plagioclase, and tridymite are all elevated, while dolomite is absent (**Figure 26**).

Unit CS 5 (44.7 ka) exhibits the highest concentration of >250 μm IRD (14.8 % of bulk sediment volume) and the highest calculated rate of JPC22 sediment accumulation (~25 cm/kyr) for the last 140 ka, indicating a substantial glacial ice-rafting event. The timing of 44.7 ka corresponds exactly to GI-12b (**Figure 24**; Rasmussen et al., 2014). The provenance data for this interval suggests that a large influx of BKIS material at 44.9 ka followed by a large influx of Laptev Sea sediment at 44.7 ka. Finally, by 44.3 ka, a large influx of LIS material is deposited at the JPC22 core site. The mineralogy for this unit shows elevated expansive clays, plagioclase, tridymite, and zeolite at 44.9 ka that are all indicative of Eurasian sources. Later in this unit there is a shift to increased dolomite with a reduction in zeolite and tridymite.

Table 7. Fine-sand (FS) and Coarse-sand (CS) units identified in JPC22. Probable transport process is presented as either iceberg dominant (Iceberg) or a mixture of Iceberg transport and sea-ice transport (Mix). For units occurring across a range of dates, both the mean and range is given. For units only identified in a single interval, their respective values are listed. Possible associations with known events are also given.

				Textural Properties											**Events**	
				Mean Grain Size (µm)		**> 250 µm (%)**		**63-250 µm (%)**		**45-63 µm (%)**		**< 45 µm (%)**		**Probable Transport Process**	**Associated Events**	**Greenland Interstadial/ D-O Event**
Unit	**CS/FS**	**Age (kyr)**	**Depth (cm)**	**Interval Mean (µm)**	**Range (µm)**	**Interval Mean (%)**	**Range (%)**	**Interval Mean (%)**	**Range (%)**	**Interval Mean (%)**	**Range (%)**	**Interval Mean (%)**	**Range (%)**			**ID (Age; Rasmussen et al., 2014)**
1	**CS**	**11***	38.5	86.8		9.1		1.1		1.4		88.4		Iceberg	Bond event 8[a]; IRD 1[c]	**Younger Dryas-Preboreal Transition** (11.7 ka)
2	**CS**	**12.5***	47.5	87.5		8.1		2.0		1.7		88.1		Iceberg	H0; IRD 1[c]	
3a	**FS**	**15.2 - 14.3**	68.5 - 60.5	55.2	28.2 - 86.2	4.0	0.8 - 7.4	11.1	5.7 - 12.5	4.1	2.7 - 4.8	80.9	71.4 - 85.0	Mix	IRD 2[c]	**GI-1** (14.7 ka)
3b	**CS**	**15.9 - 15.3**	75.5 - 69.5	71.7	42.5 - 104.6	6.6	3.0 - 10.2	3.8	0.4 - 8.4	2.2	0.5 - 4.3	87.4	84.1 - 89.9	Iceberg	IRD 2[c]; late MIS 2/1 deglaical	
3c	**FS**	**17.1 - 16.4**	89.5 - 80.5	49.0	16.2 - 86.4	3.5	0 - 7.5	6.3	3.4 - 8.9	4.5	2.6 - 5.6	85.7	80.0 - 91.2	Mix	IRD 3[c]	
3d	**FS**	**17.5 - 17.4**	95.5 - 94.5	68.3	34.2 - 102.4	4.9	2.1 - 7.7	11.0	10.5 - 11.5	4.5	4.3 - 4.7	79.6	77.4 - 81.7	Mix	IRD 3[c]	
3e	**FS**	**17.9**	105.5	59.4		6.3		10.4		2.4		80.9		Mix	early MIS 2/1 deglacial	
3f	**FS**	**19.3**	125.5	63.1		6.5		10.5		2.8		80.2		Mix	IRD 3[c]	
4a	**FS**	**38.1**	160.5	54.8		4.1		12.7		3.6		79.6		Mix	H4 (38 ka)[b]	**GI-8** (38.2 ka)
4b	**CS**	**38.9**	165.5	141.5		14.0		13.8		3.8		68.5		Iceberg	IRD 7[c]	
5	**CS**	**44.7**	190.5	110.8		14.8		16.7		2.8		65.7		Iceberg	H5 (44 ka)[b]	**GI-12b** (44.68 ka)
6	**CS**	**53.7 - 53.1***	261.5 - 254.5	72.7	36.4 - 96.3	6.9	2.9 - 9.3	2.1	0.6 - 3.9	1.5	0.6 - 2.5	89.5	88.4 - 91.2	Iceberg	late MIS 4/3 transition	**GI-14 a-e** (51.5 - 54.2 ka)
7a	**CS**	**62.0 - 61.5***	299.5 - 294.5	78.9	49.5 - 91.1	7.4	3.6 - 8.7	3.2	1.0 - 3.4	1.7	1.6 - 8.3	87.8	84.6 - 89.5	Iceberg	early MIS 4/3 transition	**GI-18** (64.1 ka)
7b	**FS**	**64.2 - 64.1**	325.5 - 324.5	73.5	66.2 - 80.8	6.8	6.7 - 6.8	13.7	12.0 - 15.5	3.7	3.7 - 3.8	75.8	74.1 - 77.5	Mix	Norwegian-Greenland Sea Excursion[d]	
8	**FS**	**79.5 - 68.3**	390.5 - 358.5	44.4	8.8 - 91.0	3.1	0 - 7.5	5.9	1.1 - 14.3	4.5	1.3 - 7.2	86.5	74.2 - 96.0	Mix	MIS 5/4 transition	
9	**FS**	**139.1 - 130.4**	580.5 - 565.5	58.9	50.4 - 66.3	4.7	4.0 - 5.6	11.0	5.5 - 20.1	3.0	2.1 - 4.2	81.2	70.9 - 87.1	Mix	Late MIS 6 deglacial	
22JPC Overall (0-600 cm; 0-140 ka)		**Mean**		50.8		4.3		3.8		2.2		89.7				
		Std. Dev.		24.2		2.6		3.3		1.3		5.1				
		Min.		3.2		0		0		0.1		65.7				
		Max.		141.5		14.8		20.1		7.6		99.9				

*Denotes coarse intervals associated with fraction concentrations exceeding 1 standard deviation above the fraction mean.

[a](Bond et al., 1997); [b](Hemming, 2004); [c](Darby & Zimmerman, 2008); [d](Nowaczyk & Frederichs, 1999)

CS - Coarse Grained Event

FS - Fine Grained Event

Units are identified and defined in this section.

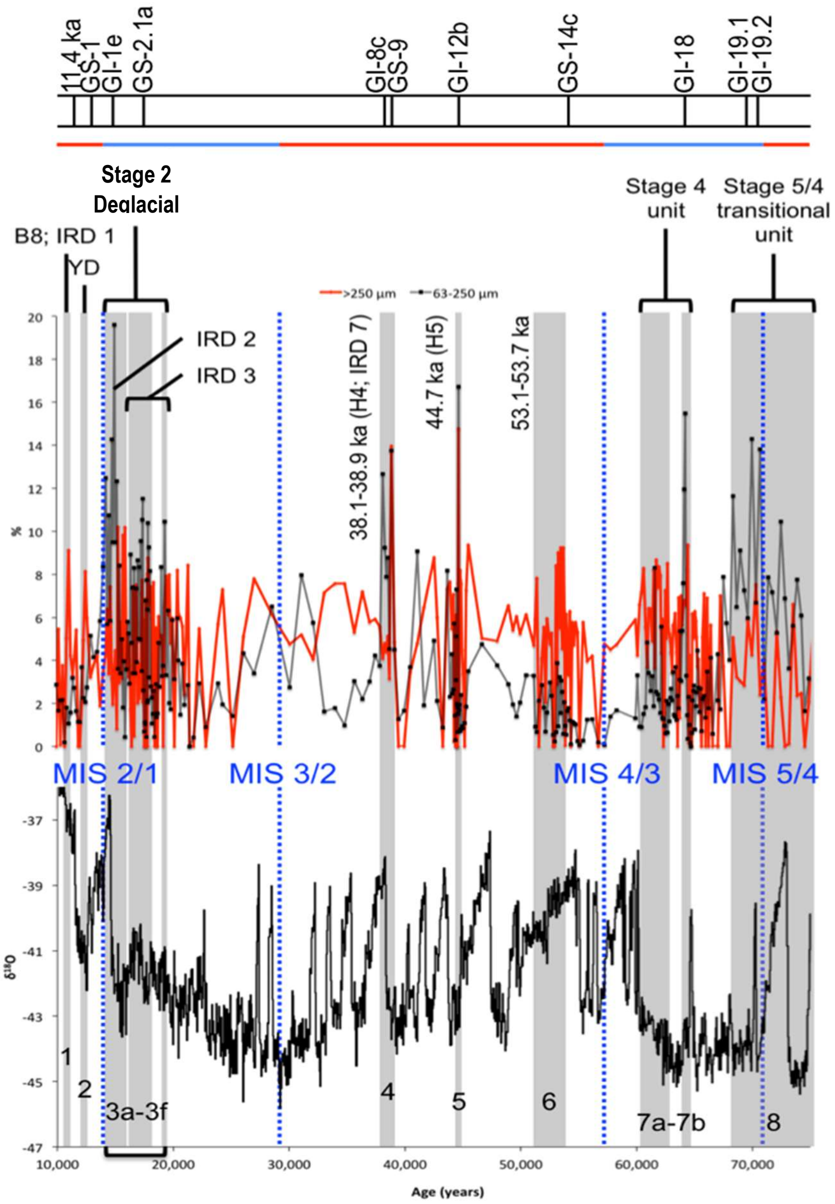

Figure 24. Plots of the NGRIP oxygen-isotope record and the >250 µm (red line) and 63-250 µm (grey line) concentrations for the period of 10-75 ka. Grey bars represent the coarse events identified in this study and are labeled accordingly (1-8; Table 2.3). Ages and or associated events are noted for each event. Dates for Heinrich events (H4 (38 ka) & H5 (45 ka)) are from Hemming (2004). The IRD 1-3 & 7 coarse units are identified in Darby & Zimmerman (2008). Bond event 8 (B8) is from Bond et al. (1997) and Allen (2003). Note: half of the 68.3-79.5 ka event and the 130.4-139.1 ka events fall outside of the plotted area. The latter corresponds to the late MIS 6 deglaciation.

Prior to CS 5, CS 6 occurs in the early portion of MIS 3 and covers the period of 53.1-53.7 ka. This unit is comprised of four > 250 µm coarse peaks and a sedimentation rate of 11.4 cm/kyr. The first three, at 53.7, 53.4 and 54.3 are all substantial with >9% of the bulk sediment volume represented by the >250 µm fraction. The fourth peak in this interval, at 53.1 ka, also exhibits increased >250 µm composition (8.4%). These intervals correspond with the start of GS-14c and d (**Figure 24**; ~54 ka; Rasmussen et al., 2014). Like CS 5, CS 6 is associated with a strong BKIS signal (53.2 ka) that precedes a North American signal (IIS inputs at 52.6 ka). In CS 6, the largest source area contribution is from SA's 36 and 37, corresponding to Novaya Zemlaya and Vilkitski Strait (**Figure 20**). Consistent with the late unit increase in North American sources, the mineralogy trends for CS 6 shows a decrease in plagioclase and increasing dolomite and pyrophyllite. Additionally, there is a brief, but sharp increase in expansive clays at 53.6 ka that probably relates to a sudden reduction in kaolinite delivery to Fram Strait as constrained by a decreasing Smec/Kaol ratio.

Table 8. Fe-oxide source provenance based on grain match percentage for coarse sand (CS) and fine sand (FS) units identified through Malvern analysis. Note: the age ranges and the FS/CS expressions are listed as youngest to oldest.

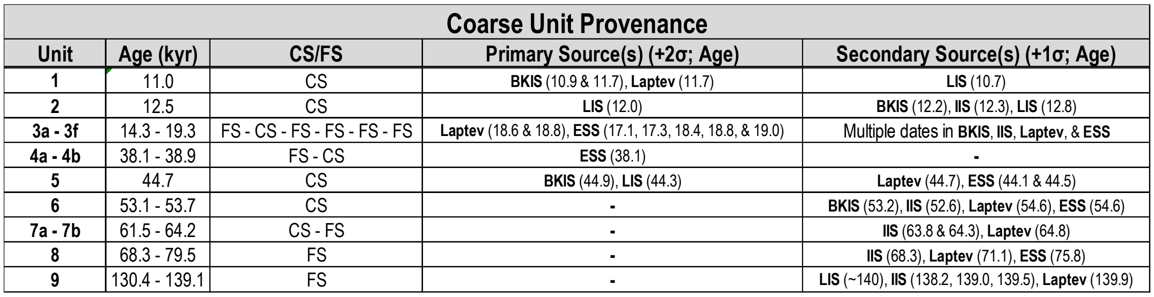

Coarse Unit Provenance				
Unit	**Age (kyr)**	**CS/FS**	**Primary Source(s) (+2σ; Age)**	**Secondary Source(s) (+1σ; Age)**
1	11.0	CS	**BKIS** (10.9 & 11.7), **Laptev** (11.7)	**LIS** (10.7)
2	12.5	CS	**LIS** (12.0)	**BKIS** (12.2), **IIS** (12.3), **LIS** (12.8)
3a - 3f	14.3 - 19.3	FS - CS - FS - FS - FS - FS	**Laptev** (18.6 & 18.8), **ESS** (17.1, 17.3, 18.4, 18.8, & 19.0)	Multiple dates in **BKIS**, **IIS**, **Laptev**, & **ESS**
4a - 4b	38.1 - 38.9	FS - CS	**ESS** (38.1)	**-**
5	44.7	CS	**BKIS** (44.9), **LIS** (44.3)	**Laptev** (44.7), **ESS** (44.1 & 44.5)
6	53.1 - 53.7	CS	**-**	**BKIS** (53.2), **IIS** (52.6), **Laptev** (54.6), **ESS** (54.6)
7a - 7b	61.5 - 64.2	CS - FS	**-**	**IIS** (63.8 & 64.3), **Laptev** (64.8)
8	68.3 - 79.5	FS	**-**	**IIS** (68.3), **Laptev** (71.1), **ESS** (75.8)
9	130.4 - 139.1	FS	**-**	**LIS** (~140), **IIS** (138.2, 139.0, 139.5), **Laptev** (139.9)

*if no primary (+2σ) source is identified, then the secondary source is considered primary

The last grouping of coarse IRD identified, unit 7, occurs between 61.5-64.2 ka has a sedimentation rate of 11.4 cm/kyr and is coincident with the timing of MIS 4. Corresponding to GI-18 (**Figure 24**; 64.1 ka; Rasmussen et al., 2014), this unit is probably related to the ice sheet growth early in

MIS 4. This unit begins with a peak in coarse sand (>1 σ above the mean >250 µm fraction) at 64.4 ka, followed by a sharp increase in fine sand at 64.2 ka (15.5 %). Over the following ~3.5 kyr, there is continuous elevated coarse sands, and a muted fine sand signal. The texture of this unit implies a dominant iceberg transport with weakened sea-ice transport. This unit is preceded by a Laptev Sea signal. The early portion of the unit exhibits an increase in IIS material at ~63.4-63.0 ka. Overall, the bulk mineral signature of this interval is composed of increasing expansive clays, decreasing plagioclase, and a sharp peak in pyrophyllite at 62.6 ka.

Fine sand unit 8 (**Table 7**) occurs over a broad period of >10 kyr (68.3-79.5 ka) and is associated with a low rate of sediment accumulation (2.9 cm/kyr). The early portion of this unit is only associated with coarse peaks that are moderately above the background levels (only few peaks exceeding 1 σ above the mean >250 and 63-250 µm means). Between 72.4-68.3 ka, however, there are four distinct jumps in the fine sand fraction (72.4, 70.6, 69.9, and 68.3 ka) which greatly exceed the background 63-250 µm signal (>2 σ above the 63-250 µm mean). This latter portion of unit 8 is coincident with the start of GS-19.2 (70.4 ka) and GI-19.1 (69.6 ka) (**Figure 24**; Rasmussen et al., 2014). Unit 8 exhibits elevated concentrations of Laptev Sea and East Siberian Sea material, and a pulse of IIS material just beyond the end of the unit (67.5 ka, **Figures 25** and **26**; **Table 8**). These sources coupled with the fine sand texture, implies this unit is derived from sea-ice entrainment. The mineralogy of this unit shows decreasing feldspars and a high dolomite concentration. These trends are consistent with and the result of increasing influence from North American sources.

The last unit, FS 9, stretches across the period of 130.4-139.1 ka (**Table 7**). This timing is coincident with the transition from MIS 6 to MIS 5e and exhibits a very low sediment accumulation rate of 1.9 cm/kyr. This unit is comprised of two peaks in the fine sand fraction at 130.4 ka and 138.2 ka. The latter of which, is the highest 63-250 µm concentration identified in the upper 600 cm of JPC22, with 20% of the sediment consisting of fine sand. The coarse sand fraction throughout this unit is consistently within the range of 4-5.5 %. In FS 9, only the IIS shows significantly increased inputs, and these occur early in the unit (139.5-138.2 ka; **Figure 26**; **Table 8**). This early occurrence makes sense given that this period corresponds to the late Stage 6 glacial transition into the Stage 5e interglacial. Other than the IIS flux, sources 14 and 15, corresponding to the Ob and Yenisei Rivers (i.e. Kara Sea), show appreciable increases in sediment flux to JPC22 during the period of 138.2-135.2 ka (**Figure 26**). Near the end of unit 9, and at the transition from 6 to 5e, there is a sharp increase in western Laptev Sea sediments (SA 17; **Figure 26**). The bulk mineralogy exhibits increasing concentrations of dolomite and expansive clays, and a decrease in Qtz/Fsp (likely due to increasing feldspar) (**Figure 27**). These changes in mineralogy are consistent with the initial increase in IIS sediments and the later increase of Eurasian sources.

4.4.3 Expressions of additional events in the JPC22 marine sediment record

The FS/CS events discussed in the previous section are based on deviations above the mean 63-250 µm and > 250 µm fraction for JPC22. Examining these size fractions in terms of deviations from the individual Stage means reveals many more coarse intervals as well as periods of very fine deposition that are either tied to the GI/GS (Greenland Interstadials and Stadials) or other climate-related chronozones. **Table 9** outlines these deviations and lists potentially corresponding GI/GS events. These events were not used to further refine the JPC22 age model. Other than the similar timings, no other empirical evidence was available to confirm the correlation.

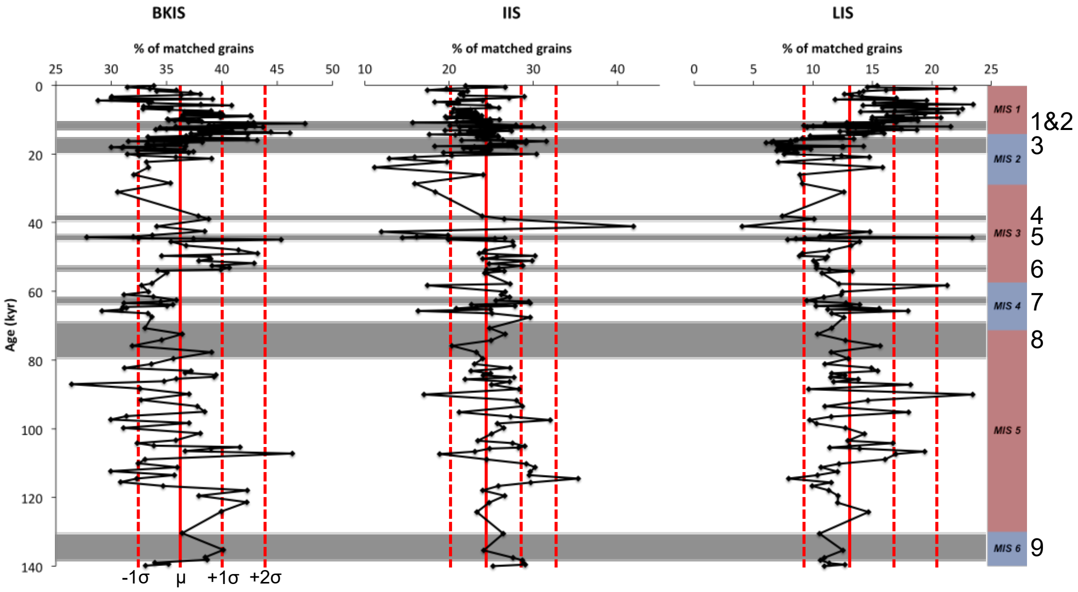

Figure 25. Provenance of ice-sheet sourced Fe-oxide grains in JPC22, given as percent of total matched grains. The relative contribution of these three ice sheet source regions averages 85% throughout core JPC22. The vertical solid red line indicates the mean value in each plot, the vertical dashed red lines indicate the standard deviations about the mean (see labels in BKIS plot).

In terms of the Greenland interstadial/stadial scale, 17 GI/GS events are clearly identified in JPC22 as either coarse or extremely fine intervals. Other GI/GS events are likely missed due to inadequacies in sampling resulting in poor resolution in portions of JPC22. Other distinct changes in sediment deposition are evident based on the textural changes in JPC22. Of note are the appearance of a two-phase Last Glacial Maximum (LGM) prior to Termination I, and the identification of Bond and Heinrich events.

The LGM is identified by extremely fine sediment, where the < 45 μm fraction is > 93.9% of the bulk sediment volume. Two such periods are identified, during 20.2-22.9 ka and 17.6-17.8 ka. The period between these two LGM units (17.8-19.7 ka) is associated primarily with Laptev Sea sourced material throughout and between 18.0-18.5 ka strong inputs from ESS. Conversely, the Stage 2 deglacial is identified as strongly coarse intervals14.0-17.5 ka. The source provenance for the deglacial phases indicates pulses of strong IIS material is followed by BKIS sourced material, while LIS material gradually increases throughout the period.

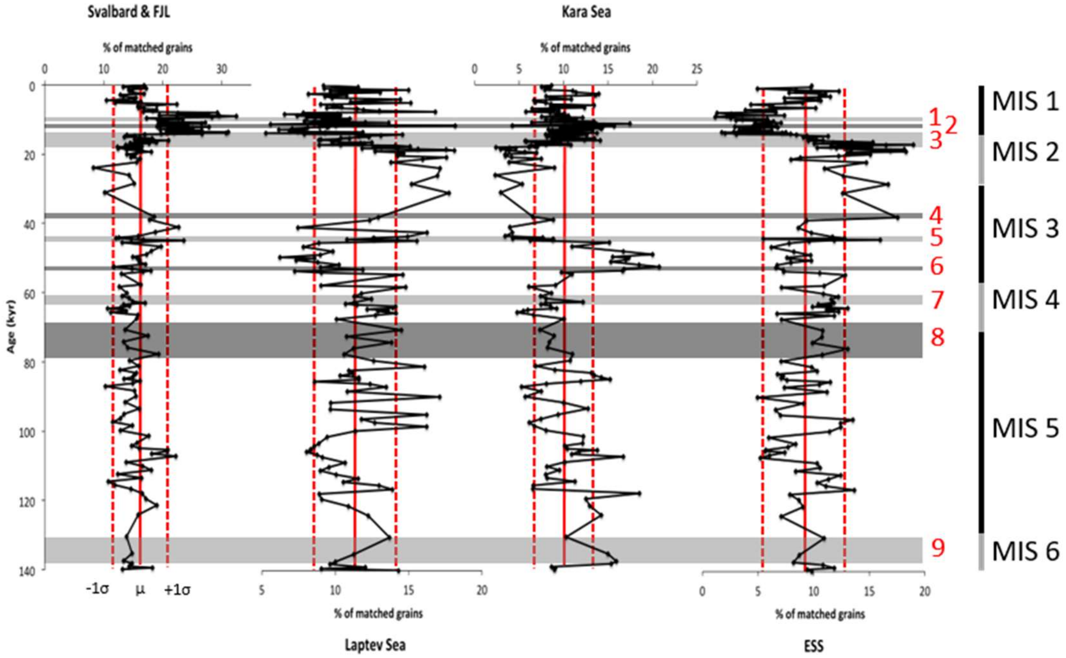

Figure 26. Provenance of Fe-oxide grains in JPC22. Both the Svalbard & Franz Josef Land (FJL), Laptev Sea, and Kara Sea sources are included in the BKIS region but are shown individually to represent their relative contribution. The East Siberian Sea (ESS) source is a major sea-ice production zone during warm phases and is shown so that major sea-ice export events can be identified, the Laptev Sea region is also an important sea-ice production zone during warm phases.

Table 9. List of major textural events in JPC22 focusing on those that correspond to major climate driven events. Textural excursions are based on deviations from the MIS mean for the >250, 63-250, and <45 µm fractions. Bond events (B), Heinrich events (H), and Greenland Interstadials and Stadials (GI/GS) are labeled accordingly. Additional textural events not tied to named events are also listed if their timing is indicative of large-scale events (for instance the Stage 2 deglacial phase). This list is not exhaustive, as there are other intervals where significant textural deviations occur but are not relative to the Greenland oxygen-isotope time scale. Red text indicates values that exceed 2 standard deviations above the respective means, otherwise the values exceed 1 standard deviation above the mean.

Table 9. Major Textural Events in JPC22

MIS	Age (ka)	Depth (cmbsf)	> 250 µm (%)	63 - 250 µm (%)	45 - 63 µm (%)	< 45 µm (%)	Mean Grain Size (µm)	Possible GI/GS	Notes
Stage 1	8.9	25.5	6.2	--	--	--	66.3	8.2 ka event? **(B5)**	--
	9.5	29.5	5.8	--	--	--	65.7	9.3 ka event? **(B6)**	--
	11	38.5	9.1	--	--	--	86.8	11.4 ka event? **(B8)**	--
	12.5	47.5	8.1	--	--	--	87.5	--	--
	12.6	48.5	6	--	--		69.9	Younger Dryas, GS-1; **H0**	--
	12.9	50.5	--	5.2	3.8	--	--	--	--
	13.2	52.5	--	4.2	--	--	--	GI-1a (13.1 ka)	--
	13.5	54.5	--	4.4	--	--	--	GI-1b (13.3 ka)	--
	13.8	56.5	--	5.8	--	--	--	GI-1c1 (13.6 ka)	--
Stage 2	14	58.5	--	8.4	--	--	--	GI-1c3 (13.9 ka)	--
	14.3	60.5	--	12.5	3.6	--	--	--	**Stage 2 Deglacial Phase**
	14.5	62.5	--	10.7	3.7	--	--	--	
	14.6	63.5	7.4	--	--	--	86.2	--	
	14.8	64.5	--	14.3	4.8	--	--	GI-1e (14.7 ka)	
	14.9	65.5	--	9.5	3.6	--	--	--	
	15	66.5	--	19.6	5.3	--	--	--	
	15.1	67.5	--	9.5	4.7	--	--	--	
	15.2	68.5	--	12.3	5.2	--	--	--	
	15.3	69.5	10.2	--	--	--	104.5	--	
	15.4	70.5	--	8.4	4.3	--	--	--	
	15.7	73.5	9.8	--	--	--	102.3	--	
	15.9	75.5	10.2	--	--	--	--	--	
	16.4	80.5	--	8.9	5.3	--	--	--	
	16.6	82.5	7.5	7.4	5.3	--	--	--	
	16.7	84.5	--	8.3	5.6	--	--	--	
	16.9	86.5	7.5	7.3	5.1	--	--	--	
	17	88.5	--	8.7	5.5	--	--	--	
	17.1	90.5	--	8.3	5.2	--	--	--	
	17.3	92.5	7.1	9.6	4.8	--	--	--	
	17.4	94.5	7.8	10.5	4.3	--	102.4	--	
	17.5	95.5	--	11.5	4.7	--	--	--	
	17.6	97.5	--	--	--	98.6	--	GS-2.1a (17.48 ka)	**LGM? Phase II**
	17.6	98.5	--	--	--	97.7	--		
	17.7	99.5	--	--	--	93.9	--		
	17.8	101.5	--	--	--	98.8	--		
	17.8	103	--	7.7	--	--	--	--	--
	17.8	104.5	8	--	--	--	--	--	--
	17.9	105.5	8.8	10.4	--	--	--	--	--
	18	108	7.2	9.3	--	--	--	--	--
	18	108.5	7.1	--	--	--	--	--	--
	18.1	110.5	7.4	8.2	--	--	--	--	--
	18.4	115.5	7.6	--	--	--	--	--	--
	19	123	--	8.4	--	--	--	--	--
	19.3	124.5	--	10.5	--	--	--	--	--
	19.5	126.5	7.9	--	--	--	--	--	--
	19.7	128.5	8	--	--	--	--	--	--
	20.2	131.5	--	--	--	94.9	--	GS-2.1b (20.9 ka)	**LGM? Phase I**
	20.4	133	8.2	--	--	--	--		
	21	136.5	--	--	--	94.3	--		
	21.4	138	8.4	--	--	--	--	--	
	21.5	138.5	--	--	--	99.9	--	GS-2.1c (22.9 ka)	
	21.8	139.5	--	--	--	98.8	--		
	22.9	141.5	--	--	--	98.3	--		
	27.1	146.5	7.8	--	--	--	88	GI-3 (27.78 ka)	--

Table 9 Continued

MIS	Age (ka)	Depth (cmbsf)	> 250 µm (%)	63 - 250 µm (%)	45 - 63 µm (%)	< 45 µm (%)	Mean Grain Size (µm)	Possible GI/GS	Notes
Stage 3	31.1	150.5	--	8	--	--	--	GI-5.1 (30.84 ka); **H3 (?)**	**High Stadial/Interstadial Variability**
	34	153.5	7.6	--	--	--	82.3	GI-6 (33.74 ka)	
	34.9	154.5	7.6	--	--	--	--	GS-7 (34.74 ka)	
	38.1	160.5	--	12.7	3.6	--	--	--	
	38.3	161.5	--	9.3	4	--	--	--	
	38.4	162.5	--	7.9	--	--	--	GI-8c (38.22 ka); **H4**	
	38.6	163.5	--	8.8	--	--	--	--	
	38.9	165.5	14	13.8	3.8	--	141.5	--	
	42.6	173	8.8	--	--	--	83.6	GI-11 (43.34 ka)	
	44.7	190.5	14.8	16.7	--	--	110.8	GI-12b (44.68 ka); **H5 (?)**	
	44.8	193.5	8.2	--	--	--	86.3		
	45.5	200.5	9.4	--	--	--	--	GI-12c (46.86 ka); **H5 (?)**	
	51.4	242.5	7.8	--	--	--	--	GI-4a-e (51.5 - 54.22 ka)	
	53.1	254.5	8.4	--	--	--	--		
	53.3	256.5	9	--	--	--	--		
	53.4	258.5	9.2	--	--	--	--		
	53.7	261.5	9.3	--	--	--	--		
Stage 4	60.4	287.5	7.2	--	--	--	--	**H6 (?)**	
	60.6	288.5	8.3	--	--	--	--	GI-17.1 a-c (58.78 - 59.08 ka); **H6 (?)**	
	61.5	294.5	8.2	--	--	--	--	GI-17.2 (59.44 ka); **H6 (?)**	
	62.5	304.5	7.3	--	--	--	--	GI-18 (64.10 ka) ?	
	62.7	306.5	8.5	--	--	--	--		
	63.9	321.5	7	--	--	--	--		
	64	323.5	--	7.6	--	--	--		
	64.1	324.5	--	12	3.8	--	--		
	64.2	325.5	--	15.5	3.7	--	--		
	64.4	327.5	8.2	--	--	--	--		
	64.4	328.5	9.4	--	--	--	--		
	70.3	364.5	7.5	6.7	4.6	--	--	GS-19.2 (70.38 ka)	
	70.6	365.5	--	13.8	7.6	--	--		
Stage 5	71.4	367.5	--	7.9	5.8	--	--		**Stage 5a & Stage 5/4 transition**
	71.7	368.5	--	7.2	5.5	--	--		
	72.1	369.5	5.4	--	4.3	--			
	72.4	370.5	--	10.4	7.4	--	--	--	
	73.5	373.5	6.6	--	4.7	--		GS-20 (74.1 ka)	
	73.8	374.5	--	7.8	6.2	--	--	--	
	75.5	379.5	6.3	--	--	--		--	
	75.8	380.5	--	6.3	5.3	--	--	GI-20c (76.44 ka)	
	76.2	381.5	--	--	--		--	--	
	77.7	385.5	--	8.3	6.5	--	--	--	
	78	386.5	6	--	--	--	--	GS-21.1 (77.76 ka)	
	78.4	387.5	7.2	--	--	--	65	--	
	106.5	498.5	5.3	--	--	--	--	GS-24.1 (105.4 ka)	**Stage 5d**
	112.4	520.5	--	7.1	3.8	--	--	GS-24.2 (106.9 ka)	

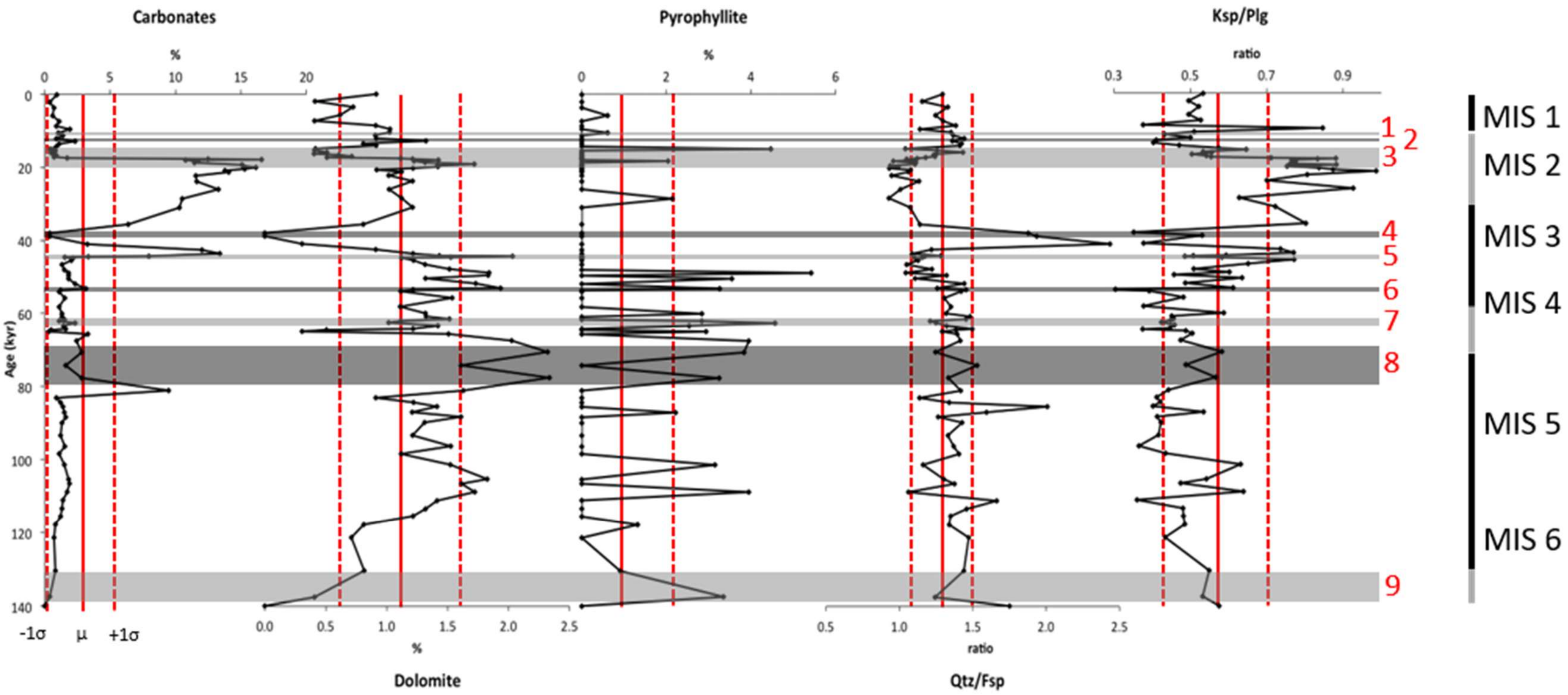

Figure 27. Plots of North American mineral signals in JPC22. Dolomite and pyrophyllite are indicators of North American sources. The plot of carbonate is also shown to differentiate between possible biogenic events. Where carbonate is high and not associated with an increase in dolomite, the source is likely biogenic. Conversely, carbonate peaks associated with dolomite peaks might represent the carbonate signal from Paleozoic Carbonate platforms of the Northern Canada region (these include primarily dolomite but also extensive outcrops of dolomitic limestone).

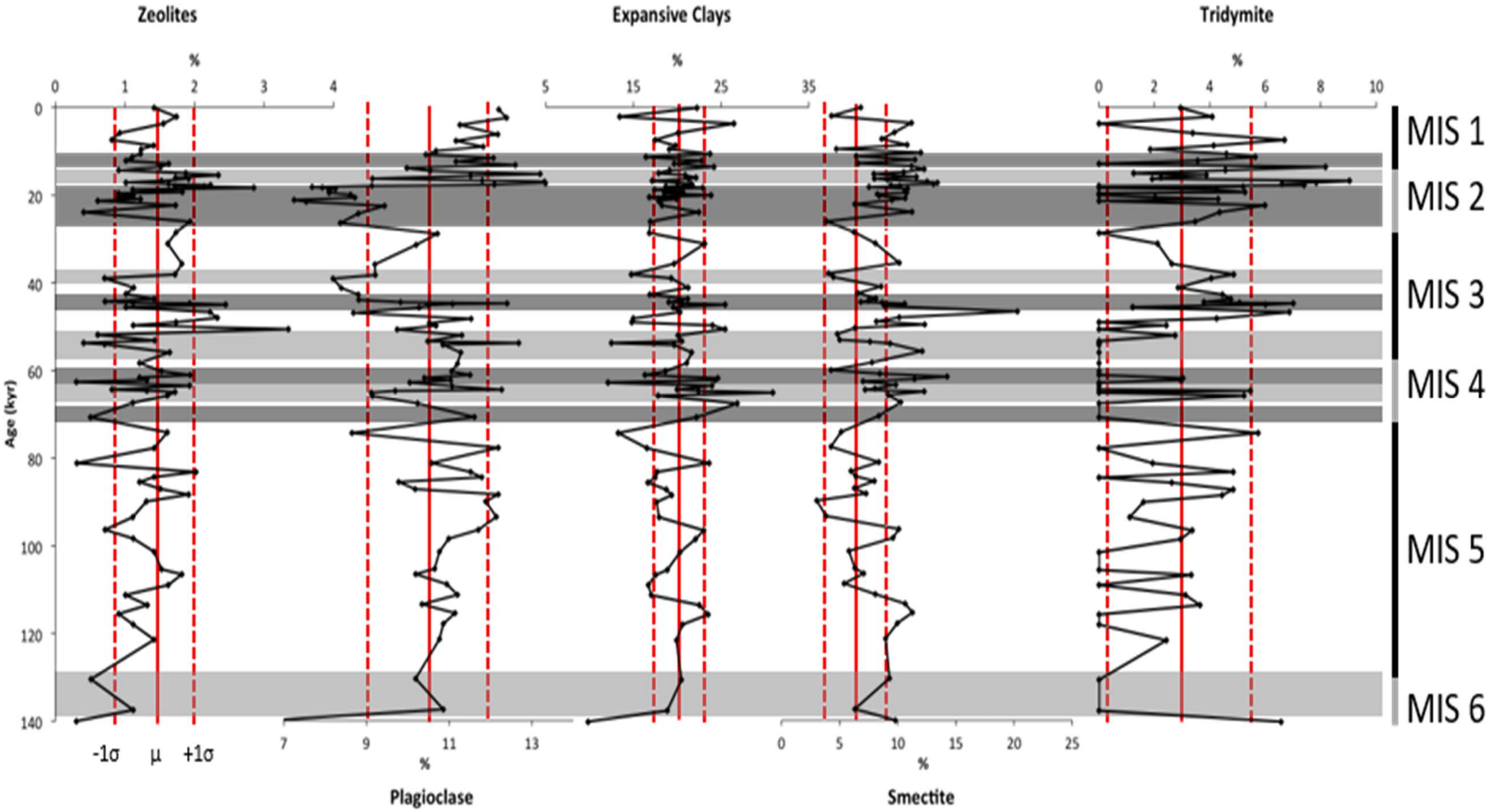

Figure 28. Eurasian source mineral variations for core JPC22. Zeolite, Plagioclase, Smectite, and Tridymite all show the same general trends across all Stages. The expansive clay phase includes smectite and illite/smectite mixed layered clays and shows trends less consistent with the Eurasian-specific smectite signal, implying that mixed layered clays from alternate sources (possibly from North America) affects these trends.

4.5 Discussion

4.5.1 Stratigraphy of Fram Strait Core JPC22

The primary objective of this work was to explore the similarities between a magnetic grain size proxy and the oxygen-isotope stratigraphy with the aim of establishing an age model for the Arctic Ocean sediment record (first described by Xuan and Channell, 2012). The resulting age model developed in this work compares well with both the global $\delta^{18}O$ benthic stack and MIS designations (Liesicki and Raymo, 2005). Additionally, the expected changes in sediment delivery to Fram Strait, as determined with the developed age model are in line with the historical changes.

4.5.2 Accumulation Rates Compared to Nearby Records

The overall sedimentation rate (4.5 cm/kyr) is consistent with, or within the same order of magnitude, as rates found for other sediment records from the Fram Strait region. For instance, Holocene sedimentation rates of 3.5 cm/kyr have been calculated for Norwegian-Greenland Sea sediment records (0-11 ka; Thiede et al., 1986). For comparison, the Holocene section of JPC22 yields an accumulation rate of 3.6 cm/kyr. This comparable accumulation rate indicates that the JPC22 age model is consistent with nearby sedimentary records for at least the Holocene.

In cores from further south, and in much deeper waters, a sediment accumulation rate of 2.4 cm/kyr was determined for the period of 12-71 ka in core PS1320-2 and a rate of 4.1 cm/kyr for the period of 5-28 ka in core PS1294-4, using a chronology based on AMS-14C dates and magnetostratigraphy (Hebbeln & Wefer, 1997). In JPC22 and for similar time ranges, rates of 4.7 cm/kyr and 8.2 cm/kyr are identified, respectively. For JPC22, the rates are roughly twice as high as those presented for cores from further south. A higher rate is expected for JPC22 due to its location closer to both the sea-ice and ice sheet margins (Polar Front). The sea-ice margin has been persistent around the Yermak Plateau region for at least the last 30 kyr (Müller et al., 2009).

4.5.3 Glacial/Interglacial Changes in Sedimentation

Due to increased volumes of sediment ice-rafting, rates of sediment accumulation vary between glacial and interglacial periods, with the cooler periods associated with rates roughly twice that of their warmer counterparts (Hebbeln & Wefer, 1997; 2.4-3.0 cm/kyr (glacial) vs. 1.2-1.3 cm/kyr (interglacial)). This trend of increased accumulation rates during cooler periods, associated with ice sheet growth is also found through the JPC22 age model. Overall, Weichselian Glacial sedimentation rates are more than twice that of the Eemian interglacial (4.8 cm/kyr vs. 2.1 cm/kyr; **Table 6**). Odd numbered (warm) Stages exhibit significantly lower sedimentation rates compared with even-numbered (cold) Stages (**Table 6**). Thus, on a finer temporal scale, the accumulation rate variations between Stages show a similar trend as what is expected with changes in ice sheet volume.

4.5.4 Event Timing to Constrain Age Model Validity

Numerous rapidly-deposited IRD intervals have been identified and dated in Fram Strait and North Atlantic sediment records (Heinrich, 1989; Bond et al., 1999; Spielhagen et al., 2001; Darby et al., 2002; Darby and Zimmerman, 2008). These timing of these IRD units can be used to confirm the accuracy of the oxygen-isotope stratigraphy applied to JPC22, especially those units identified in the well-constrained cores PS1230, PS1231, and PS1894 from Fram Strait (Darby et al., 2002; Darby and Zimmerman, 2008). The accuracy of the age model presented in this chapter is thus tested by comparing the timing of previously identified IRD events in Fram Strait against the timing of coarse- and fine-grained events in JPC22. Additionally, $\delta^{18}O$ excursions in the Greenland ice records corresponding to JPC22 IRD events can be used for further confirmation.

Focusing on the strongest textural signals (i.e. those listed in **Table 6** and red values in **Table 9**) key chronological markers can be determined to confirm the validity of the JPC22 age model. Overall, these coarse-grained events correspond well to the dates of both previously identified IRD events, the timing of Heinrich and Bond events, and excursions in the Greenland $\delta^{18}O$ record (equivalent to Greenland Stadials and Interstadials).

FS/CS units 1, 4, 5 and possibly 2 and 6 show potential as geochronologic markers. CS unit 1, occurring at 11.0 ka, is roughly coincident with the 11.4 ka event identified in the Greenland $\delta^{18}O$ record and/or the occurrence of Bond event 8 (11.1 ka). CS units 2, 4, 5 and 7 correspond well with the timings of Heinrich (H) events 0, 4, 5, and 6, respectively. Like the findings of Darby et al. (2002) these coarse events occur slightly before the recording of their Heinrich event counterparts in North Atlantic sediments. In the broadly-spaced coarse unit 3, many coarse intervals are identified. One or more of these events might correspond to H1 but given the sheer number of coarse events during this interval, this correlation cannot be determined.

In Table 4-5, numerous coarse events are identified that possibly correspond to excursions in the Greenland $\delta^{18}O$ record. Generally, for Stage 2 the occurrence of a GI will be associated with a coarse event and a GS will be associated with a finer texture. Conversely, during Stage 1 (and portions of early Stage 5) the opposite trend is found. This trend does not apply to Stages 3 and 4, as these periods are cool (warm) interstadial (stadial) periods. For example, Stage 3 exhibits multiple GI periods associated with sediment coarsening. Given that the ice volume during Stage 3 was still high relative to the present, interstadial conditions still result in major ice calving events especially in the early portions of the stage.

4.5.5 Last Glacial Maximum

Very fine-grained intervals (identified in **Table 9**) are shown to be contemporaneous with the timing of LGM periods and thus provide a further chronological constraint on the JPC22 age model. All major continental ice sheets essentially reached their maxima at a similar time (Clark et al., 2009). Therefore, this event is an ideal chronozone candidate to confirm the JPC22 age model. An extremely fine-grained unit between 22.9-21.5 ka (possibly extending to 20.2 ka) in JPC22 is identified as the LGM as it is coincident with previously determined age ranges for the global LGM. The dates for the LGM are somewhat wide ranging, but the consensus is that it occurred between 23-19 ka (Hughes et al., 2013).

Interestingly, there is an additional fine-grained unit identified and based on the JPC22 age model is assigned an age of 17.8-17.6 ka. The timing of this event is roughly coincident with that of GS-2.1a

(17.48 ka). This unit could represent a colder than average period with/or increased sea-ice volume during glacial Stage 2. This short unit is inferred to represent a secondary phase of the LGM (LGM phase II). This unit is preceded by extremely coarse sediment probably representing the bulk of the deglacial activity during Termination 1 and is followed by further coarse sedimentation. This feature has not been noted in any literature and is therefore unreliable. The cause of this short event might be related to local ice sheet calving, rather than a northern hemisphere ice sheet event.

4.5.6 Potential Age Model Issues

An offset between the $\delta^{18}O$ and the κ_{ARM}/κ ratio at the MIS 2/1 boundary of >10 cm is likely due to $\delta^{18}O$ depletion from the early deglaciation of the Svalbard region (Knies et al., 1999; Xuan and Channell, 2005). This early deglaciation is substantiated by an increase in Svalbard and Franz Josef Land sourced Fe-oxide grains across the 14.3-14.1 ka interval from 16.9 % to 26.6 % (grain match percent). The latter is more than two standard deviations above the mean grain percent of material from Svalbard and Franz Josef Land reaching JPC22. Similar situations might impart some uncertainty at other glacial-to-interglacial transitions given the proximity of the core site to the Svalbard/Barents Ice Sheet, but overall and beyond this Stage 2/1 offset the record compares remarkably well with the LR04 $\delta^{18}O$ record.

An additional offset might exist near the Stage 6/5e boundary and is exemplified by the presence of planktic foraminifera in high abundances during the latter portion of Stage 6 (unpublished data). This biogenic signal should accompany the Stage 5e interglacial but based on the magnetic grain size proxy for oxygen-isotope stratigraphy this is not the case. Adiabatic winds coming off the ice sheet can act to push ice away from the margin and maintain open water flaw leads that can promote major biogenic production (Wollenberg et al., 2004). The highest abundance of Atlantic foraminifera species in the Arctic occurs in the Fram Strait, especially in regions under the influence of the Western Spitsbergen Current (WSC). Core JPC22, lies in a region under direct influence of the WSC, and therefore, much of the planktonic foraminifera found in JPC22 could be advected into the region from the North Atlantic.

Overall, the variable rates in sedimentation that correspond to warm and cold intervals indicate that the age model for JPC22 is consistent with the paleoenvironmental changes occurring in the Fram Strait region over the past 140 ka. The only point of contention might be the transition from MIS 6 to 5e, due to the foraminiferal enrichment in late Stage 6.

4.5.7 Constraining the Timing of Ice Sheet Activity

In addition to constraining the accuracy of the JPC22 age model, coarse units associated with periods of ice sheet growth and decay can be used to identify potential lead/lag relationships between the major ice sheets. By examining the timing of increased Fe-oxide grain matches from the primary ice sheets prior to, through and following these events, the relative order of ice sheet growth/decay can be inferred. Constraining these timings are critical to the understanding and accurate modeling of Arctic and global paleoclimate evolution.

It has previously been reported that the most common scenario is for IRD from ice sheet sources to occur simultaneously (Darby and Zimmerman, 2008). Furthermore, these authors identified that in the Fram Strait region, one record might show simultaneous ice sheet IRD occurrence while another record might indicate one ice sheet leads the others. The implication of this is that the dynamics of IRD transport and release is quite complex. Of course, it should be noted that this study only focused on the LIS and IIS through the period of 11 to 36 ka, so the relationship with the BKIS was not explored and only MIS 2 was fully studied.

Through the numerous coarse intervals identified in JPC22 and corresponding to major ice sheet growth and decay phases, the general trend is that one ice sheet leads the others. During ice sheet decay phases of MIS 2/1 and 4/3 transitions the increases in IIS Fe-oxides grain matches lead the others. For the stage 2/1 transition, this IIS lead is constrained to the period of 16.6-16.9 ka. For the period of 17.3-17.4 ka, however, the LIS and BKIS occur simultaneously and leads that of the IIS. For late MIS 6/5e, the major deglacial phase is not fully constrained but the Fe-oxide provenance indicates that the LIS might lead the IIS, and the BKIS inputs lag further (LIS [140ka] → IIS [139.5 ka] → BKIS [135.2 ka]). The implications of these leads, is that the deglacial phases are highly complex and that no two deglacial phases are the same, insinuating that it is not the instabilities in a single region that results in full scale deglacial response.

4.5.8 Relationship between JPC22 Coarse Events and Heinrich Events

Based on coincident timings, a relationship between Heinrich events and Fram Strait ice export events identified as coarse IRD signals originating from the LIS have been identified (Darby et al., 2002; Darby and Zimmerman, 2008). Coarse IRD peaks identified in JPC22, and based on oxygen-isotope stratigraphy, chronologically precede the timings of corresponding Heinrich events. Ice export events in Fram Strait have been previously determined to be precursory to the North Atlantic expression of Heinrich events (H0-H3) (Darby et al., 2002). However, since the Heinrich layers in the North Atlantic and the precursory coarse events in Fram Strait are not identified in the same record, the interpreted lead is subject to dating uncertainties (Hemming, 2004).

In JPC22, nearly all Heinrich events are identified (H0-H1 and H3-H6). Only H2 (~24 ka; Hemming, 2008) is not identified in JPC22. The timing of the H1 event in JPC22 is at ~15.9 ka which is more recent than the generally accepted timing of 16.8 ka (Hemming, 2008). However, alternate timings for H1 have been proposed that range from ~14 ka (Vidal et al., 1999) to 15.5 ka based on the average given by Darby et al. (2002). If this latter date for H1 is assumed correct, then for all occurrences of Heinrich event related IRD events in JPC22, the signal in Fram Strait leads that of the North Atlantic by a range of 0.1-1.5 kyr (mean of 0.65 kyr). The implication of the lead-lag relationship is that the Arctic LIS is disintegrating prior to the eastern LIS export through the Labrador Sea (Darby et al., 2002). However, given the potential chronological error in the JPC22 oxygen-isotope stratigraphy and only minor increases in LIS material at these times a similar conclusion cannot be substantiated.

Instead, during coarse IRD events coincident with Heinrich events, there are increases in BKIS material during H0, H1, and H4 and increased IIS inputs for H1, H4, and H6. These increased source signals from specific ice sheet regions implies that there is possibly a connection between the instabilities in the IIS and BKIS to the initiation of Heinrich events. Using an isotope fingerprint of Sr/Nd in the >150 μm fraction it has been suggested, for most Heinrich Events, pulses from the Fennoscandinavian Ice Sheet precedes the dominant LIS IRD in these North Atlantic signals (Grousset et al, 2004). Therefore, instabilities in the Eurasian ice sheet might be the cause for the occurrence of Heinrich Layers. The findings of this work fit well with the concept of a strong BKIS input prior to LIS inputs for Heinrich events. Since the IIS is so small relative to the LIS and BKIS, identifying the IIS signal in the noise of the inputs of the larger ice sheets is somewhat unexpected. It could be that the IIS and LIS export occurs together but the LIS signal at JPC22 is overwhelmed by the IIS signal or the LIS outflow is largely restricted to the Hudson Strait during these events.

4.6 Conclusions

Overall, the age model presented here for core JPC22 from the Fram Strait is consistent with the environmental and glacial history of the Arctic region. As such, reconstructions and interpretations can be made for recognized coarse-grained (IRD) events and the timing of ice sheet dynamics. The accuracy of the JPC22 age model is improved by tuning identified coarse intervals to the ages of corresponding oxygen-isotope excursions from the Greenland ice core records. However, more information would be necessary regarding the timing of these oxygen-isotope shifts and their translations into the marine sediment record.

The timing of changes in provenance associated with Heinrich events show that signals from the BKIS and/or IIS typically lead the LIS signal recorded in Fram Strait sediments. This association suggests that instabilities in the BKIS and/or IIS might initiate the environmental changes that result in Heinrich layers, or at the very least are more susceptible to the processes that initiate these events.

In general, the provenance variations associated with glacial terminations imply that these periods (for at least the late Quaternary) are not necessarily the result of similar processes. Thus, while the initiation of a deglacial phase might be caused by variations in insolation (Milankovitch Cycles), the sequence of events that follow varies considerably. Conversely, ice sheet growth phases might show a persistent lead by BKIS sediments. Therefore, it is suggested that ice growth in the Eurasian region potentially marks the onset of a glacial period. When ice in this region reaches a certain volume, a tipping point is surpassed that pushes the system into full-scale glaciation.

5 EXPLORING THE SEDIMENTARY RECORD OF JPC9, MENDELEEV RIDGE, CENTRAL ARCTIC OCEAN: AN AGE MODEL FRAMEWORK AND CLIMATIC VARIABILITY

5.1 Introduction

The Arctic Ocean is sensitive to global climate change. Through positive feedbacks, small increases in equatorial temperature are amplified in the Arctic region often by an order of magnitude. This climate amplification highlights the importance of this still relatively unexplored Arctic region in terms of our understanding of global climate dynamics and impacts. Central to this understanding are central Arctic sediment records that lack quantitative age control.

Previous investigations have established regional variability in the geology of the coastal areas surrounding the Arctic; using these differences, mineralogical and geochemical variations within sediment records have been used to infer sediment transport pathway changes (Vogt, 1997; Wahsner et al., 1999; Viscosi-Shirley et al., 2003; Darby et al., 2011; Kaparulina et al., 2016). For example, detrital Fe-oxide grain chemistry can be precisely sourced to 41 circum-Arctic sources to determine sediment provenance, transport pathways, and by extension, the relative position of the Transpolar Drift (TPD) and the Beaufort Gyre (BG) through time (Bischof and Darby, 1997; Darby, 2003; Darby et al., 2001, 2009, 2012, 2015; Stein et al., 2010). The ability to identify paleo-transport pathways is a powerful tool, providing insights into environmental change in this polar region. These previous findings are improved, identifying unique mineral signals to infer drift pathway variation and explore how changes in these drift patterns might provide valuable information for correlations between two cores along the prominent TPD and BG drift paths. This improvement is made by first developing an age model for JPC9 using the most reliable data from JPC8. The model is further refined by comparing key horizons formed at the same time at JPC9 and JPC22 by processes that mix BG and TPD sediments.

5.2 Background

The Arctic Ocean can be divided into eastern (Eurasian) and western (Canada) basins, bathymetrically separated by the Lomonosov Ridge (**Figure 1**). The TPD and BG dominate surface circulation and ice transport in the Arctic (Mysak, 2001; Rigor et al., 2002). The TPD is a broad sweeping current, largely restricted to the Eurasian basin that moves from the shelves of the Laptev and Kara Seas across the Arctic Ocean towards and through Fram Strait. The BG is a clockwise gyre largely restricted to the Canada Basin. Due to the semi-basin restriction of these two currents, the sedimentation regimes of eastern and western Arctic are generally considered mutually exclusive. This exclusivity typically hinders the direct correlation of sediment records from the eastern and western Arctic basins. While the BG and eastern portion of the TPD shifts in response to atmospheric conditions, along the central Arctic the TPD remains relatively constant. This consistent TPD stream transports sediment-laden ice from the Chukchi and East Siberian Seas across the Arctic to Fram Strait, roughly along the path from JPC9 to JPC22 (**Figure 1**).

Exchange between the TPD and BG occurs at their confluence in the central Arctic Ocean, and the extent of exchange varies through time depending on atmospheric configuration. Through this mixing a BG signal can imprint into sediment records typically dominated by a TPD sediment signal and vice-versa depending on the strength of mixing. This exchange can thus impart noise into the sediment records of JPC9 and JPC22. Despite this mixing-induced noise, the TPD signal has potential for use as a correlative tool for sediment records over vast distances especially when combined with other variables with similar correlative potential.

Quaternary age models for the western and central Arctic Ocean (Amerasian Basin) are poorly constrained and based on one of several low precision dating techniques, such as biostratigraphy (Cronin, 2013), lithostratigraphy (Clark et al., 1980; Stein et al., 2010), physical properties (Sellén et al., 2010), manganese stratigraphy (Löwemark et al., 2008; 2012; 2014; Wang et al., 2017), cyclostratigraphy (Backman et al., 2008) or other low precision dating techniques (Backman et al., 2004; Polyak et al., 2004). While these various dating techniques are typically only slightly different, the associated errors can often result in missed or misplaced events and erroneous age model shifts. Due to the importance of this region regarding global climate dynamics, the lack of quality age control for the central Arctic Ocean is a problem.

The aim of this study is the development of an age model for central Arctic Ocean sediments using an approach based on the precise sources of detrital, anhydrous Fe-oxide minerals (Fe grains) and distinct down-core variations of physical characteristics. More specifically, this work attempts to transfer an age model based on oxygen-isotope stratigraphy from JPC22 from the Fram Strait area (Yermak Plateau) that extends to ca. 140 ka to an undated core (JPC9), on the Mendeleev Ridge, ~2200 km distant (**Figure 1**). These two cores were chosen because they are both located along the TPD drift path and ideally positioned to record major variations in the dominant ice drift pathways. The basic premise is that ice-rafted detritus (IRD) from unique sources will deposit sediment markers in both the Mendeleev Ridge and Yermak Plateau sediments that can be used for correlations.

5.3 JPC9 Age Model Development

5.3.1 Age Model Framework and Development

An initial framework of estimated age-depth relationships was applied to core JPC9 from the Mendeleev Ridge by correlation to a nearby core HLY0503-JPC08 (Mendeleev Ridge; 79 35.6’ N, 172 30.1’ W; 2792 mwd; henceforth JPC8). Core JPC8 was retrieved from less than a kilometer away from the location of JPC9 (**Figure 1**).

JPC8 has been extensively studied and a qualitative age model has been developed using radiocarbon dating, and amino acid racemization dating, and stratigraphic correlation to central Arctic Ocean records with established age models (Adler et al., 2009; Polyak et al., 2009). Due to the extensive previous investigation of JPC8, core material was unavailable for use as part of the current research. Additionally, JPC9 provides a more continuous record that is more suited for an investigation of age control.

Two techniques Adler et al. (2009) used to model JPC8, radiocarbon dates and amino acid racemization, can be problematic in Arctic sediment records. The former is subject to poorly constrained reservoir corrections that often result in dating errors. Errors in ventilation age can vary by thousands of years (up to 10 ka in some cases) in Arctic regions, as inferred for the Norwegian Sea and North Atlantic (Sarnthein, 2011; Thornalley et al., 2011; Thornalley et al., 2015). Furthermore, large fluxes of suspended carbonate entering the Arctic as glacial flour from under North American ice sheets could bias radiocarbon dates and result in anomalously old dates, although this has been considered and not deemed a major influence (Polyak et al., 2009). Amino acid racemization dating in the Arctic also has limitations, as the rate of racemization is both species and environmentally dependent (Miller and Mangerud, 1985; Miller and Brigham-Grette, 1989). The method is associated with a standard error of 10-15%, so older dates have proportionally increased potential error (Kaufmann et al., 2008; Adler et al., 2009). Thus, the older the obtained date, the higher the potential error. For example, as shown in Figure 29 that lists the estimated age-depth relationship from 23 AAR dates provided in Adler et al. (2009), numerous inversions are evident and ages range widely, especially at depth. This error in AAR dating is a result of poorly understood environmental controls on the rates of racemization in polar waters, such as how pH and temperature impact these rates (Kaufmann et al., 2008). Figure 29 also shows the location of a prominent slump or gravity flow feature in JPC8 between 270-350 cm which complicates the interpretation of a portion of the late Quaternary in this record.

Based upon these age-dating errors, the JPC8 age model is considered qualitative due to dating complications and the low and variable rates of sedimentation in the region and is thus best used for determining relative timing of events in the central Arctic and in a global context (Polyak, pers. comm.). Regardless of the issues with the JPC8 age model, it still provides an age framework on which refinements can be made.

While not intended for a continuous age model, a model for JPC8 was interpolated to provide a comprehensive framework for correlation with JPC9 using the published dates for JPC8. In total twentyone (21) age-depth points were chosen to interpolate a basic age model framework for JPC8 (**Figure 30**; gray line). Of these tie-points, the majority consisted of radiocarbon dates, identified MIS boundaries, and estimated glacial midpoints; only one AAR date was deemed useful as most were inverted or in direct conflict with more reliable dates. One necessary adjustment from the Adler et al. (2009) model was based on a misinterpreted Stage designation centered on the slump feature in JPC8. Initially, the Stage 5e/6 boundary in JPC8 was placed above the slump feature but later reassessed to occur below the slump (Polyak, pers. comm).

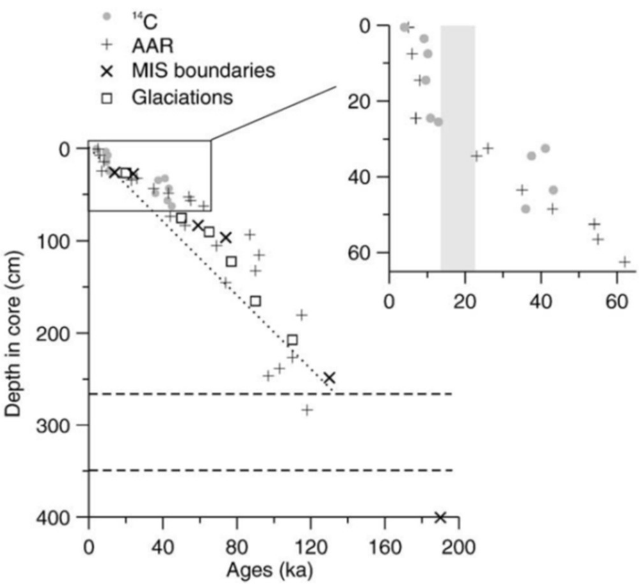

AAR Age-Depths	
Depth (cm)	Est. Age (Kyr)
1	4
8	6
15	8
25	7
34	23
32	26
43	35
49	43
52	54
57	55
62	62
75	43
85	52
95	87
105	67
118	93
133	90
148	74
180	115
226	110
235	102
248	97
280	118

Figure 29. JPC8 age model from Adler et al. (2009). Embedded table indicates the estimated Amino Acid Racemization age-depth tie-points for JPC8 to highlight the errors associated with this age-date method. The vertical gray bar indicates the slump feature.

An initial correlation between JPC8 and JPC9 was based on core physical properties (sediment color as lightness, density, and magnetic susceptibility), with subsequent adjustments based on the comparison of relative foraminiferal abundance between the two cores. This comparison provided the first-order correlations to produce an initial age model for JPC9 (**Figure 30**; orange line). In total, 43 age-depth correlation tie-points were incorporated into the model (**Table 10**).

5.3.2 Age Model Refinement

After establishing the initial age framework, the age model for the JPC9 record was refined to oxygen-isotope stratigraphy through correlation to JPC22. This refinement was performed through comparison of similarities in Fe-Oxide provenance signals, inferred as drift path deposits.

A comparison of dominant source signals (e.g. Banks Island and Kara Sea) indicated a potential, yet weak and noisy, inverse correlation. At core JPC9, when the predominant source signal is from the Banks Island/North American region, the inputs from the Kara Sea are reduced. Likewise, when Kara Sea source inputs to JPC9 are increased, the Banks Island/North American inputs are reduced. For JPC22, in Fram Strait, this signal is also identified. The primary difference at JPC22 is that the Kara Sea sources dominate, and the Banks Island/North American signals are reduced. This implies several things, 1) mixing between the TPD and BG occurs near to or upgradient of the JPC9 location and 2) the TPD and BG signals can be used to qualitatively investigate this mixing through time, and 3) this mixing can be used as a correlative tool. When mixing is occurring, increased TPD sediments enter the BG and are deposited at JPC9; likewise, during increased mixing, a stronger BG sediment signal will be found in the Fram Strait. Thus, a comparison of these signal ratios should aid in the identification of correlation tie points. Conversely, when TPD and BG mixing is minimized the ratios of TPD/BG (JPC9) and BG/TPD (JPC22) will remain very low.

Using the signal ratios of TPD/BG (JPC9) and BG/TPD (JPC22) plotted versus time or depth, several correlative tie points are identified (**Table 10**). A comparison of the final TPD/BG signal based on the JPC9 model compared to the BG/TPD signal of JPC22 is provided in **Figure 31**. The TPD signal was constrained as the combined source are matches from several Fe-oxide provenance groups within the Laptev, Kara, and East Siberian Seas. Source area matches were combined to constrain the BG signal and is represented by the western Canadian Islands (namely Banks and Victoria Islands), the Mackenzie River, and the northern Alaska shelf through to eastern Chukchi Sea. By taking the ratio of TPD/BG (JPC9) and BG/TPD (JPC22), a direct relationship between the central Arctic and Fram Strait is evident (**Figure 31**). When the TPD sources increase in the central Arctic there appears to be an associated increase in BG sources at Fram Strait. Thus, the ratios of the TPD and BG signals allows a qualitative measure of current mixing that occurs in the central Arctic. The use of these signals as a correlative tool is not without fault, as there can be situations where BG material bypasses the central Arctic and exits along the coast of North America.

Based on the TPD/BG (and BG/TPD) signal, sixteen (16) additional correlations between JPC9 and JPC22 were identified (**Table 10**). These tie-points resulted in several age differences and inversions when comparing the JPC8-JPC9 correlation with the JPC9-JPC22 correlation. Each discrepancy was examined, and if the age difference was large or inverted the JPC9-JPC22 correlated age was used. This is because the age control on JPC22 is considered stronger, as it is linked to oxygen-isotope stratigraphy. Using these TPD/BG based tie-points, the final age model adjustments were made (**Figure 30**; black line). In total forty-six (46) age-depth correlation tie-points were incorporated into the model, and therefore thirteen of the original JPC8-JPC9 age-depth tie-points were dropped. As a result, the JPC8 model can also be refined, but this was not performed as part of this study. Comparisons were not made between JPC22 and JPC9 based on foraminiferal abundance, because the abundance in JPC22 is highly influenced by sub-Arctic environmental conditions of the North Atlantic.

Table 10. Final correlation tie-point table for JPC9 age model. Source indicates the core from which the tie-point was derived. JPC8 tie-points are based on core physical properties. JPC22 tie-points are based on the TPD/BG and BG/TPD comparison.

9JPC Depth	Age (kya)	Source	9JPC Depth	Age (kya)	Source
0	0	core top	117	76.7	JPC8
2.5	3.32	JPC22	122	77.2	JPC8
8	10.3	JPC8	130.5	78.5	JPC8
12	10.4	JPC8	134	79.6	JPC8
12.5	11.7	JPC22	142.5	85.5	JPC22
22	12.95	JPC8	154	89.6	JPC8
25	25	JPC8	154.5	89.9	JPC22
28.5	28.6	JPC22	166	91.3	JPC8
30.5	38.1	JPC22	166.5	91.7	JPC22
35	39.7	JPC8	168	95.2	JPC8
38	40.5	JPC8	170	96.5	JPC8
44.5	42.6	JPC22	170.5	98.4	JPC22
53	43.8	JPC8	182	103	JPC8
59	45.9	JPC8	190.5	108.9	JPC22
61	46.7	JPC8	191	110.3	JPC8
63	57.2	JPC8	194.5	111.2	JPC22
76.5	64.2	JPC22	201	117.9	JPC8
78.5	67.5	JPC22	214	119.3	JPC8
82.5	70.6	JPC22	215	119.4	JPC8
90	71.7	JPC8	218	119.6	JPC8
93	72	JPC8	227	120.2	JPC8
98.5	72.8	JPC8	266.5	130.4	JPC22
101	73.7	JPC8	314.5	139.9	JPC22
107	75.2	JPC8			

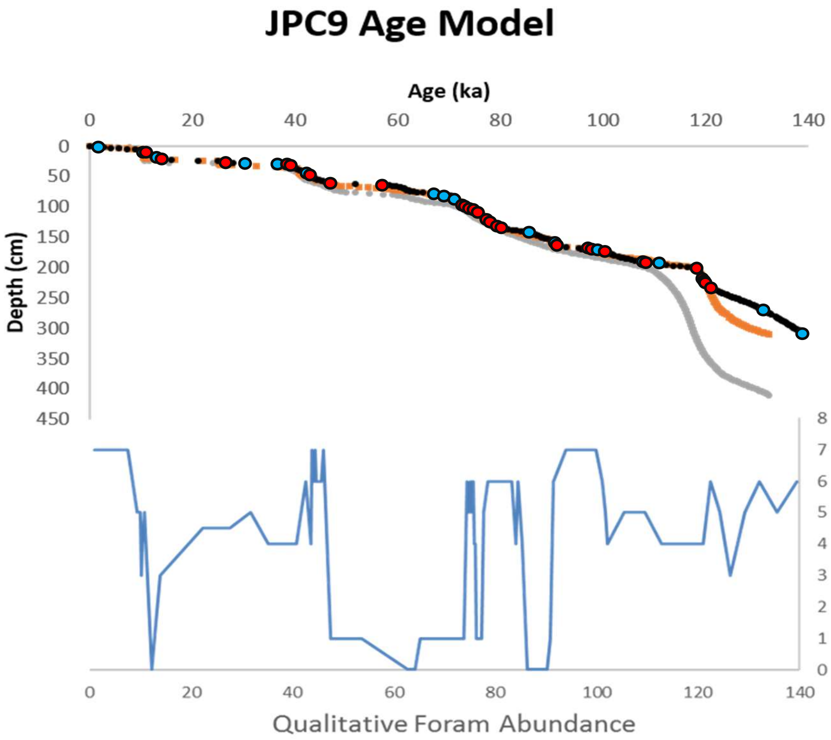

Figure 30. Age model for JPC9. The gray line indicates the JPC8 age model framework. The sharp dip at ~118 ka represents the prominent slump feature identified in JPC8 (Adler et al., 2009). The orange line represents the first iteration of the JPC9 model and consists of a PCHIP interpolation of 28 correlation tie-points between JPC8 and JPC9, based on sediment lightness, density, and magnetic susceptibility; but also includes adjustments for Stage boundaries and relative foraminiferal abundance. Foraminiferal abundance is shown, qualitatively defined as absent (0) to very abundant (8). The black line represents the final iteration of the JPC9 model, incorporating mineral and source comparisons between JPC22 and JPC9 including comparisons of TPD/BG and BG/TPD. Red dots: age-depth tie-points from JPC8. Blue dots: age-depth tie-points from 22JPC.

5.4 Results

5.4.1 Age Model

Core JPC9 was collected from the eastern flank of the Mendeleev Ridge, from a depth of 2783 meters below sea level (**Figure 1**). The primary source of terrigenous sediment input to JPC9 is presumed to be via ice transport (sea-ice and/or icebergs). However, there is potential for significant terrigenous inputs to the core site from turbidity currents and winnowed silts from bathymetrically higher areas along

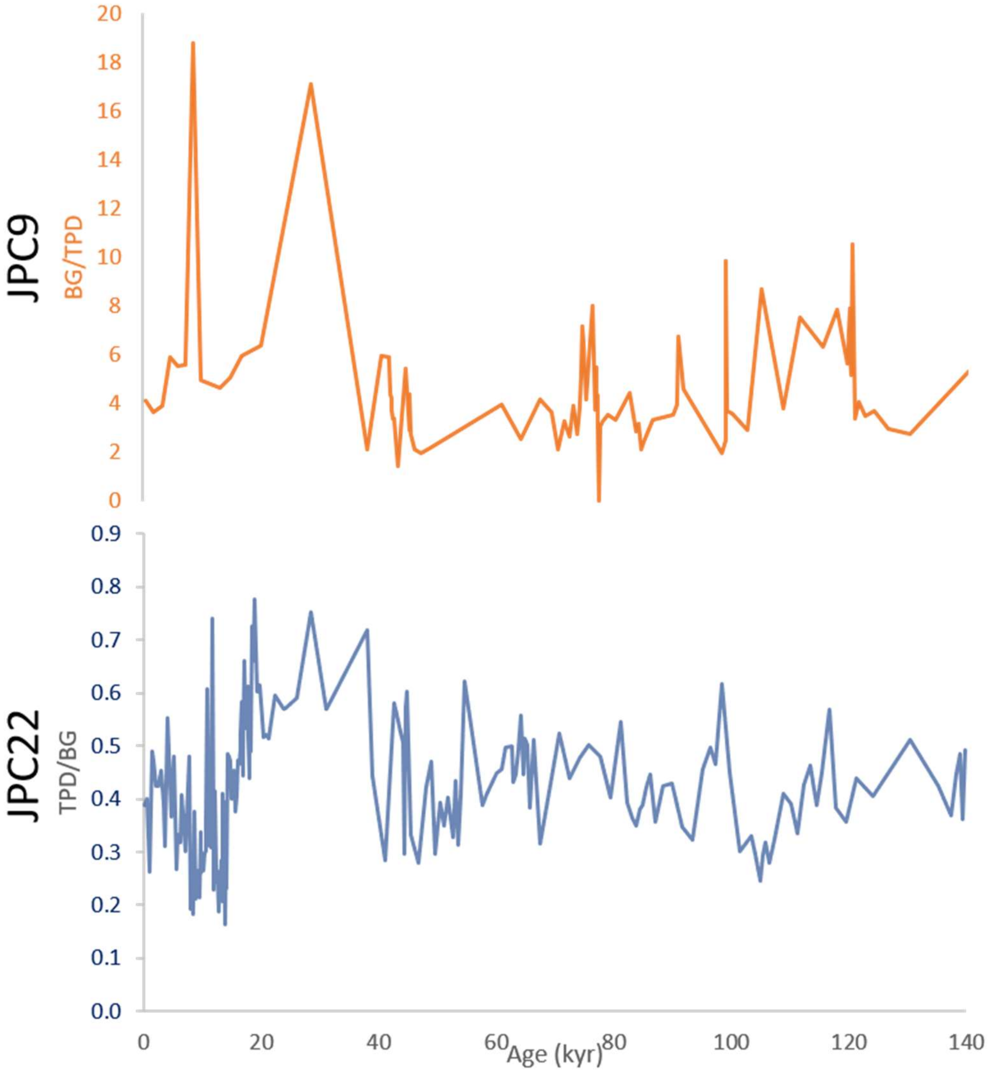

Figure 31. TPD/BG (JPC22) and BG/TPD (JPC9) ratios plotted against age. The basis of the TPD/BG signal is detailed in the text.

Mendeleev Ridge. The potential for turbidity current sources is high considering the large slump feature identified in core JPC8 less than one kilometer to the west and from roughly the same depth (Adler et al., 2009; Polyak et al., 2009). Unlike the neighboring JPC8, this slump feature is not identified in the JPC9 record, so it is assumed that major turbidity deposits do not impact this core. Consistent deposition from bathymetrically higher winnowed sediments would impart a higher sedimentation rate in JPC9. Given the high sedimentation rate (2.2 cm/kyr) and the high silt content for JPC9, winnowed sediments from upgradient along the Mendeleev Ridge probably contribute significantly. The proximity of JPC9 to the East Siberian Sea and Chukchi Sea shelves, known to be a region of high-volume sea-ice production (Eicken et al., 2005; Darby et al., 2011), may impart a sediment signal bias from these Eurasian regions.

Based on the presented age model, the average sedimentation rate for this Mendeleev Ridge core (JPC9) through the Late Quaternary to present is 2.2 cm/kyr. Strong variations in accumulation rates are identified between glacial and interglacial periods (**Table 11**). Accumulation rates in JPC9 range from periods of nondeposition during the Stage 2 glacial maximum to inferred rates up to 8.9 cm/kyr during the MIS 2 deglacial.

Sedimentation during interglacial periods is generally higher than during glacial periods, while rates of sediment accumulation across stage transitions do not appear to exhibit consistent trends. This is the opposite of rates found in JPC22. In general, warm stages are texturally coarser than cool stages. Warm period coarseness is buoyed by the large volume of glacial ice entering the Arctic during deglacial phases. This coarse trend during warm periods is not identified during Marine Isotope Stage 1.

Table 11. Calculated sedimentation rates for JPC9 and the average sediment texture for each Marine Isotope Stage (MIS).

JPC9		Stage Texture (average %)				
Stage Designation	**Calculated Sedimentation Rate (cm/kyr)**	**<45 µm**	**45-63 µm**	**63-250 µm**	**>250 µm**	**>45 µm**
Core Average	**2.2**	**92.5**	**1.3**	**5.0**	**1.2**	**7.5**
MIS 1	1.7	95.3	0.5	2.5	1.7	4.7
MIS 2	0.8	94.1	0.9	4.0	1.0	5.9
MIS 3	1.9	88.1	1.9	8.8	1.2	11.9
MIS 4	1.2	97.7	0.4	1.5	0.3	2.3
MIS 5	3.0	91.8	1.5	5.4	1.3	8.2
5a	4.6	91.7	1.4	5.5	1.3	8.3
5b	3.8	94.8	0.9	3.5	0.8	5.2
5c	1.2	92.2	0.8	6.6	0.3	7.8
5d	1.3	96.0	1.0	2.5	0.6	4.0
5e	5.0	89.1	2.3	6.6	2.1	10.9
Late MIS 6	5.0	94.3	1.2	3.9	0.6	5.7

5.4.2 Accumulation Events

Several periods of enhanced or reduced sediment accumulation are identified within the investigated JPC9 record (**Table 12**). Nine rapid units (R1-R9) were identified with accumulation rates of >4 cm/kyr, or approximately twice the core average sedimentation rate for core JPC9 (2.2 cm/kyr). The calculated rates range from 4.0 cm/kyr to 8.9 cm/kyr, with one Holocene rapid event exhibiting a calculated rate exceeding 60 cm/kyr over a very short interval (2 cm). Units of slow sedimentation are identified as intervals with accumulation rates significantly lower than the core average (generally <1 cm/kyr). Six total events are identified and designated as units S1-S6 and range from 0.3 cm/kyr to 1.4 cm/kyr.

Through these units, no consistent trends are noted for textural, provenance, or mineralogical characteristics across all rapid or slow accumulation event types. For instance, most rapid events are associated with a moderately-coarse to coarse texture consistent with sea-ice and glacial IRD, but a few are fine grained (units R1, R2, and R7). Similarly, during slow events, both fine and coarse textures are identified. While sediment provenance from proximal source areas can be attributed to some units which may suggest localized or regional events, others show distant source provenance indicative of basin-wide events. Brief descriptions of these units are provided below.

5.4.2.1 Rapid Sedimentation Units R1, R2, and R7

Events R1, R2, and R7 have calculated accumulation rates of 66.7 cm/kyr, 8.9 cm/kyr, and 6.7 cm/kyr, respectively (**Table 12**). Sedimentation across unit R1 is calculated over a very short 2 cm interval perhaps covering a period of less than 100 years (circa 10.3 kya). The error within the JPC9 age model precludes the determination of the duration of unit R1, but it can be stated that this event constitutes a very rapid deposit. Unit R2 represents the late pre-Holocene period of 11.7-12.5 kyr. Unit R7 comprises late Substage 5c and covers the period of 89.9-91.7 kyr.

The texture of these three units is distinct and very fine, with the average <45 μm fraction constituting >97% of the bulk sediment (**Figure 32**; **Table 12**). Each of these units contain very few Fe-oxide grains of which very few were matched (3 to 6 average matches). Although these matches are low, units R1 and R2 appear to initially match to North American sources with the latter exhibiting a strong Chukchi Sea source and capped with a slight increase in Kara Sea sources. Unit R7 exhibits a change in matches from North America (mainly Banks and Victoria Island) and Laptev Sea, followed by the Kara Sea and then East Siberian Sea.

The mineralogical signals for units R1, R2, and R7 are generally consistent with the Fe-oxide provenance signals (**Table 13)**. For unit R1, dolomite, smectite, and chlorite signals are slightly elevated above the core averages which is consistent with a primary North American and secondary Laptev Sea source. Unit R2 mineralogy exhibits a below average but increasing dolomite signal, below average smectite concentration and an above average concentration of chlorite. Across unit R7, mineralogy exhibits a strong drop in chlorite, increasing smectite and expansive clays, and an overall low concentration of dolomite. Unit R7 was not fully sampled and analyzed for mineralogy with the early portion missing. If like R1 and R2, where the dolomite signal is restricted to the early portion of the event, the dolomite signal in R7 would be missed.

Table 12. Identified rapid (R) and slow (S) depositional events in JPC9. Rates of sedimentation and texture (>63 µm fraction) through these units and associated MIS designations are listed. Potential correlated events corresponding to Greenland stadial/interstadial, Heinrich, and Coarse Events are provided (Darby et al., 2002; Hemming, 2004; Darby and Zimmerman, 2008; Rasmussen et al. 2014). The varying shades of gray indicate when events are temporally related.

					Rasmussen et al., 2014 (Hemming, 2004)		Darby et al., 2002 (Darby & Zimmerman, 2008)	
Event	**Age (ka)**	**JPC9 ate (cm/kyr)**	**Texture (>63 µm)**	**Stage**	**Correlated Event ID**	**Event Age (kya)**	**Correlated Event ID**	**Event Age (kya)**
S1	0 - 9.4	0.7	8.1	MIS 1	–	–	–	–
R1	10.32 - 10.35	66.7	1.4	MIS 1	9.3 ka Event	9.3	(IRD 1)	(10)
R2	11.7 - 12.6	8.9	1.3	MIS 1	Holocene / GS-1	11.7 - 12.9	H0 / AL1	12.2 / 12.9
S2	13.8 - 38.1	0.3	5.0	MIS 2 / 3	GI-8c	38.2	–	–
R3	39.1 - 39.6	4.0	4.5	MIS 3	GI-8c / GS-9 (H4)	38.2 - 39.9 (38)	(IRD 7)	(38.9)
R4	42.6 - 44.2	6.2	9.3	MIS 3	GS-11 / GI-11 (H5)	42.2 - 43.3 (45)	–	–
S3	46.4 - 69.5	0.9	4.0	MIS 3 / 4	GS-19.1 / GI-19.1	69.4 - 69.6	–	–
R5	70.6 - 72.8	7.3	9.6	MIS4 / 5	GS-19.2 / GI-19.2	70.4 - 72.3	–	–
R6	74.7 - 78.5	6.8	4.7	MIS 5 (a)	GI-20b / GI-21.1a	74.4 - 78.1	–	–
S4	79.8 - 85.5	1.4	5.7	MIS 5 (a/b)	GI-21.1d / GI-21.2	79.7 - 85.1	–	–
R7	89.9 - 91.7	6.7	2.4	MIS 5 (b/c)	GI-22e / GS-23.1	89.8 -90.1	–	–
S5	91.7 - 98.4	0.6	6.2	MIS 5 (c)	–	–	–	–
S6	111.2 - 115.7	0.9	0.8	MIS 5 (d)	GI-25b / GI-25c	111.4 - 115.7	–	–
R8	119.0 - 122.3	8.5	11.2	MIS 5 (e)	GS-26	119.1	–	–
R9	129.4 - 139.2	4.9	5.2	MIS 5/6	–	–	–	–

The qualitative foraminiferal abundance through units R1, R2, and R7 exhibit high counts at least for portions of the units. Unit R2 starts with a very low foraminiferal component that rises to very high and continues through unit R1. In contrast unit R7 begins with a high foraminiferal content which reduces through the unit to very low. When coupled with the difference in provenance identified between units R1/R2 and R7, this stark difference in foraminiferal abundance implies very different environmental conditions for units R1, R2 and R7.

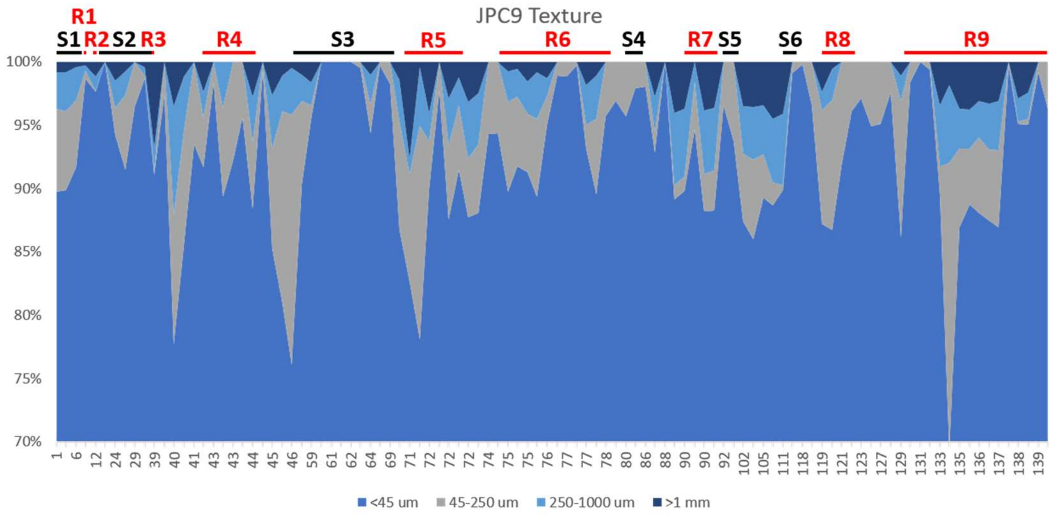

Figure 32. JPC9 Texture. Percent contribution is presented on the y-axis and age (ka) is presented on the x-axis. Several major coarse excursions are evident, and Rapid (red) and Slow (black) events are noted. Also note that the age scale is nonlinear and variable.

5.4.2.2 Rapid Sedimentation Units R3, R6, and R9

The slowest of the rapid accumulation events, units R3, R6 and R9, reveal calculated sediment accumulation rates of 4.0 cm/kyr, 6.8 cm/kyr, and 4.9 cm/kyr, respectively (**Table 12**). Unit R3 represents a short sediment excursion during late Stage 3 (39.1-39.6 kyr). Unit R6 is a moderate duration (3.8 ka) event during late Stage 5 (Substage 5a). Unit R9 is an approximately 9.8 ka interval characterizing late Stage 6 and a short portion of early Substage 5e. The foraminiferal abundance through these units is consistent with their placement within the overall JPC9 age model (**Figure 32**). Unit R3 occurs during an interglacial period and exhibits moderately high qualitative foraminiferal abundance, while units R6 and R9 cover stadial conditions and the terminus of a glacial stage and exhibit an expected low foraminiferal abundance associated with increased ice.

Units R3, R6, and R9 exhibit moderate coarse texture with an average <45 µm composition of 94.2%, a >63 µm composition of 4.4% (**Figure 32**). Through these three units, an average of 25 Fe-oxide grains were matched. Unit R3, within Stage 3, exhibits average matches of 13 grains and an average provenance influx from four prominent circum-Arctic source groupings (Eurasian and North American). The unit culminates with very low inputs from the Kara and Laptev Seas, while other provenance regions maintain consistent inputs. Unit R6 has low total matches early that increase during the latter half of the unit. Even with low numbers of matches, the Fe grain match has an error of only 1.5% so that even one or two grain matches are significant (Darby et al., 2015). Eurasian and North American sources are roughly proportional throughout the unit with the latter presenting the strongest signal. Unit R9 begins with a strong North American signal and ends with very high inputs from the Laptev Sea area but lacks significant input from other sources.

Based on the timing, texture, and provenance trends of unit R3, it is inferred that sea-ice transport dominates this interval. While initially receiving inputs from the full eastern Arctic Shelf area as well as from the North American inter-island channels (such as the Amundsen Gulf ice stream), the Kara and Laptev Sea sea-ice flux was shifted or restricted from reaching the Mendeleev Ridge. The possibility for reduced melt-out rates is precluded by the consistent sedimentation through this interval from other circum-Arctic sources.

Unit R6 begins with lower overall matches that rapidly increase and is coincident with increasing coarseness. This trend is indicative of increasing ice volume, transport, and melt-out. The initial influx through this unit is characterized by the Laptev and Chukchi Seas, however as the total matched grains increase these sources are offset by increased sediment flux from Banks and Victoria Islands and East Siberian Sea sources.

Unit R9 exhibits strong fluctuations of total matched grains through the unit. Initially, matches are low, approximately 10 grains matched, and almost exclusively sourced to North America. Total matches increase through approximately 137 ka (rising to an average of ~70 matches), and no source area dominates, rather inputs from major source regions are uniform (**Figure 33**). This period is followed by a slight reduction in matched grains (average 22 matches) before ramping up again to greater matches (average 60 matches). This latter period of high matches has very low inputs from the Chukchi Sea area with very high Laptev Sea influx, perhaps evidence of glacial ice build-up on the Chukchi Rise and Plateau (Borderland) preventing North American and Chukchi sources from reaching Mendeleev Ridge (JPC9).

Table 13. Generalized provenance sources for identified rapid and slow sedimentation events. Note: Asterisks indicate finer grained units where very few Fe-oxide grain matches were made.

		Provenance
Type	**Event ID**	**Dominant Sources**
Rapid Events	**R1***	*average 3 matched grains; North American
	R2*	*average 3.3 matched grains; North American
	R3	North American (48.5%); mostly eastern CAA
	R4	Eurasian Sources dominate, starting with Kara Sea, successive replacement by more eastern sources through interval
	R5	Brief early North American signal; replaced by East Siberian and Laptev Sea Sources
	R6	Low early total matches, Strong SA8/ESS/Chukchi singal in later half, weak overall Kara signal throughout
	R7*	Low overall matches, stongest signal from Kara and Laptev Seas
	R8	Low to average Laptev Signal, interval capped with strong Kara Sea pulse
	R9	Weak Source Signals throughout unit, but capped with strong Laptev Source signal.
Low Rate Events	**S1**	Strong Eurasian signal throughout, with a late flux of SA8
	S2	Initially strong ESS/Laptev/Chukchi flux, capped with SA8 flux
	S3	Strong initial Kara signal, replaced by Laptev; low North American signal
	S4	Strong Kara and Laptev signal, with late flux of Chukchi sources
	S5*	Low matches, ESS early followed by increased Laptev and North American sources
	S6*	Low matches, Chukchi and North American early, followed by Laptev and ESS increase, Kara inputs very low.

5.4.2.3 Rapid Sedimentation Units R4, R5, and R8

Displaying the coarsest texture of all rapid units, units R4, R5, and R8 exhibit an average <45 µm composition of 87.7%, 45-63 µm fraction of 3.2%, 63-250 µm fraction of 3.5%, and 1.2% >250 µm fraction (**Figure 32**). Unit R4 occurs across a 1.6 kya duration (42.6-44.2 ka) during mid-Stage 3 and exhibits a calculated accumulation rate of 6.2 cm/kyr. Unit R5 represents a 2.2 kyr (70.6-72.8 ka) rapid event during late Stage 5 (5a) interglacial (interstadial) and covers the transition into glacial Stage 4. The calculated rate associated with unit R5 is 7.3 cm/kyr. Unit R8 exhibits an accumulation rate of 8.5 cm/kyr for a period of 3.3 ka. In general, the primary sources of these sediments are varied but from known glaciated regions.

Fe-oxide matches for these three units are moderate to high and all contain high foraminiferal counts, suggesting high melt-out rates due to thin ice or open leads (**Figures 32** and **33**). Unit R4 exhibits a reduction in matches through the interval (overall average 16 and expresses a strong initial flux from the Kara and Laptev Sea areas and later joined by Chukchi and East Siberian Sea sources. The mineralogical signal through unit R4 displays a strong kaolinite signal possibly related to the elevated kaolinite around Franz Josef Land. Additionally, there is an increasing smectite signal that conforms with the Kara and Laptev Sea signal (**Figure 33**).

The interval of unit R5 has an average match count of 46 matches, with a trend of increasing matches through the unit. Early unit matches indicate elevated North American and East Siberian Sea sources and a depressed signal from the Laptev Sea, which is immediately followed by a depression in the North American signal. The latter half of the unit is characterized by an initial pulse of Kara Sea sources with a lagging signal from East Siberian and Laptev Seas. Mineralogy through this unit is consistent with the Fe-oxide source provenance. A lack of a dolomite signal indicates that the primary North American source is from the eastern Canada region and/or the Alaskan regions. The chlorite signal starts strong and reduces in concentration through the interval. Again, this chlorite signal is consistent with the strong initial East Siberian Sea signal which likely catches some of the chlorite-rich Chukchi Sea region. This unit initially has very high foraminiferal content that reduces through the interval to very low abundance.

Based on the timing, coarseness, and strong mineralogical and provenance signals from historically glaciated regions, the events of units R5 and R8 are typical of glacial IRD deposits. The lack of a strong >250 µm fraction within unit R4, coupled with the sweeping influx of Eurasian sources beginning with the Kara and Laptev Seas and subsequently replaced by more eastern sources implies a likely regional scale sea-ice transport event with high melt-out rates.

5.4.2.4 Slow Sedimentation Units S1 through S5

Several slow sedimentation events are identified within the JPC9 age model and typically have long durations, ranging from 5.7 to 24.3 kyr. The average sedimentation rate of these five units is 0.8 cm/kyr, with a range of 0.3 (S2; 13.8-38.1 ka) to 1.4 (S4; 79.8-85.5 ka). Unlike the rapid events, most of the slow accumulation events share a similar textural composition. Five of the six slow sedimentation events, S1-S5, exhibit an average textural composition of 93.3% <45 µm, 0.9% 45-63 µm, 4.7% 63-250 µm, and 1.1% >250 µm (**Table 11**). The total number of matched Fe-oxide grains through these intervals varies (range 6 – 49 matches), averaging 27 matched grains.

Of these five events, units S1, S2, and S5 show similar provenance signals with an apparent initial flux of sediment originating from the eastern Arctic followed by a subsequent flux of western Arctic sources. Units S3 and S4, however, only exhibit significant sediment flux from the eastern Arctic region (**Figure 33**).

Initial sediment flux associated with unit S3 (0-9.4 ka) is from Chukchi and eastern Laptev Sea sources with a later flux from Banks and Victoria Islands and the East Siberian Sea. Unit S2 (13.8-38.1 kyr) begins with an initial flux from the East Siberian, Laptev, and Chukchi Seas followed by a strong reduction in Laptev Sea influx and the interval is capped with a strong Chukchi Sea and Banks and Victoria Island signal. Although matches are particularly low for unit S5 (91.7-98.4 kyr; average of 6.5

matched grains through the interval), the unit begins with a strong influx of East Siberian Sea sources followed by increase in North American and Laptev Sea sources (**Figure 33**).

Units S3 and S4 primarily exhibit sediment flux from the eastern Arctic regions with very little input from the western Arctic. The early half of unit S3 (46.4-69.5 kyr) exhibits a high concentration of matches sourced to the Kara Sea region that is later joined by increased flux from the Laptev Sea area. Approximately midway through this unit, the Kara Sea signal declines and is replaced by East Siberian, Laptev, and Chukchi Sea signals. Unit S4 (79.8-85.5 kyr) is elevated in Kara and Laptev Sea sources between 85.5 and 82.7 kya, afterwards these source signals are replaced with strong increase in Chukchi Sea sources.

5.4.2.5 Slow Sedimentation Unit S6

Of the six slow accumulation events, only unit S6 (0.9 cm/kyr; 111.2-115.7 ka) exhibits an extremely fine texture, with 99% of the bulk sediment through this interval classified as <45 µm (**Figure 32**). An average of 7.5 Fe-oxide grain matches are obtained through this interval, beginning with a North American and Chukchi Sea signal that is subsequently replaced by a Laptev and East Siberian Sea signal. The Fe-oxide provenance determinations through this interval is limited by the low number of grain matches.

Although the interval is not fully investigated for mineralogy, the general mineralogical trends do not fully support the Fe-oxide provenance. Based on the texture of this interval, the mineralogical data is likely more indicative of environmental changes during this period. The initial chlorite signal in this interval is elevated which is indicative of the Chukchi Sea region

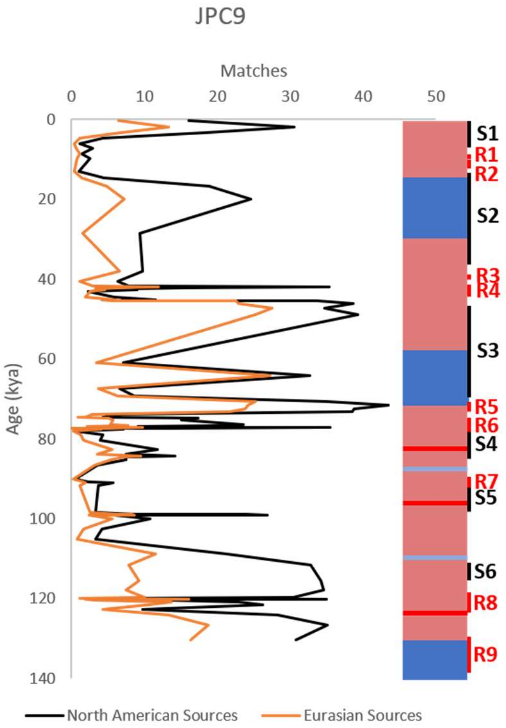

Figure 33. Contributions to JPC9 from prominent source areas. Marine Isotope Stages/substages are denoted by the color bars. Rapid and Slow events are labeled. The North American Sources include all source regions from Northern Greenland to Alaska. The Eurasian sources include sources from Kara Sea through the western Chukchi Sea.

which is a prominent source of chlorite within the western Arctic. Counter to the Fe-oxide provenance matches that show decreasing Chukchi Sea sources, this chlorite signal appears to increase through time. Similarly, dolomite is initially low and appears to increase through the interval. In contrast, the smectite signal appears to decrease through this interval. These data imply that North American and Chukchi Sea inputs to JPC9 are likely more continuous through this interval, contrary to the Fe-oxide provenance results based on low numbers of matched grains. This conflicting source provenance might be due to differences in sediments size and the associated mode of transport, with the concentrated fine-grained chlorite (clay) capable of being transported farther distances via currents and is not reliant on melt out rates as are the coarser sand fractions.

5.5 Discussion

5.5.1 Age Model

This work builds on the age model framework developed for JPC8 (Adler et al., 2009; Polyak et al., 2009) which was limited in resolution due to errors associated with age-dating methodologies (discussed above). Overall, the age model for JPC9 is very similar to that of JPC8 (**Figure 34**); however, small refinements in the JPC9 age model have exposed significant and important features. The notable differences throughout Stage 5 are the result of the JPC9 age model refinement based on correlation to JPC22. The estimated resolution of the model is ± 500 years/cm and based on the error of the nearby JPC8 record (Adler et al., 2009). In this study, the age model for JPC9 was tuned, were applicable, to oxygen-isotope stratigraphy from JPC22 (Fram Strait) and allowed for the identification of strong but brief variations in sedimentation rates. The timing of these depositional events implies a response to glacial and sea-ice transport dynamics related to Marine Isotope Stages (MIS) and other climatic events such as Dansgaard-Oeschger events (DO; Greenland Stadials/Interstadials (GS/GI) and/or Heinrich events (**Table 12**; Hemming, 2004; Darby and Zimmerman, 2008; Steffensen et al., 2008; Rasmussen et al. 2014).

Glacial stages (MIS 2 and 4) exhibit lower overall sedimentation rates (0.8 and 1.2 cm/kyr, respectively) with respect to the interglacial stages (MIS 1, 3, and 5; 1.7, 1.9, and 3.0 cm/kyr, respectively) (**Table 11**). MIS 6 exhibits a high overall sedimentation rate (5.0 cm/kyr) which is probably biased-high by only capturing the end-Stage deglacial activity. Stage 6 likely has a much lower rate of sedimentation probably like that of Stage 2, as evidence suggests that an ice shelf covered much of the central Arctic that would restrict ice movement, melt-out and sediment deposition for parts of this stage (Jakobsson et al., 2016). This variable sedimentation depending on glacial/interglacial environment is typical of central Arctic sediment records (Speilhagen et al., 2004; Polyak et al., 2007; Adler et al., 2009; Polyak et al., 2009; Stein et al., 2010; Jakobsson et al., 2014). Based on texture, the interglacial periods (>63 μm avg. = 6.6%; σ = 5.2%) appear to be slightly coarser than their glacial counterparts (>63 μm avg.

= 3.9%; σ = 4.3). This textural dynamic is somewhat counterintuitive. The explanation may be that much of the deglacial phase(s) (i.e. the large volumes of sediment laden glacial ice transport) is included in the interglacial phases, as defined in this study. Sediment transport or melt-out decreases through glacial periods as noted by the reduced deposition or nondeposition associated with Stages 2 and 4 (Adler et al., 2009; Polyak et al. 2009; Poirier et al., 2012). Error associated with the textural data is approximately ±5%, which increases above 200 µm. Regardless, eventthe average texture between glacial and interglacial periods is still significantly different.

Based on the identification of ice scouring on the Chukchi Borderland and the Lomonosov Ridge it has been proposed that in the past large ice caps existed in the central Arctic Ocean (Grosswald and Hughes, 1999; Jakobsson et al., 2001; Polyak et al., 2001). Similar ice shelves may also develop through the combined effects of seaward glacial extension and extensive thickening of multi-year land-fast sea-ice (Bradley and England, 2008; Jakobsson et al., 2014) The presence of such ice caps or extensive land-fast ice could restrict the transport of IRD within and from the Arctic Ocean or more likely adversely affect melt-out rates. Recent investigations of ice scour features on the Chukchi Borderland and Lomonosov Ridge constrained the timing of the most recent ice grounding to MIS 6 (Jakobsson et al., 2016). While these groundings supposedly did not occur during Stages 4 or 2, a moderate ice shelf on the East Siberian Sea or ice build-up on the Chukchi Borderland could reduce sediment delivery to JPC9 through restricted transport/movement and melt-out. Fe-oxide provenance of sediments from JPC9 indeed reveals a reduced influx of sediment from the East Siberian and Chukchi Seas (**Figure 33**). Provenance of sediments in core JPC22 from Yermak Plateau, however, indicates no substantial reduction in western sources through Stage 2 and 4; thus, there does not appear to be a reduction of sediment entrainment and flux from the East Siberian and Chukchi Sea-ice shelves. Given these findings, it is likely that the reduction in sediment delivery at JPC9 during glacial and stadial phases is the result of reduced melt-out rates and not restricted ice transport to the Mendeleev Ridge area.

Perhaps the most interesting findings from this study is the variability in sedimentation rates identified in JPC9. Several rapid and slow sedimentation events are highlighted within JPC9 (**Figure 30**). The identification of these events highlights significant variations in sediment delivery and melt-out rates in this central Arctic Ocean sediment record.

5.5.2 Rapid and Slow Periods of Sediment Deposition

Several rapid and slow sedimentation events were identified within the JPC9 sediment record and are attributed to known climatic excursions identified in other sediment and Greenland ice core records (**Table 12)**. While these correlations are not confirmed with independent dating, the correlated age similarities are intriguing. The identification of climatic excursions in central Arctic sediment records, such as Dansgaard-Oscheger and Heinrich Events are typically made using biological assemblage proxies and oxygen-isotope measurements (Backman et al., 2009; Poirier et al, 2012), but also Fe-oxide provenance and texture (Darby et al, 2002; Darby and Zimmerman, 2008).

Two primary relationships are identified involving the rapid and slow depositional events. First, and the most common trend, is a period of slow deposition that culminates with a very rapid sedimentation event. This trend is identified four times within JPC9 and is typically related to cool periods that transition into a rapid warming. The second trend, identified twice, exhibits a rapid depositional event followed by a short-lived rebound to average sedimentation and then a reduction in deposition or nondeposition. This trend indicative of a transition into a cool period, with increased sedimentation associated with the increased buildup of ice to a maximum, at which point sedimentation declines in response to reduced ice transport and/or melt-out rates. Several additional rapid depositional events are identified that do not appear related to one of the trends. These events may be isolated, or the associated slow event was missed due to weak sampling resolution. Several of the events identified in JPC9 are also identified in JPC22 (**Figure 34**). In the following sections, each of the oxygen-isotope stages and rapid and slow depositional events are examined in further detail within the context of this newly developed central Arctic age model.

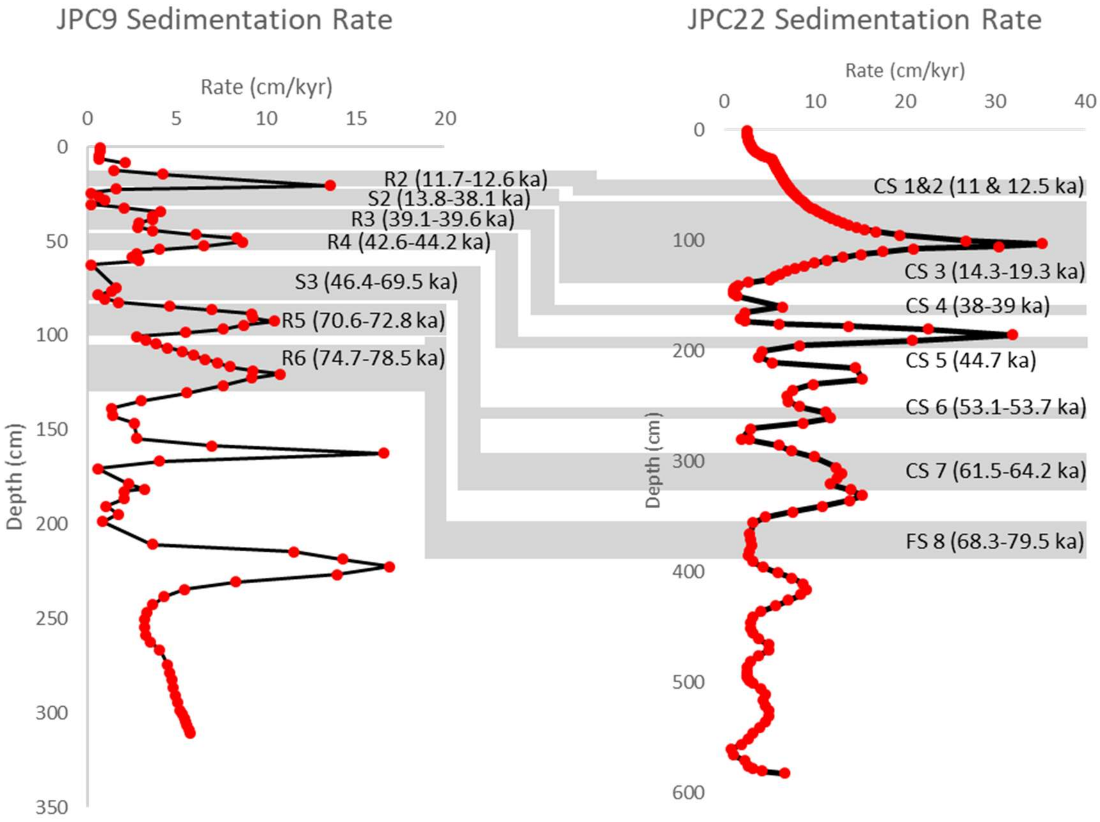

Figure 34. Rapid and Slow events identified in both JPC9 (Mendeleev Ridge) and JPC22 (Fram Strait). Plots show continuously calculated sedimentation rates from both JPC9 and JPC22 for inter-core comparison. JPC9 is compressed relative to JPC22. Note the rapid sedimentation (>65 cm/kyr) at 10.5 cm in JPC9 was removed to allow for increased resolution for visualization purposes. Some peaks in sedimentation correspond with troughs. This mismatch highlights the difference in sedimentation regimes between the two basins and the ability of this correlation method to overcome this difference.

5.5.3 MIS 5

Stage 5 exhibits highly variable sedimentation rates that fluctuate depending on the substages (a-e). The overall rate of sedimentation for Stage 5, based on this age model is approximately 3 cm/kyr (**Table 11**). Within the substages, depositional rates range from 1.2 cm/kyr to 5 cm/kyr (**Table 11**). Foraminifera abundance shows distinct intervals. Based on these abundance estimates, the substage designation may be incorrectly interpolated within the JPC9 age model. However, these abundances were not used in the interpolation as their addition would have resulted in the nullification of 16 age-depth tie-points from JPC8 used in the model. Since these JPC8 ages were determined via traditional dating methods such as radiocarbon and amino acid racemization dating (Adler et al., 2009), they were retained.

Within JPC9, Stage 5 sediments are sourced to all the Eurasian Seas as well as North America. The number of matched grains covaries with the coarseness of the sampled interval, with coarser intervals obviously providing increased matched Fe-oxide grains to Eurasian and North American sources. The end of Stage 5 is identified as the very pale brown and pinkish, dolomite-rich interval at the base of brown interval B3 (brown unit designations from Clark et al., 1980; ca. 75 ka; Adler et al., 2009; Polyak et al., 2009). This dolomite signal originates from Banks Island in the western Canadian Arctic and corresponds to the interval of 102.5-110.5 cm (74.1-75.8 ka). Substage 5a corresponds to brown interval B4 (Polyak et al., 2004, 2009; Adler et al., 2009), or alternatively to brown interval B5 (Backman et al., 2009; Stein et al. 2010). Within the age model presented here for JPC9, substage 5a is presumed coincident with that of B3 (Adler et al., 2009).

Prior to Substage 5e and comprising the Stage 6/5 transition, rapid depositional event R9 (129.4-139.2 ka; 262.5-310.5 cm) is identified. This unit encompasses the Stage 6 deglacial period. This event is firmly within Stage 6 and implies that much of the Stage 6 deglacial phase occurred before the transition into Stage 5. The rapidly deposited interval begins with a strong North American flux, although the number of matched grains is low; and is followed by a reduction in most sources. A short-lived flux of Chukchi Sea influx is identified in the middle of event R9, and the interval is capped by North American and Laptev Sea influx. Texturally, this interval exhibits prolonged periods of very coarse sediment, with 278.5-306.5 cm exhibiting increased >250 µm fractions. These textural and provenance characteristics are consistent with iceberg IRD transport.

Substage 5e is identified as a thick brown sediment interval within JPC9 (210.5-262.5 cm) with a high rate of deposition (5 cm/kyr). Overall this interval exhibits a fine texture (average >63 µm – 4.4%). Two short intervals of coarse texture are identified (262.5 cm and 214.5-218.5 cm), where significant >250 µm flux is encountered. Fe-oxide provenance through Stage 5 shows consistent flux from North

American, East Siberian, Chukchi and Kara Seas. Laptev Sea inputs are initially high (262.5 cm) but decrease to average or below average, especially between 214.5-218.5 cm and 238.5-242.5 cm. These textural and provenance trends can be described as derived primarily from sea-ice IRD and localized inputs with intermittent flux of iceberg IRD. Given the location of JPC9 on the Mendeleev Ridge and the high potential for ice jamming along the Chukchi Borderland (Stein et al., 2010; Jakobsson et al., 2014), the Stage 6/5 transition may not be recorded in JPC9 as the movement of ice and melt-out rates might have been insufficient to induce a signature. Alternatively, this deglacial phase may be identified as part of the end Stage 6 period.

One rapid depositional event, R8 (119.0-122.3 ka; 210.5-238.5 cm), is identified within Substage 5e. This interval corresponds to the Glacial Stadial GS-26 (119.1 ka) (Rasmussen et al., 2014), implying a short glacial resurgence within the substage. This assertion is supported by the coarse textural signal identified within this rapid interval between 214.5-218.5 cm which may indicate a resurgence of iceberg IRD. While there is a decrease in foraminiferal abundance, the volume of ice associated with this event was not enough to prevent foraminiferal growth as moderate to high foraminiferal abundance is identified. The provenance of sediments through interval R8 indicates an initial influx from the East Siberian Sea with a cap of Kara Sea influx. North American sources are elevated, although not significantly. Mineralogy within this unit supports a glacial ice source, with elevated dolomite (222.5-226.5 cm; 119.9-120.2 ka). Therefore, it is proposed that during Substage 5e there was a short resurgence of ice sheet growth of the western LIS and possibly of the BKIS.

Substage 5d exhibits an overall sedimentation rate of 1.3 cm/kyr. This substage is associated with a period of slow deposition, S6 (111.2-115.7 ka; 194.5-198.5 cm) that may be related to the Greenland Interstadials GI-25b and GI-25c (spanning 111.4-115.7 ka; Rasmussen et al., 2014). Stage 5d should be considered a stadial, but the evidence from this unit suggests that this period is probably a cooler interstadial. There is evidence that the Substage 5d maxima is isolated to the latter portion of the substage interval. Moderately high foraminiferal abundance within S6 indicates conditions during this substage were ideal for planktonic foraminiferal growth within the central Arctic. The sediment textures are very fine initially, with an influx of very coarse sediment in the latter portion of the interval. This textural trend supports the notion of mild stadial conditions early within the unit that transition to more stadial like conditions in the latter portion. These stadial conditions differ from the full glacial periods in the sediment record, as the latter has conditions capable of producing hiatuses in sediment deposition. Sediment transport through this period was primarily via sea-ice, as indicated by the sediment provenance of Fe-oxides from sources not known to have been glaciated. There is a strong, short initial sediment signal originating from North American (eastern and western regions) and the Chukchi Sea that is replaced by influx from the Laptev and East Siberian Seas with very little input from the Kara Sea. This provenance trend indicates that, at the Mendeleev Ridge local sediment flux (e.g. sea-ice transport from the Laptev and East Siberian Seas) is dominant. Two major erosional events have been identified on the Chukchi Borderland and dated to Stage 4 and Substage 5d (Polyak et al., 2007; Stein et al., 2010). The origin of the ice has been proposed to be from floating ice masses from the LIS or from an East Siberian ice shelf (Jakobsson et al., 2014)). The latter source is supported by the East Siberian Sea provenance found in JPC9. Further support comes from the reported ice cover of Severnaya Zemlya from Substage 5d through Stage 4 based on the identification of glacial tills, indicating JPC9 was proximal to a major ice source in Substage 5d (Moller et al., 2006; Jakobsson et al., 2014).

Stein et al. (2010) identified a distinct carbonate (dolomitic) signal and interpreted this as MIS 5d. This dolomitic signal is not identified within Substage 5d based on this model. A dolomitic signal is identified within rapid interval R8 which is assigned to later Substage 5e. The placement of the dolomitic signal within substage 5e is intuitive as there is higher probability of sediment laden icebergs from the disintegrating Stage 6 terrestrial ice sheets. Regardless, if Stein et al. (2010) are correct, the dolomitic signal within R8 (222.5 to 226.5 cm) could be used as a Substage 5d age tie point for the age model. The model was not updated to incorporate this tie point as the model presented here is correlated to JPC8, which was constrained with modern dating techniques (Adler et al., 2009; Polyak et al., 2009). Using this dolomite signal as the MIS 5d tie point would result in a reduced duration of MIS 5e.

Substage 5c is coincident with an identified period of slow deposition, S5 (91.7-98.4 ka; 166.5-170.5 cm). Sediment lightness data from Substage 5c indicates a very brown interval. This brown color is typical of warmer Arctic environments. Very high foraminiferal abundance and texture supports the idea that this interval is ice free or restricted to first year ice, which is thin enough to allow for biologic productivity, as would be expected for a warm period. Initially, this interval experienced a very coarse signature with 7% >250 µm (3% > 1 mm), followed by a reduction in the coarse fraction to 2-4% >63 µm. This texture is somewhat indicative of a minor sea-ice IRD component. Sediment provenance further supports a warm interval with sea-ice sediment transport. The interval begins with a strong East Siberian Sea signal that is followed by North American and Laptev Sea signals. Aside from the North American signal, the primary source regions are known areas of only sea-ice production (Darby et al., 2011).

Substage 5b is bracketed by two depositional trends. The boundary between Substages 5b and 5a is marked by the slow deposition of S4, as described below. The beginning of the Substage 5b is marked by the rapid deposition of the 5c/5b transition, R7 (89.9-91.7 ka). R7 is related to the Greenland interstadial to stadial transition of GI-22e / GS-23.1 (89.8-90.1 ka). Foraminiferal content supports this transition, as the abundance is high Texture through R7 is very coarse, with a significant >250 um fraction (>8%) with a sizable >1 mm fraction. The texture is indicative of increasing iceberg sediment transport and delivery to the Mendeleev Ridge region. The provenance of Fe-oxides through this unit is interesting. Early in this unit, the primary sources are North America and the Laptev Sea. This suggests that the confluence of the TPD and BG was centered on the Mendeleev Ridge. The provenance then changes to the primary source being North America alone. Near the end of the unit, grains originating from the East Siberian and Kara Seas become more significant. This latter change could be the result of a constriction of the BG in response to atmospheric restructuring (e.g. Arctic Oscillation), and a broadening of the TPD source area, with significant eastward boundary current carrying sediment laden ice from the

Kara Sea towards Mendeleev Ridge (Rigor et al., 2002; Darby et al., 2012). This modification of the TPD and BG has been proposed previously, based on the sediment composition from the Fram Strait area (Phillips and Grantz, 2001). The constriction of the BG in response to environmental cooling is circumstantially supported by the short period following R7 that exhibits characteristics of a cooling climate.

Following R7, there is approximately 4 ka period of slightly above average sedimentation rates that is coincident with the peak of substage 5b and the transition to 5a, when the rates decline significantly. The texture of this interval of average sedimentation is initially 99.9 % < 45 um, followed by a return of coarse material at 146.5 cm. There is also a paucity of foraminifera through this short interval. This supports the possibility of an extremely cool period associated with the peak of Substage 5b with very little melt-out, followed by a return of iceberg rafted sediments as the climate rebounded toward interstadial conditions.

Substage 5a has a sedimentation rate of >4.5 cm/kyr. The interval begins with slow deposition, S4, spanning 134.5-142.5 cm (79.8-85.5 ka). This slow depositional period corresponds with Greenland interstadials GI-21.1d / GI-21.2 (79.9-85.1 ka) (Rasmussen et al., 2014). The sediment through S4 originates, in order, from the Kara and Laptev Seas, the East Siberian Sea, and the Chukchi Sea (**Figure 33**; **Table 13**). The texture within S4 is fine-grained (**Figure 32**). The provenance trend, coupled with the texture, implies an eastward flow of ice from the Kara Sea sea-ice with later onset of localized inputs from the East Siberian and Chukchi Seas. The planktonic foraminiferal abundance through S4 begins very low and increases to moderate to high concentrations. The implication of the foraminiferal abundance is that the sea-ice during this period was likely thin first year ice. Rates of deposition following S4 increase rapidly up through the MIS 5/4 transition.

Two rapid depositional events are identified within substage 5a, R6 and R5 (104.5-130.5 cm and 82.5-98.5 cm). These two rapid events that stand out in a period of enhanced sedimentation are probably related to growing terrestrial ice sheets based on textural characteristics. Event R6 does show early textural trends indicative of increased sea-ice entrainment. Both R6 and R5 exhibit punctuated increases in coarseness, with significant concentrations of >250 um fraction and >1 mm input. Both units exhibit influx of sediment from the Laptev and Chukchi Seas. R6 and R5 exhibit influx from North American and Kara Sea sources, respectively. The North American sources indicate that the Beaufort Gyre was active during this period. The later flux from the Kara Sea region implies direct eastward ice flow towards the Mendeleev Ridge. R6 and R5 contain very low foraminiferal preservation, therefore implying that thick multi-year sea-ice and/or glacial ice was forming an ice cap thick enough to prohibit foraminiferal growth. R6 corresponds with Greenland interstadials GI-20b / GI-21.1a (74.4-78.1 ka) (Rasmussen et al., 2014). Based on the timing, R6 appears to be a short warming period that occurred as the climate was cooling towards Stage 4.

5.5.4 MIS 4

Stage 4 exhibits fine texture and is mainly associated with the prolonged slow depositional period of S3. Overall the sedimentation rates through Stage 4 compare well with a conceptual ice sheet curve for the Svalbard-Barents Sea-ice sheet (Mangerud et al., 1998; Jakobsson et al., 2014). Much of Stage 4 is associated with elevated terrestrial ice volume as well as extensive perennial sea-ice cover. This interval of reduced sedimentation is probably attributable to these extensive ice sheet extensions and reduced melt-out during the strong stadial conditions of Stage 4. The sediment budget for JPC9 was probably like that of Stage 2 (Adler et al., 2009; Polyak et al., 2009; Poirier et al., 2012) and a more extreme version of late Stage 3 conditions (Cronin et al., 2012; Xaio et al., 2015), where thick extensive sea-ice pack prevented transport to, and melt-out of sediment laden ice. Erosional features are identified on the Chukchi margin, with the last erosional event sourced to the LIS and dated to the penultimate glaciation (MIS 4) based on cores from the Northwind Ridge (Polyak et al., 2007; Jakobsson et al., 2014). The presence of these erosional features implies the presence of a thick blockade of ice on the Chukchi Borderland that would prevent the movement of ice into the area of JPC9 on the Mendeleev Ridge. The result of this restricted ice movement coupled with lower water temperatures is slow rates of sediment deposition.

The prolonged period of S3 is preceded by rapid depositional event R5 which likely represents the rapid ice sheet extension associated with the Stage 5a/4 interstadial to stadial transition. The texture and provenance of the Fe-oxides within this unit is consistent with increased ice production in the primary ice sheet regions (e.g. North American and Eurasian ice sheets). The latter portion of this interval exhibits a strong Fe-oxide signal from both eastern and western North American sources (Ellef Ringnes and Banks Islands) and the eastern Laptev, Kara, and Barents Seas (**Figure 33**). This moderately ice-rich period associated with the Early Weichselian (Stage 5a-5d), was followed by a rapid increase in northern hemisphere ice volume (Mangerud et al., 1998; Svendsen et al., 2004; Jakobsson et al., 2014). Based on the JPC9 age model presented here, the advance of the LIS, IIS, and BKIS appears to be coeval through early Stage 4. The provenance of Fe-oxides from this rapidly deposited interval indicates that the circulation during early Stage 4 was like the present. The Beaufort Gyre circulation or similar would have had to been active for eastern North American sources to reach the Mendeleev Ridge. North American sediment signals are persistent in Mendeleev Ridge sediments through Stage 5; therefore, it is likely that the BG was persistent during this period.

5.5.5 MIS 3

Stage 3 is the coarsest unit identified within the JPC9 sediment record (10% >63 um), with the coarsest intervals restricted to middle and early Stage 3 periods. The textural trend identified through this unit is indicative of interstadial-like conditions with abundant iceberg-derived sediment deposition (Poirier et al., 2012). Two notable rapid excursions are identified at ca. 39.0-39.5 kya (R3) and ca. 42-44 kya (R4). Late Stage 3 consists of a period of extremely slow sediment deposition.

Prior to the Stage 2 hiatus and through the Stage 2/3 transition (23-38 kya), the sedimentation rate in JPC9 is very low. At the Stage 2/3 transition and well into late Stage 3, ca. 28 – 38 kya (28.5-30.5 cm), a period of very slow accumulation is identified in JPC 9 (possibly a hiatus). This period is associated with significant terrestrial ice sheet growth as the climate progresses into a full glacial period, and therefore would presumably result in increased sedimentation.

In the Mendeleev Ridge area, however, thick sea-ice with limited warm Atlantic water flux could result in decreased melt-out rates. Through this interval, very few Fe-oxide matches are from the eastern Arctic region (Kara and Laptev Seas) and may imply a weakened Atlantic flux to the western Arctic Ocean region (**Figure 33**). Couple the reduced warm Atlantic water reaching the Mendeleev Ridge with increased ice build-up along the Chukchi Borderland and increasingly thick sea-ice, and reduction in sediment melt-out can be envisioned. The foraminiferal abundance through this interval is higher than expected for increased sea-ice thickness but significantly decreases as the climate transitioned into Stage 2 (**Figure 30**). Sea-ice cover during late Stage 3 was more severe than the Holocene (Cronin et al., 2012; Xaio et al., 2015). Cronin et al., (2012) found a deeper halocline in the central Arctic relative to the present, related to a reduction in freshwater influx as a result of increased sea-ice cover, lower sea level, and smaller continental shelf areas during Stage 3. These authors also found that the abundance of an Arctic ostracode (*Acetabulastoma acrticum*) was elevated, indicative of cooler conditions. Variability in the sea-ice biomarker, IP_{25}, provides additional evidence that points to a cooler Stage 3 with increased sea-ice (Xiao et al., 2015). These authors found low or zero concentrations of phytoplankton biomarkers that indicates perennial and dense ice cover for the Mendeleev Ridge area during late Stage 3 (Xiao et al., 2015).

The timing of unit R3 is comparable to several previously identified events. The R3 unit is bracketed by Greenland Interstadial 8c and GS-9 (38.2-39.9 kya). This short-lived cooling event could explain a resurgence in ice sheet growth that could lead to increased sediment deposition. The rapid depositional interval is associated with a very coarse texture, with more than 10% of the sediment volume being coarser than 63 μm. This coarse signature would be indicative of increased ice sheet growth with increased ice calving and sediment transport. Additionally, the timing of this rapid event corresponds well with Heinrich event 4 (H4 – 38 kya; Hemming, 2004) and IRD event 7 (38.9 kya; Darby and

Zimmerman, 2008). The latter is associated with an ice sheet resurgence led by the IIS. This IIS lead is not recognized in JPC9, rather in JPC9 this event is associated with a sharp increase in sediments from Banks and Victoria Island and imply a LIS lead.

JPC9 rapid unit R4 has a finer texture, relative to R3, and is more indicative of a warmer period with extensive sea-ice transport and deposition. The timing of this event (42.6-44.2 kya) corresponds to a period bracketed by GS-11 and GI-11 (42.2 – 43.3 kya) and Heinrich Event 5 (H5) (Hemming, 2008; Rasmussen et al., 2014). This interval is associated with a sharp peak in lightness (*L) indicative of a brown interval (**Figure 35**). These brown intervals have been linked with variations in manganese, with the primary source attributed to extensive peat bogs and boreal forests of northern Siberia with further enhancement tied to bottom water ventilation changes during interglacial-glacial cycles (Jakobsson et al., 2000; Marz et al., 2012). The provenance of Fe-oxide grains within this unit in JPC9 conforms with the hypothesized source suggested by Jakobsson et al. (2000) and Marz et al. (2015). Fe-oxides grains from the R4 interval match initially to the Kara Sea area and are followed by increased flux from northern Siberian sources to the east (i.e. Laptev Sea then Chukchi Sea). The evidence of Siberian ice is established to have been present during Stage 4 on Severnaya Zemlya (Moller et al., 2006) as well as the northern Siberian coast (Alexanderson et al., 2001). Thus, as the environment transitioned into interstadial-type conditions, increased flux from the northern Siberian region under the right transport regime could reach the Mendeleev Ridge area and is a possible source for rapid depositional event R4. Distinct IRD maxima have been identified in Eurasian Basin sediment records which are recorded in the late MIS 4/early MIS 3 interval (65 to 50 kya; Speilhagen et al., 2004). These distinct IRD maxima are not identified in the JPC9 age model, rather the only identified IRD maxima in JPC9 is recorded as part of R4. Either these IRD maxima are missed in JPC9 either through poor sampling resolution or ice bypassing the JPC9 area or the model is shifted through this time period.

The R4 unit is preceded by a period of slow sediment deposition (S3; 46.4-69.5 kyr) that encompasses early Stage 3 and most of Stage 4. The start of this interval corresponds with GS-19.1 and GI-19.1 (69.4-

69.6 ka; Rasmussen et al., 2014). The lack of a coarse textural signature at the Stage 4/3 transition implies that this stadial to interstadial transitional signature was delayed. The sediment signal associated with the stadial to interstadial transition is likely found within rapid interval R4. The glaciation curve of the Svalbard-Barents Sea-ice sheet indicate that the bulk of the Stage 4 ice sheet disintegration occurred in early stage 3 (Mangerud et al., 1998; Jakobsson et al. 2014). Assuming this trend is true throughout the Arctic, which is probable for the cooler central Arctic, then the R4 sedimentation event probably does represent the Stage 4 deglacial sediment signal. As previously mentioned, the primary source of R4 sediments is from the Kara Sea region with increasing influx of northern Siberian sources.

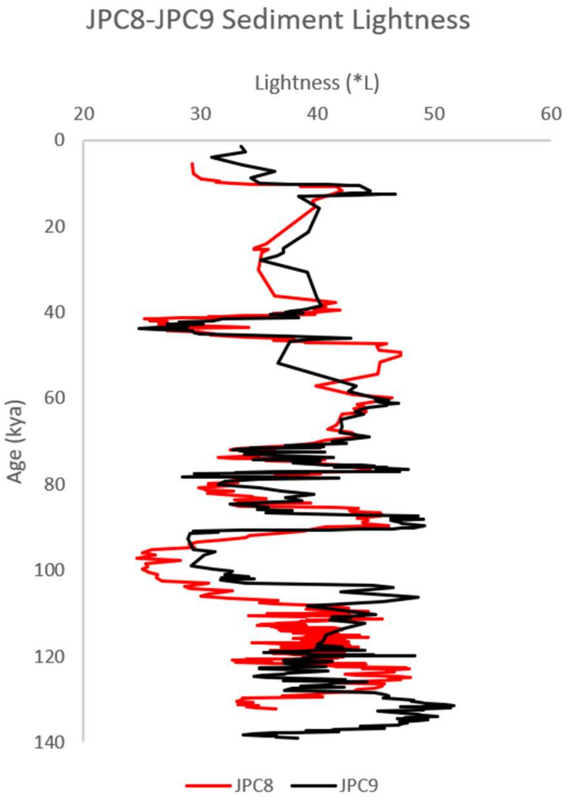

Figure 35. Comparison of sediment lightness of JPC8 and JPC9 plotted against age. The slight difference between the two curves is a result of the JPC9 age model refinement based on the correlation to JPC22.

Two distinct pink-white layers are associated with Stage 3 sediments, one at the Stage 4/3 boundary and the other at ca. 40 ka (Polyak et al., 2004, 2009; Stein et al., 2010). While the pink-white layer at ca. 40 ka is recognized in JPC9 through increased dolomitic content and is bracketed by R3 and R4, the pink-white layer associated with the Stage 4/3 transition is not identified. This peak in dolomite tied to the Stage 4/3 transition may have been missed in the sampling of JPC9. If this pink-white layer was especially rapid, the sampling resolution of JPC9 (~2 cm) may have missed a major IRD event. There is a pink-white layer attributed to early Stage 4/late stage 5. Since this record was initially tuned to the JPC8 record of Polyak et al. (2009), it is unlikely that a large age model shift occurred. The most likely reason for this missing pink-white layer is that it was a short-lived event and was subsequently missed during sampling.

5.5.6 MIS 2

Much of the Stage 2 interval appears to be missing indicating a period of non-deposition (hiatus), as has been previously described for other central Arctic sediment records (Adler et al., 2009; Polyak et al., 2009; Poirier et al., 2012). In JPC9 this hiatus covers the interval between 22.5-24.5 cm and corresponds to 13.8-23.6 ka. This hiatus of ca. 10 kyr corresponds well to the hiatus of several thousand years between 15-23 ka identified in nearby core JPC8 (Adler et al., 2009; Polyak et al., 2009). The longer duration hiatus identified in JPC9 may be related to limited sampling resolution and poor constraints on the beginning and end of the hiatus.

The reason for this hiatus during Stage 2 is not fully understood but may be related to winnowing processes (Poore et al., 1999) or the presence of extensive thick ice cover and strongly reduced sediment deposition (Adler et al., 2009; Polyak et al., 2009). Like JPC8, the lack of definitive coarse lag deposits implies that winnowing is an unlikely source of this hiatus (Polyak et al. 2009).

5.5.7 Holocene/MIS 1

The lack of a sharp defined coarse signature during the MIS 2/1 transition is anomalous. Melt-out rates along the Mendeleev Ridge (JPC9 core site) may have been insufficient during the Stage 2/1 transition to produce a rapidly deposited coarse-textural signature, or the duration of an event was too short for the sampling frequency through this interval to identify such a textural excursion. Despite the lack of a coarse texture signal, two prominent rapid sedimentation intervals are identified (R1 and R2). These rapid events indicate that the environment during the transition from Stage 2 to 1 was not a continuous or smooth transition, but rather implies a deglaciation marked by pulses of calving glacial ice. Although rapidly deposited, events R1 and R2 appear to be quite fine in texture. Very few Fe-oxide sediment grains were available for provenance determination via Fe-oxide fingerprinting, but those that were indicate a North American source for at least the coarse sediment. The fine fraction from these two events exhibit dolomite (North American) and smectite (Kara and Laptev Seas) signatures that are moderately elevated above the core mean. This mineral signal is indicative of co-varying North American and Eurasian source inputs.

A rapid depositional event (R1) is identified between 8.5 and 10.5 cm and, based on the interpolated JPC9 age model, corresponds to a period of less than 100 years at approximately 10.3 ka. This is beyond the estimated resolution or error of the age model, conservatively 1000 years, and is thus considered instantaneous. R1 is likely related to either the 9.3 ka cooling event (Rasmussen et al., 2014) or it is related to a secondary deglacial pulse from the ice sheet collapse associated with Termination I. Darby & Zimmerman (2008), identified several ice-rafted detritus (IRD) layers in various Arctic Ocean sediment cores. R1 corresponds with IRD event 1 (ca. 10 kya) which was found to exhibit a simultaneous sediment flux from the Laurentide and Innuitian Ice Sheets (LIS and IIS; Darby and Zimmerman, 2008). Again, the Fe-oxide matches for this interval are low in JPC9 but do imply a roughly simultaneous flux with source areas 4 (IIS) and 8 (LIS) peaking at the same time.

A second rapid sedimentation event is identified between 11.7 and 12.6 ka (R2). This timing of this event is related to Greenland Stadial 1 (GS) (Younger Dryas cooling event) as identified in the NGRIP Greenland Ice Core record (Rasmussen et al., 2014). This event also corresponds the previously identified Heinrich Event 0 (H0; ca. 11 ka) and Arctic Laurentide event 1 (AL1; 12.9 kya) (**Table 12**;

Darby et al., 2002). In JPC9, rapid sedimentation event R2 shows a strong North American signal with a subequal flux from the Chukchi Sea region. The interval is capped by a Kara Sea signal which implies that the LIS leads the Barents-Kara Ice Sheet (BKIS) sediment flux to JPC9. The identification of this event, coupled with the JPC9 age model, increases our understanding of deglacial conditions during Termination I. Prior to R2, an interval of very slow deposition is recognized that encompasses Stage 2 and late Stage 3.

5.5.8 Age Model Approach

In this study, the age model of a central Arctic Ocean sediment record is refined to the oxygen-isotope stratigraphy of a core from Fram Strait using unique mineralogical signals. While the approach is not perfect, it is simple and effective. Even with an estimated error of approximately 500 years per centimeter of sediment, rapid depositional events were identified. If this approach can be further refined, the potential for deepening our understanding of central Arctic stratigraphy is great. Additional investigation of the use of TPD and BG signals as a correlative tool may reduce the need for intermediary core correlations. For instance, the current need for Lomonosov Ridge cores for age model transfers from the eastern and western Arctic Ocean basins.

The major restriction to this approach is the need for a framework on which to build and refine the model. In this study, the framework of ages from JPC8 was decently established utilizing multiple age dating methods providing abundant ages across a comprehensive depth range covering the late Quaternary. Further refinement of the approach utilizing the TPD and BG signals and linkage to GI and GS events (e.g. DO cycles) may lead to a more robust proxy of central Arctic variations in these signals. If this TPD/BG proxy signal is further defined and found to be ubiquitous throughout the central Arctic, the need for an age model framework may not be required.

5.6 Conclusions

Periods of rapid and slow deposition are identified in the Central Arctic. These rapid and slow depositional events appear to correspond to stadial and interstadial events associated with DO cycles. If these events can be further shown to correspond to DO cycles, then they potentially represent key chronostratigraphic tie points for oxygen-isotope stratigraphy in the central Arctic Ocean.

Fe-Oxide matches provide evidence that the current surface circulation in the Arctic has been active throughout most of the late Quaternary. Some variation is identified, indicating some modulation that may include constriction/loosening of the BG and increasing/decreasing swath of the TPD. These changes are in response to environmental changes possibly linked to climatic variations. Tighter age control is still required to confirm this assertion. The mineralogical provenance data corresponds nicely with the Fe-Grain matches to sources. Because these Fe-grain matches are more precise than mineralogical provenance, the correspondence between the two independent methods shows that the mineralogic provenance as defined here is a viable approach to determining sources.

This work shows that an age model can successfully be transferred from a core in the eastern Arctic basin to the western basin. The current procedure does require an age model framework on which to build. As the knowledge of stratigraphy increases the need for such a framework will diminish. Additional work is required to refine the basin-wide characteristics of the sedimentation events used in this correlation.

6 SUMMARY

Several findings stem from this work that contribute to Arctic paleoceanography. One important result was the identification of a smectite source in North America, from a region that significantly contributes to the Arctic sediment budget during glacial and interglacial periods. This North American smectite signal calls into question previously published interpretations that attribute the presence of smectite to solely Eurasian sources (e.g., Vogt and Knies, 2008). Further, the speciation, or type, of smectite shows promise as a means of distinguishing Eurasian and North American source contributions of smectite. Several minerals are identified as potentially useful for determining provenance under certain conditions where these minerals are more than trace amounts. More research is required to fully understand this potential. Increased sampling density and distribution of circum-Arctic sources, especially in the North American region, and perhaps an improved mineral quantification method would be the logical first steps in attempting to constrain these circum-Arctic mineral characteristics.

Global oxygen-isotope stratigraphy was successfully transferred via a paleomagnetic proxy to core JPC22 located on the Yermak Plateau in Fram Strait. This stratigraphy was then used to refine a central Arctic age model, JPC9. Effectively applying oxygen-isotope stratigraphy by proxy to the central Arctic. The importance of these two models lies in the identification of variations in sedimentation rates. These sedimentation ‘events’ provide new insights to the history of the Arctic Ocean ice-rafting. Many of these ‘events’ appear to be contemporaneous to known major ice-rafting episodes. The identification and characterization of these ice-rafting events should be attempted for various regions within the Arctic to see if these events represent basin-wide ice-rafting events. The characterization of these horizons will be key in their eventual (potential) use in chronostratigraphic investigations. The contributions of source areas for these sedimentation events such as glacial discharge events and large sea-ice entrainment events. Increased core resolution would also be helpful in deconstructing glacial-related events (e.g. deglacials).

REFERENCES

Aagaard, K., and E. C. Carmack (1989) The role of sea-ice and other fresh water in the Arctic Mediterranean seas. *Journal of Geophysical Research,* 94(C10), 14485-14498.

Aagaard, K., D. Darby, K. Falkner, G. Flato, J. Grebmeier, C. Measures, and J. Walsh (1997) Marine Science in the Arctic: A strategy, Arctic Research Consortium of the United States (ARCUS), Fairbanks, AK, 84 pp.

ACIA (2004) Impacts of a Warming Arctic: Arctic Climate Impact Assessment. Cambridge University Press.

Adler, R.E., L. Polyak, J.D. Ortiz, D.S. Kaufman, J.E.T. Channell, C. Xuan, A.G. Grottoli, E. Sellen, and K.A. Crawford (2009) Sediment record from the western Arctic Ocean with an improved Late Quaternary age resolution: HOTRAX core HLY0503-JPC8, Mendeleev Ridge. *Global and Planetary Change,* doi: 10.1016/j.gloplacha.2009.03.026

Aksenov, Y., Karcher, M., Proshutinsky, A., Gerdes, R., de Cueves, B., Golubeva, E., Kauker, F., Nguyen, A.T., Platov, G.A., Wadley, M., Watanabe, E., Coward, A.C., and George Nurser, A.J. (2016) Arctic Pathways of Pacific Water: Arctic Ocean Model Intercomparison experiments. *Journal of Geophysical Research: Oceans,* 121, 27-59, doi: 10.1002/2015JC011299

Aldahan, A., G. Possnert, R. Scherer, N. Shi, J. Backman, and K. Bostrom (2000) Trace-element and major-element stratigraphy in Quaternary sediments from the Arctic Ocean and implications for glacial termination. *Journal of Sedimentary Research, 70, 5,* 1095-1106

Alexandrov, V.Y., Martin, T., Kolatschek, J., Eicken, H., Kreyscher, M., Makshtas, A.P. (2000) Sea-ice circulation in the Laptev Sea and ice export to the Arctic Ocean: Results from satellite remote sensing and numerical modeling. *Journal of Geophysical Research,* 105, C7, 17143-17159

Alexanderson, H., J. Backman, T.M. Cronin, S. Funder, Ó. Ingólfsson, M. Jakobsson, J.Y. Landvik, L. Löwemark, J. Mangerud, C. März, P. Möller, M. O'Regan, and R.F. Spielhagen (2014) An Arctic perspective on dating Mid-Late Pleistocene environmental history. *Quaternary Science Reviews,* 92, 9-31

Alexanderson, H., C. Hjort, P. Moller, O. Antonov, M. Pavlov (2001) The North Taymyr ice-marginal zone, Arctic Siberia – a preliminary overview and dating, *Global Planetary Change,* 31, 427-445.

Alexandrov, V.Y., Martin, T., Kolatschek, J., Eicken, H., Kreyscher, M., Makshtas, A.P. (2000) Sea-ice circulation in the Laptev Sea and ice export to the Arctic Ocean: Results from satellite remote sensing and numerical modeling. *Journal of Geophysical Research,* 105, C7, 17143-17159

Alley, R.B. (1995) Resolved: The Arctic Controls Global Climate Change. *Coastal and Estuarine Studies,* 49, 263-283

Amante, C. and B.W. Eakins (2009) ETOPO1 1 Arc-Minute Global Relief Model: Procedures, Data Sources and Analysis. NOAA Technical Memorandum NESDIS NGDC-24. National Geophysical Data Center, NOAA. doi:10.7289/V5C8276M [September 27, 2015]

Andrews, J.T. and Principato, S.M (2002) Grain-Size characteristics and provenance of ice-proximal glacial marine sediments. In: Dowdeswell, J.A. and Ó Cofaigh, C. (eds.) Glacier-Influenced

Sedimentation on High-Latitude Continental Margins. Geological Society, London, Special Publications, 203, 305-324

Andrews, J.T., Geirsdottir, A., Jennings, A.E. (1989) Spatial and temporal variations in clay- and silt-size mineralogy of shelf and fjord cores, Baffin Island. *Continental Shelf Research,* 9, 445-463

Backman J, M. Jakobsson, R. Løvlie, L. Polyak, L.A. Febo (2004) Is the central Arctic Ocean a sediment starved basin? *Quaternary Science Reviews*, 23:1435-1454

Bazhenova, E.A. (2012) Reconstruction of late Quaternary sedimentary environments at the southern Mendeleev Ridge (Arctic Ocean). dissertation, Unversity of Bremen.

Bazhenova, E.A., Fagel, N., Stein, R. (submitted) Origin of late Quaternary 'pink-white' layers at the Mendeleev Ridge (Arctic Ocean): New insights from lead and neodymium isotope composition of detrital sediment component. *Geochimica et Cosmochimica Acta.*

Behrends, M., Peregovich, B., and Stein, R. (1996) Terrigenous sediment supply into the Arctic Ocean: Heavy mineral distribution in the Laptev Sea. In: Surface-sediment composition and sedimentary processes in the Central Arctic Ocean and along the Eurasian Continental Margin, R. Stein, G. Ivanov, M. Levitan and K. Fahl (eds.), *Reports on Polar Research,* 212, 37-42.

Behrends, M., Hoops, E., Peregovich, B. (1999) Distribution patterns of heavy minerals in Siberian rivers, the Laptev Sea and the eastern Arctic Ocean: an approach to identify sources, transport and pathways of terrigenous matter. In: Kassens, H., Bauch, H.A., Dmitrenko, I., Eicken, H., Hubberten, H.-W., Melles, M., Thiede, J., Timokhov, L. (Eds.), Land–Ocean Systems in the Siberian Arctic: Dynamics and History. Springer, Berlin, pp. 265–286.

Bischof J.A. & D.A. Darby (1997) Mid- to Late Pleistocene ice drift in the western Arctic Ocean: Evidence for a different circulation in the past. *Science*, 277, 74-78.

Bischof, J., D.L. Clark, and J-S. Vincent (1996) Origin of ice-rafted debris: Pleistocene paleoceanography in the western Arctic Ocean. *Paleoceanography*, 11, 6, 743-756.

Biscaye, P.E. (1965) Mineralogy and sedimentation of recent deep-sea clays in the Atlantic Ocean and adjacent seas and oceans. *Geological Society of America Bulletin, 76,* 803-832

Bogen, J. and Bønsnes, 2003, Erosion and sediment transport in high arctic rivers, Svalbard, *Polar Research*, v. 22, p. 175-189.

Bond, G.C. and R. Lotti (1995) Iceberg discharges into the North Atlantic on millennial time scales during the last glaciation. *Science,* 267, 1005-1010. doi:10.1126/science.267.5200.1005

Bond GC, Showers W, Cheseby M, Lotti R, Almasi P, deMenocal P, Priore P, Cullen H, Hajdas I, Bonani G (1997) A pervasive millennial-scale cycle in North Atlantic Holocene and glacial climates. Science, 278:1257-1266

Brigham-Grette, J., D.M Hopkins, V.F. Ivanov, A.E. Basilyan, S.L. Benson, P.A. Heiser, and V.S. Pushkar (2001) Last Interglacial (isotope Stage 5) glacial and sea-level history of coastal Chukotka Peninsula and St. Lawrence Island, Western Beringia. *Quaternary Science Reviews*, 20, 419-436.

Chamley, H. (1989) Clay Sedimentology, Springer Verlag, Berlin, 623 pp.

Channell, J.E.T. and Xuan, C. (2009) Self-reversal and apparent magnetic excursions in Arctic sediments. *Earth and Planet. Lett.* 284, 124-131

Christie, R.L. (1964) Geology of Northeastern Ellesmere Island. G.S.C. Memoir 331

Clark, D.L. (1970) Magnetic reversals and sedimentation rates in the Arctic Basin. *Geological Society of America Bulletin,* 81, 3129-3134.

Clark, D.L, Whitman, R.R., Morgan, K.A., and S.D. Mackey (1980) Stratigraphy and glacial-marine sediments of the Amerasian basin, central Arctic Ocean. *Geoloical Society of America Special Paper,* 181, 1-57.

Colleoni, F., Kirchner, N., Niessen, F., Quiquet, A., and Liakka, J. (2013) An east Siberian ice shelf during the late Pleistocene glaciations: numerical reconstructions. *Quaternary Science Reviews.* 147, 148-163.

Comiso, J.C., C.L. Parkinson, R. Gersten, and L. Stock (2008) Accelerated decline in Arctic sea-ice cover. *Geophysical Research Letters,* 35, 1, DOI: 10.1029/2007GL031972

Comiso, J.C. (2012) Large decadal decline of the Arctic multiyear ice cover. J. Clim., 25, 1176-1193.

Council, E. (2012) *Central Arctic lithostratigraphy: Implication on sediment transport and paleoceanograpghy.* (unpublished doctoral dissertation) Wright State University, Dayton, Ohio.

Couture, R.A. (1977) Composition and origin of palygorskite-rich and montmorillonite-rich zeolite-containing sediments from the Pacific Ocean. *Chemical Geology,* 19(1-4), 113-130.

Cronin, T.M., G.S. Dwyer, J. Farmer, H.A. Bauch, R.F. Spielhagen, M. Jakobsson, J. Nilsson, W.M. Briggs Jr., and A. Stepanova (2012), Deep Arctic Ocean warming during the last glacial cycle. *Nature Geoscience.,* 5, 631-634. doi: 10.1038/ngeo1557.

Cronin TM, Polyak L, Reed D, Kandiano ES, Marzen, RE, Council EA (2013) A 600-ka Arctic sea-ice record from Mendeleev Ridge based on ostracodes. Quat Sci Rev. http://dx.doi.org/10.1016/j.quascirev.2012.12.010

Darby, D. A. (1975) Kaolinite and other clay minerals in Arctic Ocean sediments, *Journal of Sedimentary Petrology, 45,* 272-279

Darby, D. A. (2003), Sources of sediment found in sea-ice from the western Arctic: New insights into processes of entrainment and drift patterns, *Journal of Geophysical Research, 108* (C8), 3257, doi: 10.1029/2002JC001350

Darby, D. A. (2008), Arctic perennial ice cover over the last 14 million years. *Paleoceanography*, *23*, PA1S07, doi:10.1029/2007PA001479

Darby, D.A. and J.F. Bischof (1996) A statistical approach to source determination of lithic and Fe-oxide grains: an example from the Alpha Ridge, Arctic Ocean. *Journal of Sedimentary Research*, 66, 599-607

Darby D.A. and J. Bischof (2004) A Holocene record of changing Arctic Ocean ice drift, analogous to the effects of the Arctic Oscillation. *Paleoceanography*, 19, PA1027, doi: 10.1029/2003PA000961

Darby, D.A. and P. Zimmerman (2008), Ice-rafted detritus events in the Arctic during the last glacial interval and the timing of the Innuitian and Laurentide ice sheet calving events. *Polar Research,* 27, 114-127

Darby, D. A., S. A. Naidu, T. C. Mowatt, and G. A. Jones (1989), Sediment composition and sedimentary processes in the Arctic Ocean, in *The Arctic Seas: Climatology, Oceanography, Geology, and Biology,* edited by Y. Herman, pp. 657-720, Van Nostrand Reinhold, New York.

Darby, D.A., J. F. Bischof, R. F. Spielhagen, S. A. Marshall, and S. W. Herman (2002), Arctic ice export events and their potential impact on global climate during the late Pleistocene. *Paleoceanography, 15, 1-17,* doi:10.1029/2001PA000639

Darby, D. A., M. Jakobsson, and L. Polyak (2005), Icebreaker Expedition Collects Key Arctic Seafloor and Ice Data, Eos Trans. AGU, 86(52), doi:10.1029/2005EO520001.

Darby D.A., L. Polyak, M. Jakobsson, G. Berger, R. Lövlie, D. Perovich, T. Grenfell, T. Kikuchi, and K. Tateyama (2006) HLY0503 Cruise Report. http://sci.odu.edu/oceanography/research/hotrax/leg2/HYL0503_cruise_rpt.pdf

Darby DA Polyak L, Bauch H (2006b) Past glacial and interglacial conditions in the Arctic Ocean and marginal seas, a review. In: Structure and function of contemporary food webs on Arctic shelves: a Pan-Arctic comparison, P. Wassman, (ed.). Progr. Oceanography 71:129-144.

Darby, D., Ortiz, J., Polyak, L., Lund, S., Jakobsson, M., and Woodgate, R., (2009a) The role of currents and sea-ice in both slowly deposited central Arctic and rapidly deposited Chukchi–Alaskan margin sediments, *Global Planetary Change*, doi:10.1016/j.gloplacha.2009.02.007.

Darby D.A., L. Polyak, and M. Jakobsson (2009b) The 2005 HOTRAX expedition to the Arctic Ocean. *Global and Planetary Change*, 68, 1e4

Darby D.A., W.B. Myers, M. Jakobsson, and I. Rigor (2011) Modern dirty sea-ice characteristics and sources: The role of anchor ice. *Journal of Geophysical Research*, doi: 10.1029/2010JC006675

Darby, D.A., J.D. Ortiz, C.E. Grosch, and S.P. Lund (2012), 1,500-year cycle in Arctic Oscillation identified in Holocene Arctic sea-ice drift, *Nature Geoscience.* doi: 10.1038/NGEO1629

Darby D.A., Myers W., Herman S., and B. Nicholson (2015) Chemical fingerprinting, a precise and efficient method to determine sediment sources. *J. of Sed. Res.* 85, 247-253, doi: http://dx.doi.org/10.2110/jsr.2015.17

Deer, W.A., Howie, R.A., Zussman, J., (2001) Rock Forming Minerals: Volume 4A, Framwork Silicates: Feldspars, *The Geological Society.* London. 973 pp.

Dove, D., Polyak, L., Coakley, B., (2014) Widespread, multi-source glacial erosion on the Chukchi margin, Arctic Ocean. *Quat. Sci. Rev.* 92, 112-122.

Dowdeswell, J.A., Jakobsson, M., Hogan, K.A., O'Regan, M., Backman, J., Evans, J., Hell, B., Löwemark, L., Marcussen, C., Noormets, R., Cofaigh, C.Ó., Sellén, E., Sölvsten, M. (2010) High-resolution geophysical observations of the Yermak Plateau and northern Svalbard margin: implications for ice-sheet grounding and deep-keeled icebergs. *Quaternary Science Reviews*, 29, 3518-3531.

Drewry, D. (1986) Glacial Geologic Processes. Edward Arnold, London, 276 pp.

Eakins, B.W. and G.F. Sharman (2010) Volumes of the World's Oceans from ETOPO1, NOAA National Geophysical Data Center, Boulder, CO

Eberl, D. D. (2003), User guide to RockJock—A program for determining quantitative mineralogy from X-ray diffraction data. Revised 2009. U.S. Geological Survey Open-File Report, OF 03-78, 56 p. (RockJock version 10)

Eberl, D. D. (2004) Quantitative mineralogy of the Yukon River system: Changes with reach and season and determining sediment provenance. *American Mineralogist, 89*, 1784-1794

Eicken, H., R. Gradinger, A. Gaylord, A. Mahoney, I. Rigor, and H. Melling (2005) Sediment transport by sea-ice in the Chukchi and Beaufort Seas: Increasing importance due to changing ice conditions? *Deep Sea Research Part II: Topical Studies in Oceanography,* 52, 24-26, 3281-3302.

Ernst, R.E., Hamilton, M.A., Söderlund, U., Hanes, J.A., Gladkochub, D.P., Okrugin, A.V., Kolotilina, T., Mekhonoshin, A.S., Bleeker, W., LeCheminant, A.N., Buchan, K.L., Chamberlain, K.R., Didenko, A.N. (2016) Long-lived connection between southern Siberia and northern Laurentia in the Proterozoic. *Nature Geoscience*, doi: 10.1038/ngeo2700.

Gamboa, A., Montero-Serrano, J.-C., St-Onge, G., Rochon, A., Desiage, P.-A., (2017) Mineralogical, geochemical, and magnetic signatures of surface sediments from the Canadian Beaufort Shelf and Amundsen Gulf (Canadian Arctic). *Geochemistry, Geophysics, Geosystems,* 18, 2, 488-512, doi: 10.1002/2016GC006477.

Gibbs, R.J. (1965) Error due to segregation in quantitative clay mineral X-ray diffraction mounting techniques. *American Mineralogy,* 50(10), 741-751.

Gordeev, V.V. (2006) Fluvial seidiment flux to the Arctic Ocean. *Geomorphology*, 80, 94-104.

Grosswald, M.G. and T.J. Hughes (1999) The case for an ice shelf in the Pleistocene Arctic Ocean. *Polar Geography,* 23, 1, 23-54.

Hemming, S.R., (2004) Heinrich events: Massive late Pleistocene detritus layers of the North Atlantic and their global climate imprint. *Reviews of Geophysics,* 42, 1, doi: 10.1029/2003RG000128

Hevrøy, K., Lavik, G., and Jansen, E. (1996) Quaternary Paleoceanography and Paleoclimatology of the Fram Strait, *Yermak Plateau Region: Evidence from Sites 909 and 912,* Thiede, J., Myhre, A.M., Firth, J.V., Johnson, G.L., and Ruddiman, W.F. (Eds.) Proceedings of the Ocean Drilling Program: Scientific Results, 151, pp 469-482.

Hu, A., Meehl, G.A., Han, W., Timmermann, A., Otto-Bliesner, B., Liu, Z., Washington, W.M., Large, W., Abe-Ouchi, A., Kimoto, M., Lambeck, K., Wu, B., (2012) Role of the Bering Strait on the hysteresis of the ocean conveyor belt circulation and glacial climate stability. *Proc. Natl. Acad. Sci.* 109, 6417-6422.

IPCC, 2013: *Climate Change 2013: The Physical Science Basis. Contribution of Working Group I to the Fifth Assessment Report of the Intergovernmental Panel on Climate Change* [Stocker TF, Qin D, Plattner G-K, Tignor M, Allen SK, Boschung J, Nauels A, Xia Y, Bex V, Midgley PM (eds.)]. Cambridge University Press, Cambridge, United Kingdom and New York, NY, USA, 1535 pp, doi: 10.1017/CBO9781107415324.

Jakobsson M, Løvlie R, Al-Hanbali H, Arnold E, Backman J, Mörth M (2000) Manganese and color cycles in Arctic Ocean sediments constrain Pleistocene chronology. Geology, 28:23-26

Jakobsson M., R. Løvlie, E.M. Arnold, J. Backman, L. Polyak, J-O. Knutsen, and E. Musatov (2001) Pleistocene stratigraphy and paleoenvironmental variation from Lomonosov Ridge sediments, central Arctic Ocean. *Global and Planetary Change,* 31, 1-22

Jakobsson, M., J. Backman, A. Murray, and R. Løvlie (2003) Optically Stimulated Luminescence dating supports Central Arctic Ocean cm-scale sedimentation rates. *Geochemistry, Geophysics, Geosystems.* 4, 1016, doi:10.1029/2002GC000423.

Jakobsson M., L. Polyak, M. Edwards, J. Kleman, B. Coakley (2008) Glacial geomorphology of the central Arctic Ocean: the Chukchi Borderland and the Lomonosov Ridge. *Earth Surf Process Landf,* 33, 526-545.

Jakobsson M, et al. (2012) The International Bathymetric Chart of the Arctic Ocean (IBCAO) Version 3.0. *Geophysical Research Letters*, doi: 10.1029/2012GL052219.

Jakobsson M, et al. (2013) Arctic Ocean glacial history. *Quaternary Science Reviews,* 92, 40-67.

Jakobsson M., J. Nilsson, L. Anderson, J. Backman, G. Björk, T.M. Cronin, N. Kirchner, A. Koshurnikov, L. Mayer, R. Noormets, M. O'Regan, C. Stranne, R. Ananiev, N. Barrientos Macho, D. Cherniykh, H. Coxall, B. Eriksson, T. Flodén, L. Gemery, Ö. Gustafsson, K. Jerram, C. Johansson, A. Khortov, R. Mohammad, and I. Semiletov (2016) Evidence for an ice shelf covering the central Arctic Ocean during the penultimate glaciation. *Nature Communications,* doi: 10.1038/ncomms10365

Jones, E.P. (2001) Circulation in the Arctic Ocean. *Polar Research,* 20(2), 139-146

Kalinenko, V.V., E.S. Shelekhova, and M. Wahsner (1996), Clay minerals in surface sediments of the East Siberian and Laptev Seas. In Stein et al. (Eds.) Surface-sediment composition and sedimentary processes in the central Arctic Ocean and along the Eurasian continental margin. *Polarforschung*, 212, 43-50.

Kaparulina, E., Strand, K., and Lunkka, J.P. (2016) Provenance analysis of central Actic Ocean sediments: Implications for circum-Arctic ice sheet dynamics and ocean circulations during Late Pleistocene. *Quaternary Science Reviews, 147, 210-220. doi: https://doi.org/10.1016/j.quascirev.2015.09.017*

Kaufman D, L. Polyak, R. Adler, J. Channell, and C. Xuan (2008) Dating late Quaternary planktonic foraminifer Neogloboquadrina pachyderma from the Arctic Ocean by using amino acid racemization. *Paleoceanography*, 23: PA3224.

Kempama, E.W., E. Reimnitz, and P.W. Barnes (1989) Sea-ice sediment entrainment and rafting in the Arctic. *Journal of Sedimentary Research,* 59, 2, 308-317

Kleman J, Jansson K, De Angelis H, Stroeven AP, Hättestrand C, Alm G, Glasser N (2010) North American Ice Sheet build-up during the last glacial cycle, 115-21 kyr. Quat. Sci Rev. 29:2036-2051

Knies, J. and Stein, R., (1998) New aspects of organic carbon despostion and paleoceanographic implications along the northern Barents Sea margin during the last 30,000 years. *Paleoceanography,* 13, 384-394.

Knies J, Vogt C (2003) Freshwater pulses in the eastern Arctic Ocean during Saalian and Early Weichselian ice-sheet collapse. Quat. Res. 60: 243-251

Knies J, Vogt C, Stein R (1999) Late Quaternary growth and decay of the Svalbard/Barents Sea-ice sheet and paleoceanographic evolution in the adjacent Arctic Ocean. Geo-Mar. Lett 18:195-202.

Knies, J., Muller, C., Nowaczyk, N., Vogt, C. and Stein, R. (2000) A multiproxy approach to reconstruct the environmental changes along the Eurasian continental margin over the last 150 kyr. *Marine Geology,* 163, 317-344.

Knies J, Kleiber HP, Matthiessen J, Müller C, Nowaczyk N (2001) Marine ice-rafted debris records constrain maximum extent of Saalian and Weichselian ice-sheets along the northern Eurasian margin. Global Planet. Change 31:45-64

Knies J, Matthiessen J, Mackensen A, Stein R, Vogt C, Frederichs T, Nam, S-I (2007) Effects of Arctic freshwater forcing on thermohaline circulation during the Pleistocene. Geology 35:1075-1078

Knies, J. D. Koseoglu, L. Rise, N. Baeten, V.K. Bellec, R. Boe, M. Klug, G. Panieri, P.E. Jernas, and S.T. Belt (2018) Nordic Seas polynyas and their role in preconditioning marine productivity during the Last Glacial Maximum. *Nature Communications*. 9, 3859.

Krylov, A.A., Andreeva, I.A., Vogt, C., Backman, J., Krupskaya, V.V., Grikurov, G.E., Moran, K., Shoji, H. (2008) A shift in heavy and clay mineral provenance indicates a middle Miocene onset of a perennial sea-ice cover in the Arctic Ocean. *Paleoceanography,* 23, PA1S06, doi: 10.1029/2007PA001497

Knoll and Swett (1990) Carbonate deposition during the Late Proterozoic Era – An example from Spitsbergen. *American Journal of Science,* 290A, 104-132

Lang N and Wolff EW (2011) Interglacial and glacial variability from the last 800 ka in marine, ice and terrestrial archives. Clim. Past 7:361-380

Levitan M.A., and R. Stein (2008) History of sedimentation rates in the glacial zone of sedimentation during the last 130 ka. *Lithology and Mineral Resources,* 1:74-86 (in Russian)

Levitan M.A. and Y.A. Lavrushin (2009) Sedimentation History in the Arctic Ocean and Subarctic Seas for the Last 130 kyr. Springer-Verlag Berlin Heidelberg

Levitan, M.A., Dekov, V.M., Gorbunova, Z.N., Gurvich, E.G., Muyakshin, S.I., Nürnberg, D., Pavlidis, M.A., Ruskova, N.P., Shelekova, E.S., Vasilkov, A.V., Wahsner, M. (1996) The Kara Sea: a reflection of modern environment in grain size, mineralogy, and chemical composition of the surface layer of bottom sediments. In. Stein, R., Ivanov, G.I., Levitan, M.A., and Fahl, K. (eds.) Surface sediment composition and sedimentary processes in the central Arctic Ocean and along the Eurasian continental margin. *Ber. Polarforschung,* 212, 58-80.

Lightfoot, P.C. & Hawkesworth, C.J. (1997) Flood Basalts and Magmatic Ni, Cu, and PGE Sulphide Mineralization: Comparative Geochemistry of the Noril'sk (Siberian Traps) and West Greenland Sequences, in Large Igneous Provinces: Continential, Oceanic, and Planetary Flood Volcanism (eds J.J. Mahoney and M.F. Coffin), American Geophysical Union, Washington D.C., doi: 10.1029/GM100p0357.

Lind, S. & Ingvaldsen, R.B. (2012) Variability and impacts of Atlantic Water entering the Barents Sea from the North. *Deep Sea Research I.* 62, 70-88.

Lindsay, R. and A. Schweiger (2015) Arctic sea-ice thickness loss determined using subsurface, aircraft, and satellite observations. The Cryosphere, 9, 269-283, doi: 10.5194/tc-9-269-2015

Lisiecki L.E., and M.E. Raymo (2005) A Pliocene-Pleistocene stack of 57 globally distributed benthic δ^{18}O records. *Paleoceanography,* 20, PA1003. doi:10.1029/2004PA001071

Löwemark L, Jakobsson M, Mörth M, Backman J, (2008) Arctic Ocean Mn contents and sediment color cycles. Polar Res. 27:105-113

Löwemark L, O'Regan M, Hanebuth T, Jakobsson M, (2012) Late Quaternary spatial and temporal variability in Arctic deep-sea bioturbation and its relation to Mn-cycles. Paleogeogr. Paleoclimatol, Paleoecol. 365:192-208

Löwemark L, März C, O'Regan M, Gyllencruetz R (2014) Arctic Ocean Mn-stratigraphy: genesis, synthesis and inter-basin correlation. Quat. Sci. Rev. 92:97-111. http://dx.doi.org/10.1016/j.quascirev.2013.11.018

Macdonald R and Gobeil C (2012) Manganese sources and sinks in the Arctic Ocean with reference to periodic enrichments in basin sediments. Aquat. Geochem. 18:565-591

Macdonald, R.W., Naidu, A.S., Yunker, M.B., & Gobail, C. (2004) The Beaufrot Sea: Distribution, sources, fluxes, and burial of organic carbon. In: R. Stein & R.W. Macdonald (Eds), *The organic carbon cycle in the Arctic Ocean* (pp. 6-21). Heidelberg: Springer-Verlag.

Maher, H.D. Jr. (2001) Manifestations of the Cretaceous high Arctic igneous province in Svalbard. *The Journal of Geology,* 109, 1, 91-104.

Malvern Instruments Limited. (2015) Measuring the particle size of small sample volumes using laser diffraction. *Application Note.* Malvern Panalytical.

Mammone, K.A. (1998) Sediment provenance and transport on the Siberian Arctic shelf. Master's Thesis, Oregon State University.

Margold, M., Stokes, C.R., Clark, C.D. (2015) Ice streams in the Laurentide Ice Sheet: Identification, characteristics, and comparison to modern ice sheets. *Earth-Science Reviews*, 143, 117-146

Markussen, B., Zahn, R., and J. Theide (1985) Late Quaternary sedimentation in the eastern Arctic Basin: stratigraphy and depositional environment. *Paleogeogr. Paleoclimateol., Paleoecol.,* 50, 271-284.

McManus J, Berelson WM, Klinkhammer GP, Johnson KS, Coale KH, Anderson RF, Kumar N, Burdige DJ, Hammond DE, Brumsack HJ, McCorkle DC, Rushdi A (1998) Geochemistry of barium in marine sediments: Implications for its use as a paleoproxy. Geochim. Cosmo. Acta. 62:3453-3473

Moore D.M., and R.C. Reynolds (1997) X-Ray Diffraction and the Identification and Analysis of Clay Minerals. Oxford University Press, New York

Miller, G.H. and J. Brigham-Grette (1989) Amino Acid geochronology: resolution and precision in carbonate fossils. *Quaternary International.* 1, 111-128.

Miller, G.H and J. Mangerud (1985) Aminostratigraphy of European marine interglacial deposits. *Quaternary Science Reviews,* 4, 4, 215-278.

Miller, G.H., R.B. Alley, J. Brigham-Grette, J.J. Fitzpatrick, L. Polyak, M.C. Serreze, and J.W.C. White (2010) Arctic Amplification: can the past constrain the future? *Quaternary Science Reviews,* 29, 1779-1790.

Moller, P., D.J. Lubinski, O. Ingolfsson, S.L. Forman, M.S. Seidenkrantz, D.Y. Bolshiyanov, H. Lokranz, O. Antonov, M. Pavlov, K. Ljung, J. Zeeberg, A. Andreev (2006) Severnaya Zemlya, Arctic Russia: a nucleation area for Kara Sea-ice sheets during the Middle to Late Quaternary. *Quaternary Science Reviews,* 25, 2894-2936.

Monnin, E., A. Indermuhle, A. Dallenbach, J. Fluckiger, B. Stauffer, T.F. Stocker, D. Raynaud, and J.-M. Barnola. (2001) Atmospheric CO2 concentrations over the Last Glacial Termination. *Science.* 291, 112-114, doi: 10.1126/science.291.5501.112.

Müller, C. and Stein, R. (2000) Variability of fluvial sediment supply to the Laptev Sea continental margin during late Weichselian to Holocene times: implications from the clay mineral records. *International Journal of Earth Sciences*, 89, 592-604.

Müller, J., G. Masse, R. Stein, and S.T. Belt (2009) Variability of sea-ice conditions in the Fram Strait over the past 30,000 years. *Nature Geoscience,* 2, 772-776.

Mysak, L.A. (2001) Patterns of Arctic Circulation. *Science,* 293, 1269-1270.

Naidu, A.S., Creager, J.S., Mowatt, T.C. (1982) Clay mineral dispersal patterns in the North Bering and Chukchi seas. *Marine Geology*, 47, 1-15.

Naidu, A.S. and Mowatt, T.C. (1983) Sources and dispersal patterns of clay minerals in surface sediments from the continental-shelf areas off Alaska. *Geological Society of America Bulletin,* 94, 841-854.

Nathan, Y. and Flexer, A. (1977) Clinoptilolite, paragenesis and stratigraphy. *Sedimentology,* 24, 6, 845-855.

Naugler, F.P., Silverberg, N., Creager, J.S. (1974) Recent sediments of the East Siberian Sea. In. Herman, Y. (ed.) Marine Geology and Oceanography of the Arctic Seas. Springer-Verlag, New York.

Niessen, F., J.K. Hong, A. Hegewald, J. Matthiessen, R. Stein, Kim, H., Kim, S., Jensen, L., Jokat, W., Nam, S.-I., Kang, S.-H., (2013) Repeated Pleistocene glaciation of the East Siberian Continental margin. *Nature Geoscience.*

Nørgaard-Pedersen, N., Spielhagen, R.F., Erlenkeuser, H., Grootes, P.M., Heinmeier, J., Knies, J., (2003) Arctic Ocean during the Last Glacial Maximum: Atlantic and polar domains of surface water mass distribution and ice cover. *Paleoceanography*, 18(3), 1063.

Not C, Hillaire-Marcel C (2010) Time constraints from 230^{Th} and 231 Pa data in late Quaternary, low sedimentation rate sequences from the Arctic Ocean: an example from the northern Mendeleev Ridge. Quat. Sci. Rev. 29:3665-3675

Nowaczyk, N.R. and T.W. Frederichs (1999) Geomagnetic events and relative palaeointensity variations during the past 300 ka as recorded in Kolbeinsey Ridge sediments, Iceland Sea: indication for a strongly variable geomagnetic field. *Int. Jour. of Earth Sci.*, 88, 1, 116-131

Nowaczyk NR, Antonow M, Knies J, Spielhagen RF (2003) Further rock magnetic and chronostratigraphic results on reversal excursions during the last 50 ka as derived from northern high latitudes and discrepancies in precise AMS ^{14}C dating. Geophys. J. Int. 155:1065-1080

Nürnberg, D., I. Wollenburg, D. Dethleff, H. Eicken, H. Kassens, T. Letzig, E. Remnitz, and J. Thiede (1994) Sediments in Arctic sea-ice: Implications for entrainment, transport, and release. *Marine Geology,* 119, 3-4, 185-214.

Nürnberg, D., Levitan, M.A., Pavlidis, J.A., Shelekhova, E.S. (1995) Distribution of clay minerals in surface sediments from the eastern Barents and south-western Kara seas. *Geol Rundsch.,* 84, 665-682.

O'Regan, M., Jakobsson, M., Kirchner, N. (2010) Glacial geological implications of overconsolidated sediments on the Lomonosov Ridge and Yermak Plateau. *Quaternary Science Reviews*, 29, 3532-3544.

Oziel, L., Sirven, J., Gascard, J.-C. (2016) The Barents Sea frontal zones and water masses variability (1980-2011). *Ocean Science,* 12, 169-184.

Palmer, H.C., Baragar, W.R.A., Fortier, M., Foster, J.H. (1983) Paleomagnetism of Late Proterozoic rocks, Victoria Island, Northwest Territories, Canada, *Canadian Journal of Earth Sciences*, 20(9), 1456-1469, doi: 10.1139/e83-131.

Parkinson, C.L. and J.C. Comiso (2013) On the 2012 record low Arctic sea-ice cover: Combined impact of preconditioning and an August storm. Geophysical Research Letters, 40, 1356-1361.

Pendleton, S.L., E.G. Ceperley, J.P. Briner, D.S. Kaufman, S. Zimmerman (2015) Rapid and early deglaciation in the central Brooks Range, Arctic Alaska. *Geology.* 43, 419-422. doi: 10.1130/G36430.1.

Pfirman, S., Haxby, W.F., Colony, R., Rigor, I. (2004) Variability in Arctic sea-ice drift. *Geophysical Research Letters,* 31, L16402, doi: 10.1029/2004GL020063.

Poirier, R.K., T.M. Cronin, W.M. Briggs, and R. Lockwood (2012) Central Arcitc paleoceanography for the last 50 kyr based on ostracode faunal assemblages. *Marine Micropaleontology*. 88-89, 65-76.

Polyak, L., M.H. Edwards, B. Coakley, and M. Jakobsson (2001) Ice shelves in the Pleistocene Arctic Ocean inferred from deep-sea bedforms. *Nature*, 410, 6827, 453-457.

Polyak, L., W.B. Curry, D.A. Darby, J. Bischof, and T.M. Cronin (2004), Contrasting glacial/interglacial regimes in the western Arctic Ocean as exemplified by a sedimentary record form the Mendeleev Ridge. *Palaeogeography, Palaeoclimatology, Palaeoecology,* 203, 73-93.

Polyak L et al (2009) Late Quaternary stratigraphy and sedimentation patterns in the western Arctic Ocean, *Global and Planetary Change,* 68, 5-17, doi: 10.1016/j.gloplacha.2009.03.014

Poore RZ, L. Osterman, W.B. Curry, and R.L. Phillips (1999) Late Pleistocene and Holocene meltwater events in the western Arctic Ocean. *Geology*, 27, 8, 759-762

Rasmussen, S.O., K.K. Andersen, A.M. Svensson, J.P. Steffensen, B.M. Vinther, H.B. Clausen, M.-L. Siggaard-Aderdsen, S.J. Johnsen, L.B. Larsen, D. Dahl-Jensen, M. Bigler, R. Rothlisberger, H. Fischer, K. Goto-Azuma, M.E. Hansson, and U. Ruth (2006) A new Greenland ice core chronology for the last glacial termination. *J. Geophys. Res.,* 111, DO6102.

Rasmussen, S.O., M. Bigler, S.P. Blockley, T. Blunier, S.L. Buchardt, H.B. Clausen, V. Cvigjanovic, D. Dahl-Jensen, S.J. Johnsen, H. Fischer, V. Gkinis, M. Guillevic, W.Z. Hoek, J. John Lowe, J.B. Pedro, T. Popp, I.K. Seierstad, J.P. Steffensen, A.M. Svensson, P. Vallelonga, B.M. Vinther, M.J.C. Walker, J.J. Wheatley, and M. Winstrup (2014) A stratigraphic framework for abrupt climatic changes during the Last Glacial period based on three synchronized Greenland ice-core records: refining and extending the INTIMATE event stratigraphy.

Reed, B.L. and Hemley, J.J. (1966) Occurrence of pyrophyllite in the Kekiktuk Conglomerate, Brooks Range, northeastern Alaska: U.S. Geological Survey Professional Paper, 550-C. C162-C166.

Reeder, S.W., Hitchon, B., Levinson, A.A. (1972) Hydrogeochemistry of the surface waters of the Mackenzie River drainage basin, Canada – I. Factors controlling inorganic composition. *Geochemica et Cosmochemica Acta*, 38 (8), 825-865.

Reimnitz, E., McCormick, M., Bischof, J., Darby, D.A. (1998) Comparing sea-ice sediment load with Beaufort Sea Shelf deposits: Is entrainment selective? *Journal of Sedimentary Research.* 68, 777-787

Reimnitz, E., Marincovich Jr., L., McCormick, M., and W.M. Briggs (1992) Suspension freezing of bottom sediment and biota in the Northwest Passage and implications for Arctic Ocean sedimentation. *Canadian Journal of Earth Science*, 29, 4, 693-703.

Rigor, I., Wallace, J.M., Colony, R.L. (2002) Response of sea-ice to the Arctic Oscillation. *Journal of Climate*, 15, 18, 2648-2668

Rossak, B.T., Kassens, H., Lange, H., Thiede, J. (1999) Clay mineral distribution in surface sediments of the Laptev Sea: indicator for sediment provinces, dynamics and sources. In: Kassens, H., Bauch, H.A., Dmitrenko, I., Eicken, H., Hubberten, H.-W., Melles, M., Thiede, J., Timokhov, L. (Eds.), Land-Ocean Systems in the Siberian Arctic: Dynamics and History. Springer, Berlin, pp. 587-599.

Rudels, B., Korhonen, M., Schauer, U., Pisarev, S., Rabe, B., Wizotzki, A. (2015) Circulation and transformation of Atlantic water in the Eurasian Basin and the contribution of the Fram Strait inflow branch to the Arctic Ocean heat budget. *Progress in Oceanography,* 132, 128-152

Schauer, U., Rudels, B., Jones, E.P., Anderson, L.G., Muench, R.D. et al. (2002) Confluence and redistribution of Atlantic water in the Nansen, Amundsen, and Makarov Basins. *Annales Geophysicae,* European Geosciences Union, 20 (2), 257-273.

Schlitzer R. (2012) Ocean Data Viewer. http://odv.awi.de

Schoster, F. & Stein, R. (1999) Major and minor elements in surface sediments of Ob and Yenisei estuaries and the adjacent Kara Sea. In: Matthiessen, J. Stepanets, O.V., Stein, R., Fütterer, D.K., Galimov, E.M. (eds.) The Kara Sea expedition of RV “Akademik Boris Petrov”: first results of a joint Russian-German pilot study. *Ber. Polarforschung,* 300, 239-252.

Schoster, F., M. Behrends, C. Muller, R. Stein, and M. Wahsner (2000) Modern river discharge and pathways of supplied material in the Eurasian Arctic Ocean: Evidence from mineral assemblages and major and minor element distributions. *International Journal of Earth Science, 89,* 486-495.

Schauer, U., Rudels, B., Jones, E.P., Anderson, L.G., Muench, R.D. et al. (2002) Confluence and redistribution of Atlantic water in the Nansen, Amundsen, and Makarov Basins. *Annales Geophysicae,* European Geosciences Union, 20 (2), 257-273.

Sellén E, O’Regan M, Jakobsson M (2010) Spatial and temporal Arctic Ocean depostional regimes: a key to the evolution of ice drift and current patterns. Quat. Sci. Rev. 29:3644-3664

Sejrup H.P., Gifford, H.M., Brigham-Grette, J., Løvlie, R. and D. Hopkins (1984) Amino Acid epimirazation implies rapid sedimentation rates in Arctic Ocean cores. *Nature,* 310, 772-775, doi:10.1038/310772a0.

Serreze, M., M. Holland and J. Stroeve (2007) Perspectives on the Arctic's shrinking sea-ice cover, *Science*, 315, 1533-1536.

Serreze, M.C., Barret, A.P., Stroeve, J.C., Kindig, D.N., and M.M. Holland (2009) The emergence of surface-based Arctic amplification. *The Cryosphere*, 3, 11-19.

Sohn, R.A. et al. (2008) Explosive volcanism on the ultra-slow spreading Gakkel Ridge, Arctic Ocean. *Nature,* 453, 1236-1238.

Spielhagen RF and Erlenkeuser H (1994) Stable oxygen and carbon isotope ratios in planktic foraminifers from the Arctic Ocean surface sediments: Reflection of the low salinity surface water layer. Mar. Geol. 119:227-250

Spielhagen, R.F., K-H., Baumann, H. Erlenkeuser, N.R. Nowaczyk, N. Nørgaard-Pedersen, C. Vogt, and D. Weiel (2004) Arctic Ocean deep-sea record of northern Eurasian ice sheet history. *Quaternary Science Reviews,* 23, 1455-1483.

Srondon, J., V.A. Drits, D.K. McCarty, J.C.C. Hsieh, and D.D. Eberl (2001) Quantitative mineral analysis by powder X-ray diffraction from random preparations. *Clays and Clay Minerals, 49*, 514-528.

St. John, K. (2008) Cenozoic ice-rafting history of the central Arctic Ocean: Terrigenous sands on the Lomonosov Ridge. *Paleoceanography*, 23, PA1S05, doi: 10.1029/2007PA0011483

St. John, K. Passchier, S., Tantillo, B., Darby, D., Kearns, L., (2015) Microfeatures of modern sea-ice rafted sediments and implications for paleo-sea-ice reconstructions. *Annals of Glaciology*, 56(69), doi: 10.3189/2015AoG69A586

Stokes, C.R., Clark, C.D., Darby, D.A., and Hodgson, D., 2005, Late Pleistocene ice export events in the Arctic Ocean linked to the M'Clure Strait ice stream, Canadian Arctic. Global and Planetary Change, 49(3-4): 139-162St. Onge G, Stoner JS (2011) Paleomagnetism near the North Magnetic Pole: A unique vantage point for understanding the dynamics of the geomagnetic field and its secular variations. Oceanography 24:42-50,http://dx.doi.org/10.5670/oceanog.2011.53

Stärz M, Gong X, Stein R, Darby DA, Kauker F, Lohmann G (2012) Glacial shortcut of Arctic sea-ice transport. *Earth Planet. Sci. Lett*. 357:257-267

Steffensen, J.P., K.K. Andersen, M. Bigler, H.B. Clausen, D. Dahl-Jensen, H. Fischer, K. Goto-Azuma, M. Hansson, S.J. Johnson, J. Jouzel, V. Masson-Delmotte, T. Popp, S.O. Rasmussen, R. Rothlisberger, U. Ruth, B. Stauffer, M.-L. Siggaard-Andersen, A.E. Sveinbornsdottir, A. Svensson, and J.W.C White (2008) High-Resolution Greenland Ice Core Data Show Abrupt Climate Change Happens in Few Years. *Science,* 321, 680-684.

Stein, R., K. Dittmers, K. Fahl, M. Kraus, J. Matthiessen, F. Niessen, M. Pirrung, Y. Polykova, F. Schoster, T. Steinke, and D.K. Fütterer (2003) Arctic (palaeo) river discharge and environmental change: evidence of the Holocene Kara Sea sedimentary record. *Quaternary Science Reviews,* doi:10.1016j.quascirev.2003.12.004

Stein, R., Fahl, K., Gierz, P., Niessen, F., and Lohmann, G. (2017) Arctic Ocean sea-ice cover during the penultimate glacial and the last interglacial. *Nature Communications*, 8:373, 13 pp., DOI: 10.1038/s41467-017-00552-1

Stein, R. (2008) Arctic Ocean Sediments: Processes, Proxies, and Paleoenvironment. Ed. H. Chamley, *Developments in Marine Geology 2,* Elsevier, Amsterdam.

Stein R, J. Matthiessen, F. Niessen, R. Krylov, S. Nam, and E. Bazhenova (2010) Towards a better (Litho-) stratigraphy and reconstruction of Quaternary Paleoenvironment in the Amerasian Basin (Arctic Ocean). *Polarforschung*, 79, 97-121

Steuerwald, B.A., Clark, D.L., and J.A. Andrew (1968) Magnetic stratigraphy and faunal patterns in Arctic Ocean sediments. *Earth and Planetary Science Letters,* 5, 79-85, doi:10.1016/ S0012-821X(68)80018-4.

Stoner J.S., A. Jennings, G.B. Kristjánsdóttir, G. Dunhill, J.T. Andrews, and J. Hardardóttir (2007) A paleomagnetic approach toward refining Holocene radiocarbon-based chronologies: Paleoceanographic records from the north Iceland (MD99-2269) and east Greenland (MD99-2322) margins. *Paleoceanography,* 22, PA1209, doi: 10.1029/2006PA001285.

Strand, K. and Immonen, N. (2010) Dynamics of the Barents-Kara ice sheet as revealed by quartz sand grain microtextures of the late Pleistocene Arctic Ocean sediments. *Quaternary Science Reviews*, 29, 3583-3589.

Svendsen J.I., H. Alexanderson, V.I. Astakhov et al. (2004) Late Quaternary ice sheet history of Northern Eurasia. *Quaternary Science Reviews,* 23, 1229-1271

Tosca, N.J., Macdonald, F.A., Strauss, J.V., Johnston, D.T., Knoll, A.H. (2011) Sedimentary talc in Neoproterozoic carbonate successions. *Earth and Planetary Science Letters,* 306, 11-22.

Velde, B. (1985) Clay Minerals: A Physico-Chemical Explanation of Their Occurance. *Elsevier Science Publishers, B.V.* The Netherlands. 427 pp.

Vidal L., R.R. Schneider, O. Marchal, T. Bickert, T.F. Stocker, and G. Wefer (1999) Link between the North and South Atlantic during the Heinrich events of the last glacial period. *Climate Dynamics*, 15, 12, 909-919. doi:10.1007/s003820050321

Viscosi-Shirley, C., K. Mammone, N. Pisias, and J. Dymond (2003a) Clay mineralogy and multi-element chemistry of surface sediments on the Siberian-Arctic shelf: Implications for sediment provenance and grain size sorting. *Continental Shelf Research, 23,* 1175-1200.

Viscosi-Shirley, C., N. Pisias, and K. Mammone (2003b) Sediment source strength, transport pathways and accumulation patterns on the Siberian-Arctic's Chukchi and Laptev shelves. *Continental Shelf Research, 23,* 1201-1225.

Vogt, P.R., Crane, K., Sundvor, E. (1994) Deep Pleistocene iceberg ploughmarks on the Yermak Plateau: sidescan and 3.5 kHz evidence for thick calving ice fronts and a possible marine ice sheet in the Arctic Ocean. *Geology, 22, 403-406.*

Vogt, C. (1996) Bulk mineralogy in surface sediments from the eastern central Arctic Ocean. In: Stein, R., Ivanov, G.I., Levitan, M.A., Fahl, K. (eds.) Surface-sediment compostion and sedimentary processes in the central Arctic Ocean and along the Eurasian Continental Margin, Reports on Polar Research, Alfred Wegener Institute for Polar and Marine Research, Bremerhaven, 212, 159-171, hdl: 10013/epic.10213.d001

Vogt, C. (1997) Zeitliche und räumliche Verteilung von Mineralvergesellschaftungen in spätquartären Sedimenten des Arktischen Ozeans und ihre Nutzbarkeit als Klimaindikatoren während der Glazial/ Interglazial-Wechsel. [Ph.D.], Univ. Bremen. Reports on Polar Research, 251, 309 p. AWI, Bremerhaven, doi:10.2312/BzP_0251_1997. Download: http://hdl.handle.net/10013/epic.10254

Vogt, C., and J. Knies (2008) Sediment dynamics in the Eurasian Arctic Ocean during the last deglaciation—The clay mineral group smectite perspective. *Marine Geology, 250,* 211-222.

Vogt, C. and J. Knies (2009) Sediment pathways in the western Barents Sea inferred from clay mineral assemblages in surface sediments. *Norwegian Journal of Geology,* 89, 41-55. Trondheim, ISSN 029-196X.

Vogt, C., J. Knies, R.F. Spielhagen, and R. Stein (2001) Detailed mineralogical evidence for two nearly identical glacial/Deglacial cycles and Atlantic water advection to the Arctic Ocean during the last 90,000 years. *Global and Planetary Change*, 31, 23-44.

Wahsner, M., C. Muller, G. Ivanov, D. Nurnburg, E.S. Shelekhova, R. Stein, and G. Tarasov (1999) Clay mineral distributions in surface sediments from Eurasian Arctic Ocean and the Eurasian continental margin as indicator for source areas and transport pathways of sediments: A synthesis. *Boreas, 28,* 215-233.

Wang, K-S., Shi, X-F., Zou, J-J., Kandasamy, S., Gong, X., Wu, Y-H., and Yan, Q-S. (2017) Sediment provenance variations in the southern Okhotsk Sea over the last 180 ka: Evidence from light and heavy minerals. *Palaeogeography, Palaeoclimatology, Palaeoecology,* 479, 61-70.

Wollenberg, J.E., J. Knies, and A. Mackensen (2004) High-resolution paleoproductivity fluctuations during the past 24 kyr as indicated by bentic foraminifera in the marginal Arctic Ocean. *Palaeogeography, Palaeoclimatology, Palaeoecology*. 204, 209-238.

Xiao, X. R. Stein, and K. Fahl (2015) MIS 3 to MIS 1 temporal and LGM spatial variability in Arctic Ocean sea-ice cover: Reconstruction from biomarkers, *Paleoceanography,* 30, 969-983, doi: 10.1002/2015PA002814.

Xuan C. and J.E.T. Channell (2010) Origin of apparent magnetic excursions in deep-sea sediments from Mendeleev-Alpha Ridge, Arctic Ocean. *Geochemistry Geophysics Geosystems*, 11, 2, doi: 10.1029/2009GC002879

Xuan C., J.E.T. Channell, L. Polyak, and D.A. Darby (2012) Paleomagnetism of Quaternary sediments from Lomonosov Ridge and Yermak Plateau: implications for age models in the Arctic Ocean. *Quaternary Science Reviews,* 32, 48-63

Zauderer, K. (1982) Analysis of Heavy Minerals in Arenaceous Lutites from the Northern Canada Basin, Arctic Ocean. unpublished master’s thesis. Old Dominion University, Norfok, Virginia, USA.

VITA

Wesley Blake Myers
Department of Ocean, Earth, & Atmospheric Sciences
Old Dominion University
406 Oceanography & Physical Sciences Building
Norfolk, VA 23529

Education

Master of Science, Ocean & Earth Science (Geology-Track)
Old Dominion University
August 2011

Bachelor of Science, Ocean, Earth & Atmospheric Science (Geology)
Old Dominion University
December 2008

Publications

Darby D.A., W.B. Myers, M. Jakobsson, and I. Rigor (2011) Modern dirty sea-ice characteristics and sources: The role of anchor ice. *Journal of Geophysical Research*, doi: 10.1029/2010JC006675

Darby D.A., Myers W., Herman S., and B. Nicholson (2015) Chemical fingerprinting, a precise and efficient method to determine sediment sources. *J. of Sed. Res.* 85, 247-253, doi: http://dx.doi.org/10.2110/jsr.2015.17

Myers, W.B and D.A. Darby (2015) A new age model for the Central Arctic reveals brief intervals of extreme sedimentation rates over the last 140 kyr. *Arktos.*1, doi: 10.1007/s41063-015-0009-5

Selected Presentations at Professional Meetings

Myers, W.B and D.A. Darby (2011) A refinement of Circum-Arctic mineralogy. *Poster*. Presented at APEX Fifth International Conference and Workshop: Quaternary Glacial and Climate Extremes, Longyearbyen, Svalbard, Norway, June 2011.

Myers, W.B. (2012) Unique mineralogical properties of Circum-Arctic Source Regions. Presented at Geological Society of America Annual Meeting. Charlotte, North Carolina, USA. November 2012.